EUROPEAN ORGANIZATION FOR NUCLEAR RESEARCH

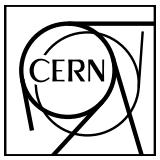

CERN-SPSC-2015-023
CERN-SR-162
June 11, 2015

COMPASS Status Report 2015

Version 2: June 16, 2015 *

Version 3: June 22, 2015 †

The COMPASS Collaboration

Abstract

The report reviews the activities and the achievements of the Collaboration during the last twelve months. Covered items are the results and ongoing analysis for the data collected in the previous years and the preparation for the 2015 Drell–Yan run.

*New section RICH 7.2.4 p. 48.

†Fig. 32 replaced, p. 30; several typos fixed on pages 10, 23, 38, 40.

Contents

1 Introduction

The report describes the new results obtained during the last twelve months, both for what concerns the hadron spectroscopy and the structure of the nucleon. The status of the 2012 DVCS and 2014 Drell–Yan data analysis is presented. Preparations for the 2015 polarised Drell–Yan run and the 2016/17 GPD/DVCS runs are described.

A summary of the results presented, giving the level reached in the corresponding analyses, is displayed in Table 1.

Channel	status	details
Hadron data		
π polarisability	final	PRL 114 (2015) 062002
Determination of the chiral dynamics in $\pi^+\gamma^* \to \pi^-\pi^0\pi^0$	new	ongoing
New axial-vector meson $a_1(1420)$ in $\pi^- p \to \pi^-\pi^-\pi^+ + p_{recoil}$	final	sub PRL
Diffractive resonance production in $\pi^- p \to \pi^-\pi^-\pi^+ + p_{recoil}$	update	PWA, fit in $m_{3\pi}$ and t'bins fit of $m_{3\pi}$ dependence
Diffractive resonance production in $\pi^- p \to \pi^-\pi^0\pi^0 + p_{recoil}$	update	PWA, fit in $m_{3\pi}$ and t'bins fit of $m_{3\pi}$ dependence
PWA of $\eta\pi$ and $\eta'\pi$ Final State	final	PLB 740 (2015) 303
Search for $Z_c(3900)$ in COMPASS	final	PLB 742 (2015) 330
Muon data		
NLO pQCD fit to the g1pnd world data and the test of the Bjorken sum rule including the 2011 g_1^p data	final	sub PLB
Determination of $\Delta g/g$ using the all-p_T events i	final	pbw
Asymmetry of inclusive photoproduction of hadrons with high-p_T at $Q^2 < 1\ (\mathrm{GeV}/c)^2$	final	pbw
Collins and Sivers asymmetries for identified π and K	final	PLB 744 (2015) 250
π multiplicities (2006 data) and FFs to pions	final	pbw
$kaon$ multiplicities (2006 data) and FFs to kaons	update	ongoing, final apart from rad. corr.
p_T dependence of multiplicities (2006 data)	update	ongoing
Interplay between Collins and two hadron asymmetries	update	pbw
The Sivers asymmetries in the Drell-Yan $x - Q^2$ region	final	part of new multidimensional analysis
Multidimensional analysis of all eight transverse asymmetries	final	pbw
The Sivers asymmetries for gluons in the proton	final	pbw
Azimuthal asymmtries for longitudinally polarised target	update	pbw
Exclusive Omega production	new	pbw

Table 1: Summary of the results presented in the report (pbw=paper being written).

2 Hadron structure and excitation spectrum

This section describes the progress made in the analysis of the data obtained with pion and proton beams in 2004, 2009 and 2012.

2.1 Photon–pion interactions in peripheral pion–nucleus scattering

Photon–pion reactions are studied at COMPASS using high-energy pion beams impinging on heavy target nuclei. Photons are provided by the Coulomb field of the nucleus, which in terms of the Weizsäcker-Williams approach constitute a quasireal photon beam with a continuous energy spectrum in the π rest frame, reaching for COMPASS kinematics up to centre-of-momentum energies in the pion–photon system of about 2 GeV. If we select the quasi-elastic channel $\pi^- + \gamma^* \to \pi^- + \gamma$ we perform Compton scattering in inverse kinematics, while spectroscopic information can be extracted from the reaction $\pi^- + \gamma^* \to \pi^-\pi^-\pi^+$.

2.1.1 Measurement of the pion polarizability

The polarizability of the pion is a fundamental property of this lightest meson and describes the inertia of the internal structure with respect to external electromagnetic fields. Both electric α_π and magnetic β_π polarizabilities are defined separately, but the present analysis assumes a strong correlation implying the assumption $\alpha_\pi + \beta_\pi = 0$, motivated by the approximate theoretical expectation from current algebra. COMPASS has completed, in the beginning of 2014, the analysis of data taken in 2009 for the measurement the pion polarisability, and the CERN preprint has been available already a year ago [1], with the final value $\alpha_\pi = (2.0 \pm 0.6_{\text{stat}} \pm 0.7_{\text{syst}}) \times 10^{-4}\,\text{fm}^3$.

The submission as a Letter of Physical Review was followed by a tedious, but finally successful refereeing process. On the scientific level, one substantial point of critique required additional work in order to achieve agreement with the referee. It concerned the correction that is due to the fact that the analysis requires the usage of CM energies of the pion–photon system up to 3.5 m_π, where the polarisability effect becomes sizable, in terms of a few percent. At this high CM energies, also higher-order effects are known to be sizeable, and for a reliable determination of the polarisability, have to be taken into account. The approach chosen in the published Letter is that from chiral perturbation theory (ChPT), in terms of the single pion loop correction. One may ask, as the referee did, how this corresponds to the alternative approach employing dispersion relations, thus estimating the pion–pion dynamics by its link to the 2π resonance spectrum. This apparently has not been studied before, so we involved the theorists of the most recent publication on dispersion relations in the current context of interest (B. Pasquini, Pisa; D. Drechsel, Mainz [2, 3]). Their calculation has been compared by us to the chiral correction, as shown in Fig. 1. In summary, the difference between the two approaches is only tiny, and could safely be neglected on the level of precision achieved with the present analysis. As a positive effect of the refereeing process, a respective comment was included in the publication.

The publication in February 2015 was followed by a CERN press release and a remarkable press echo that is documented on the COMPASS web pages.

A more refined measurement, which addresses a separate determination of α_π and β_π, is part of the COMPASS II program. In 2012, the corresponding data have been taken in similar experimental conditions as established in 2009 for the data discussed above, with the goal to increase the number of Compton scattering events by at least a factor five.

The calibration of the electromagnetic calorimeters has been worked out in the past months. A new feature extraction method, based on employing the fast Fourier transform method, has been adapted and refined for the Primakoff 2012 data. All other calibrations and post-corrections that had been found necessary for the 2009 data analysis have been revised and implemented for the 2012 data analysis. A full week has been produced for validation of the analysis, and the first full production of the 2012 Primakoff data is currently running.

In Figure 2 some first spectra of the 2012 data analysis are compared to those from 2009 data. It is found that the statistics obtained in one week of 2012 corresponds to approximately half of the full statistics from 2009. This confirms that for the analysis of 2012 data equivalent to 2009, a gain of a factor 4–5 more events is

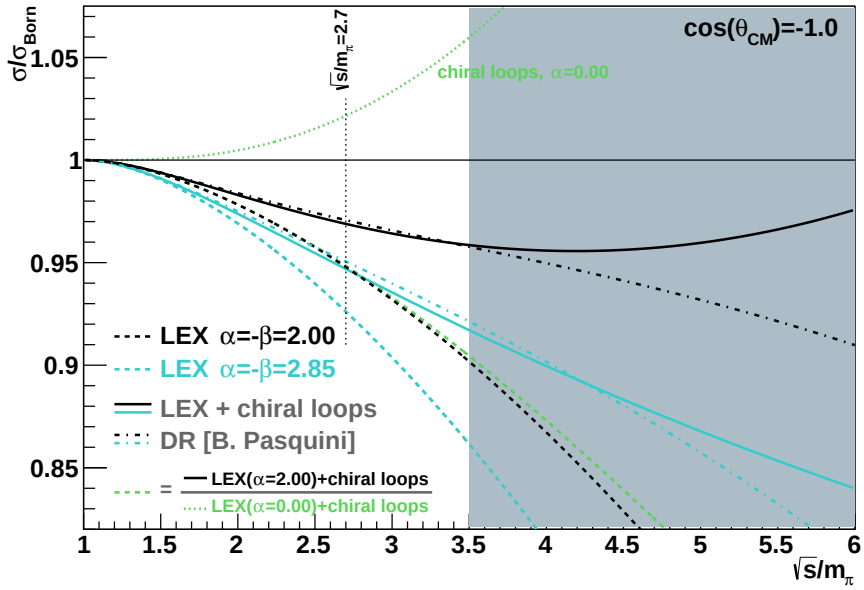

Fig. 1: Comparison of corrections to the polarisability effect as employed in the analysis of the 2009 data. The polarisability effect alone, as leading low-energy expansion (LEX) parameter, is shown as dashed lines for two values of electric pion polarisability α_π, as relative change of the cross-section for pion Compton scattering under backward angles $\cos(\theta_{\text{CM}}) = -1$. It is partly compensated by the chiral-loop correction of ChPT, corresponding in COMPASS kinematics to an effective change of the polarisability by about $+1 \times 10^{-4}\,\text{fm}^3$. The full structure effect according to one-loop ChPT is shown by the continuous lines. This full calculation is to be compared to the result of dispersion relations according to Pasquini *et al.* shown by the dash-dotted curves. Furthermore, the error made by approximating the coherent sum of chiral-loop (shown alone as dotted green curve) and polarisability effect by factorizing these two effects is indicated; it consists of the small difference between the dashed black and the dashed green curve.

expected. The analysis in the extended kinematic region, towards the disentanglement of electric and magnetic polarisability, has not yet been looked at in detail.

2.1.2 Determination of the chiral dynamics in $\pi^- + \gamma^* \to \pi^-\pi^0\pi^0$

The reactions $\pi^- + \gamma^* \to \pi^-\pi^-\pi^+$ and $\pi^- + \gamma^* \to \pi^-\pi^0\pi^0$ contain at low 3π final-state masses information related to pion–pion scattering by chiral dynamics, as both involve 4-pion vertices. This was studied in detail in the charged-pion case and published in 2011. In the past year, the corresponding analysis for the final state including two neutral pions was tackled and is in process of being finalized. In Figure 3, the current status of the result plot is depicted. The last missing step is the normalization, which can be done analogously to the charged-pion case, i.e., observation of beam K^- decays into the same final state. It is expected to be completed this summer.

2.2 Results on diffractive pion dissociation

During two beam times (2008 and 2009) COMPASS has studied pion and kaon diffractive dissociation on a hydrogen target. In these reactions various intermediate resonances X are produced by the incoming beam particles. These resonances are very short-lived and decay into various (quasi-)stable final-state hadrons measured by the spectrometer. The kinematic distribution of the final-state particles reflects the superposition of all the different X, which are characterized by the quantum numbers spin J, parity P, and C or G parity. The composition depends on the mass m_X and the four-momentum transfer squared t' to the target nucleon. For the 2008/09 data sets, the minimum value of $t' = 0.1\,(\text{GeV}/c)^2$ is defined by the trigger acceptance. COMPASS studies final states involving charged and neutral particles (e.g., K^0_S, π^0, η, and η'), the latter being identified by their decays.

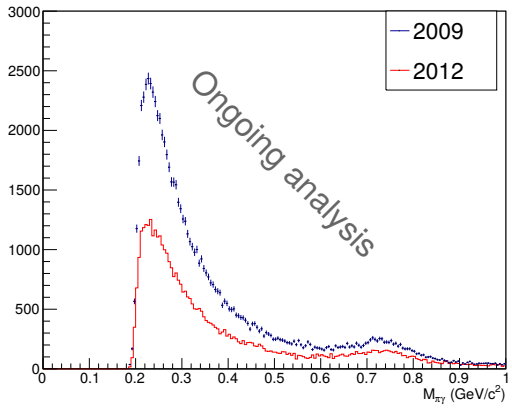

(a) Centre-of-momentum mass of the $\pi\gamma$ final state of the reaction

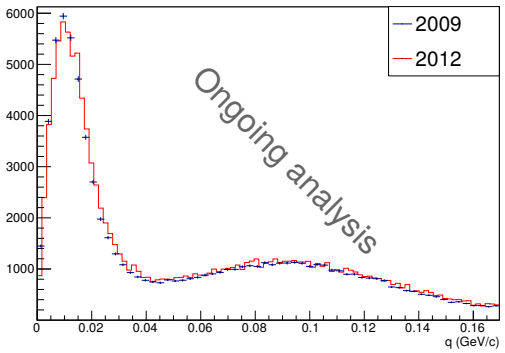

(b) Primakoff peak at smallest momentum transfer. The 2009 data have been scaled, such that its shape can be compared to the new analysis of the 2012 data.

Fig. 2: Comparison of the ongoing analysis of one week of the 2012 data to the published 2009 spectra.

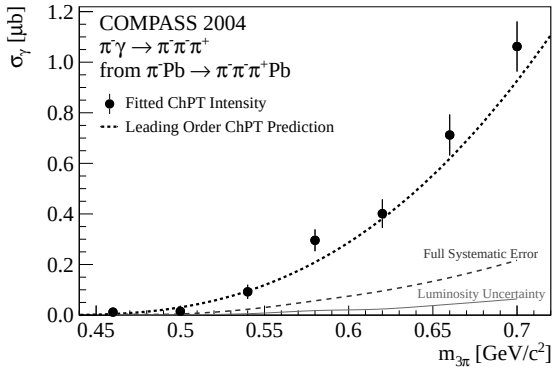

(a) Chiral Dynamics in $\pi^- + \gamma^* \to \pi^-\pi^-\pi^+$, as published in Ref. 4

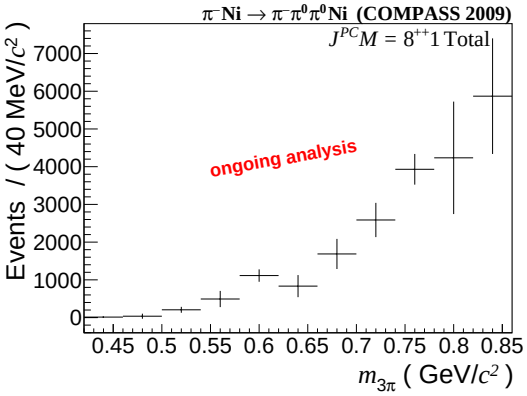

(b) Analogous analysis for $\pi^- + \gamma^* \to \pi^-\pi^0\pi^0$, from the 2009 data sample.

Fig. 3: Comparison of the threshold behaviour of the reactions $\pi\gamma \to \pi\pi^+\pi^-$ and $\pi\gamma \to \pi\pi^0\pi^0$ as extracted from scattering of pions off nuclei in Primakoff kinematics.

In order to disentangle the coherent superposition of intermediate states X with quantum numbers J^{PC} for a particular final state, we perform a partial-wave analysis (PWA). For two-body final states, this leads to a representation of the cross-section in terms of a squared sum of Legendre polynomials with complex expansion coefficients, which are called transition amplitudes. For n-body final states with $n \geq 3$, typically a more complex method, the so-called isobar model, is used, which generally has a larger model bias. In such analyses, it is assumed that the decay of the intermediate state X to the final n-body state proceeds via a series of two-body decays. In these decays, additional unstable intermediate states, the so-called isobars, appear. They correspond to known resonances or to any system that can be described analytically in terms of mass-distribution and angular variables. With the above assumptions, the amplitude for the X decay into a the n-body final state is calculable for a particular decay path up to multiplicative unknown constants. The observed kinematic distribution of the final-state particles is modelled by a set of decay amplitudes with various possible J^{PC}, each of which may have various decay paths (intermediate isobars) describing the transition from X to the final state. The coherent sum of these so-called *waves* includes complex transition amplitudes, the values of which are determined by a fit and result in the spin-density matrix. The diagonal elements of this matrix are the partial-wave intensities, which can be interpreted as the number of events that go through a particular wave. The off-diagonal elements represent the interference terms. The decomposition into partial waves is performed in narrow bins of m_X. Therefore, in this first analysis step, called *mass-independent fit*, no knowledge about possible n-body resonances is put into the model. However, the isobar amplitudes have to be known. The physics is extracted

in a second step, the *mass-dependent fit*, by connecting the resulting spin-density matrices of different mass bins using a model which typically contains resonant and non-resonant contributions for X. The outcome can systematically depend on the choice of waves, the parameterization of the isobars and on assumptions on the coherence of the amplitudes.

In the following, we will specify waves by the J^{PC} of X, its spin projection along the beam direction M, the symmetry ε of the amplitudes related to the naturality of the particle exchanged in the production process and the decay path of X ($J^{PC}\, M^{\varepsilon}$ [decay]).

2.2.1 PWA of 3π final states

Based on data taken in 2008 with 190 GeV/c pions impinging on a LH_2 target, we have selected about 4×10^7 exclusive scattering events for the $\pi^-\pi^-\pi^+$ final state and about 3.6×10^6 events for $\pi^-\pi^0\pi^0$. The $\pi^-\pi^-\pi^+$ sample is about a factor 10 to 100 larger than that of any previous experiment. The two different 3π final states are subject to similar but independent analyses. For both channels, the PWA was performed not only in narrow bins of the three-pion mass $m_{3\pi}$ but also in bins of the reduced four-momentum transfer t' in the range $0.1\,(\text{GeV}/c)^2 < t' < 1.0\,(\text{GeV}/c)^2$. The latter drastically reduces incoherences caused by the different t' dependences of the various partial waves. Typically, also the t' dependence of resonant and non-resonant contributions is different. This leads to mass spectra that change their shape as a function of t'. As will be discussed below, this additional information helps to better separate the resonant and non-resonant contributions and was one of the main motivations to perform the PWA in bins of t'.

Although the systematics of the $\pi^-\pi^-\pi^+$ and $\pi^-\pi^0\pi^0$ final states are very different, in particular concerning the acceptance correction, the two PWA analyses give very consistent results. A detailed study of the isospin symmetry that is expected to relate the intensities in the two channels is work in progress. This analysis is complicated by the fact that the Bose symmetrization of the two equally charged final-state pions, that has to be applied at the amplitude level, affects different isobars in the two channels.

Observation of a New Iso-Vector Meson The most exciting result so far is the finding of a new iso-vector axial-vector meson, the $a_1(1420)$, with $J^{PC} = 1^{++}$, a mass of $1414^{+15}_{-13}\,\text{MeV}/c^2$, and a width of $153^{+8}_{-23}\,\text{MeV}/c^2$. This state has quite unusual properties. It is observed only in the $f_0(980)\,\pi$ decay mode and collects only 0.25% of the total observed intensity. The mass of the $a_1(1420)$ is suspiciously close to the $K\overline{K}^*$ threshold. The intensity of the $1^{++}\,0^+\,f_0(980)\,\pi\,P$ wave is shown in Fig. 4a together with the model curves obtained from a mass-dependent fit of the 3×3 spin-density submatrix formed by this wave and the $2^{++}\,1^+\,\rho(770)\,\pi\,D$ and $4^{++}\,1^+\,\rho(770)\,\pi\,G$ waves. The relative phase of this wave with respect to other major waves shows the expected 180° modulation when moving across the resonance in $m_{3\pi}$ (see Fig. 4b). Since the analysis is performed in 11 bins of t', one can extract the t' spectrum of the $a_1(1420)$ component from the mass-dependent fit. The t' distribution as shown in Fig. 4c is approximately exponential with a slope parameter of about $b \approx 10\,(\text{GeV}/c)^{-2}$, similar to other resonances.

The interpretation of this new state is still unclear. Quark-model calculations including tetra-quark states predict $nn\,\overline{nn}$ and $ns\,\overline{ns}$ iso-vector states at 1381 and 1530 MeV/c^2, respectively [5]. The molecular model for the $f_1(1420)$ proposed in Ref. 6 could possibly be extended to the isovector case. After our first announcement of the $a_1(1420)$ [7], several explanations were proposed [8–10], none of them describing all features of the data. The properties of the $a_1(1420)$ suggest it to be the isospin partner of the $f_1(1420)$. This is supported by its mass value of 1414 MeV/c^2 and by its strong coupling to $f_0(980)$, which is interpretable as a $K\overline{K}$ molecule. The $a_1(1420)$ width of only 153 MeV/c^2 is narrow as compared to most other known iso-vector states, which typically have widths between 250 and 350 MeV/c^2. The much smaller width of the $f_1(1420)$ of only $(54.9 \pm 26)\,\text{MeV}/c^2$ can be explained by its strong coupling to $K\overline{K}^*$ with the corresponding phase space being much smaller than that for $a_1(1420)$ decaying into $f_0(980)\,\pi$. The $a_1(1420)$ and the $f_1(1420)$ may possibly be the first observed isospin partners for a $\pi K\overline{K}$ molecular-type excitation, which obey isospin symmetry. This interpretation suggests further experimental and theoretical studies of the $\pi K\overline{K}$ final state.

The above results are described in a paper submitted to PRL [11].

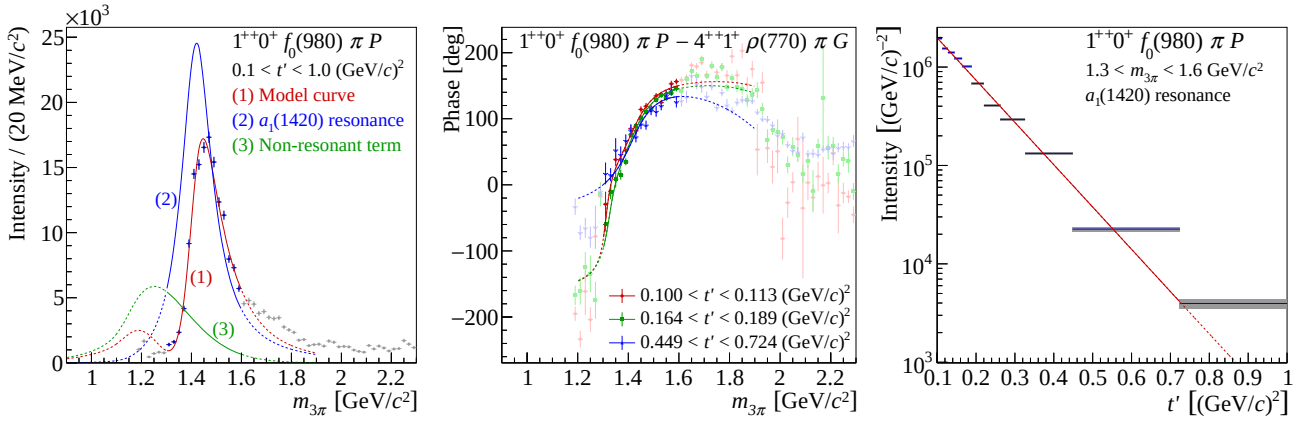

(a) (b) (c)

Fig. 4: $1^{++}\,0^{+}\,f_0(980)\,\pi\,P$ wave: Intensity distribution (a) together with the fit model, which is the coherent sum of resonances (blue) and non-resonant contributions (green). Panel (b) shows the relative phase between 1^{++} and 4^{++} together with the model curves. The t'-dependence of the $a_1(1420)$ intensity is shown in (c) together with the result of a single-exponential fit (red line).

Work in Progress Given the extraordinary precision of the $\pi^-\pi^-\pi^+$ data set, it remains one of the main focusses of the COMPASS spectroscopy analyses. The efforts concentrate primarily on the publication of the PWA results obtained so far. A paper that describes the results from the mass-independent fit using an 88-wave model is in the final stage of drafting. Highlights of this paper are the systematic study of the t' spectra of resonance regions in individual partial waves and the results of a *free-isobar* fit. In this analysis, the amplitude of the $\pi^+\pi^-$ subsystem with $J^{PC} = 0^{++}$ quantum numbers is extracted from the data as a function of 3π mass and t' by replacing the fixed parametrizations, used in the conventional approach, by piece-wise constant functions that appear as free fit parameters. Based on this publication, two follow-up papers will present results from the mass-dependent fit of a subset of 14 partial waves in 11 t' bins. One of the papers will focus on the spin-exotic $\pi_1(1600)$, the second on the other resonances. Extensive studies have been performed in order to reliably estimate the systematic uncertainties of the extracted resonance parameters. They are nearly finished.

In parallel to the publication efforts there is ongoing work to develop of new tools and methods. For the $\pi^-\pi^-\pi^+$ final state, this work addresses two issues: i) The possible extension of the free-isobar method to other isobars beyond $J^{PC} = 0^{++}$ by applying an iterative bootstrapping method, where some isobar amplitudes are left free and then the result is fed back into the next fit, in which other isobars are freed. The main challenge here is that for the waves with free isobars the orthogonality of the decay amplitudes is broken by the Bose symmetrization of the two π^- in the final state. Given that this issue can be solved and that the iterative procedure converges, this method will greatly reduce the model bias introduced by the isobar parametrizations. In addition, information about how the third bachelor pion influences the $\pi^+\pi^-$ system can be extracted from the data. ii) Studies showed that the systematic uncertainty of many resonance parameters is mainly limited by the description of the non-resonant component. A large fraction of the non-resonant contribution is caused by the Deck effect. This is supported by results from the partial-wave decomposition of Monte Carlo data generated using a particular model of the Deck effect. In order to separate this component, studies have been performed where the Deck model was included as a partial-wave amplitude at the level of the mass-independent fit. First results are encouraging. In many partial waves features attributable to the non-resonant component are suppressed or vanish nearly completely. However, in some waves unphysical artifacts appear. Given the simplistic nature of the currently employed Deck model, these effects hopefully disappear when applying more realistic models.

2.2.2 *PWA of $\eta\pi^-$ and $\eta'\pi^-$ final states*

In Reference 12 our results of a PWA of diffractively produced $\eta\pi^-$ and $\eta'\pi^-$ final states are presented. A striking similarity of the partial-wave intensities (scaled by kinematical factors) and the relative phases between the two final states is observed for orbital angular momenta of $L = 2, 4, 6$ (Figs. 5b and 5c). This includes the

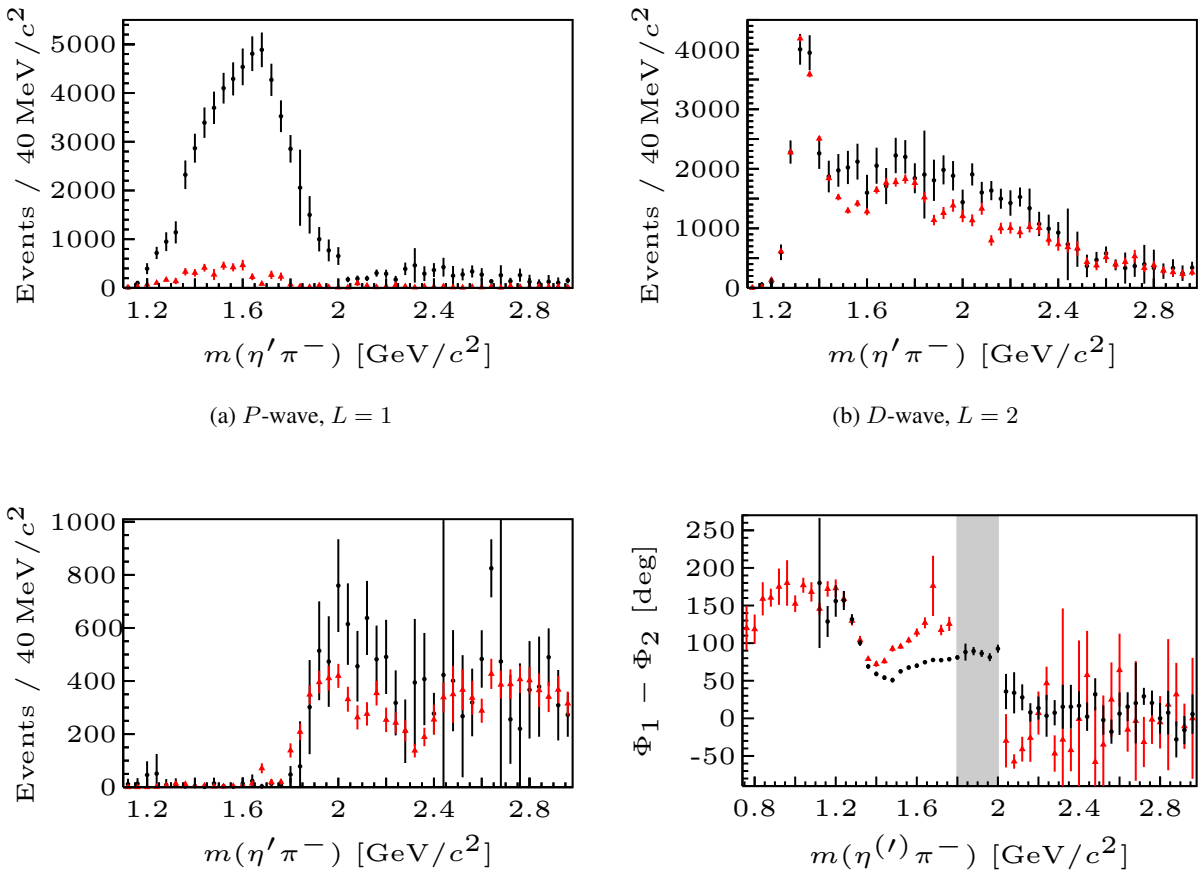

(a) P-wave, $L = 1$

(b) D-wave, $L = 2$

(c) G-wave, $L = 4$

(d)

Fig. 5: Panels (a) to (c): Partial-wave intensities from the PWA of the $\eta'\pi^-$ data (black points) together with the $\eta\pi^-$ results scaled by a kinematical factor that corrects for the different phase space (red points). Panel (d): Phase of the $L = 1$ partial wave relative to the $L = 2$ wave of $\eta\pi^-$ (red points) and $\eta'\pi^-$ (black points) systems. For $\eta\pi^-$, the phase between the P and D-waves is ill-defined in the region of vanishing P-wave intensity between 1.8 GeV/c^2 and 2.05 GeV/c^2 (shaded).

known resonances $a_2(1320)$ and $a_4(2040)$. In contrast, the intensities of odd-L $\eta'\pi^-$ partial waves, which carry non-$q\bar{q}$ quantum numbers, are enhanced by a factor $5 - 10$ as compared to $\eta\pi^-$ (Fig. 5a). The $L = 1$ intensity peaks at 1.7 GeV/c^2 in $\eta'\pi^-$ and at 1.4 GeV/c^2 in $\eta\pi^-$, the corresponding phase motions with respect to the $L = 2$ waves are different in the two channels (Fig. 5d). It is suggestive to ascribe these observations to the dominant $\mathbf{8} \otimes \mathbf{8}$ and $\mathbf{1} \otimes \mathbf{8}$ character of the $\eta\pi^-$ and $\eta'\pi^-$ $\mathrm{SU}(3)_{\text{flavour}}$ configurations, respectively. When the former couples to an octet intermediate state, Bose symmetry demands even L, whereas the latter may couple to the non-symmetric odd-L configurations. This is related to the interpretation of a potential π_1 resonance in the $L = 1$ wave as a hybrid ($gq\bar{q}$) or the lowest molecular state ($q\bar{q}q\bar{q}$), which both have $\mathbf{1} \otimes \mathbf{8}$ character.

From mass-dependent fits using standard relativistic Breit–Wigner parameterizations for the $a_2(1320)$ and $a_4(2040)$ resonances the following ratios of branching fractions were extracted

$$B_2 \equiv \frac{N(a_2 \to \eta'\pi^-)}{N(a_2 \to \eta\pi)} = (5 \pm 2)\% \quad \text{and} \quad B_4 \equiv \frac{N(a_4 \to \eta'\pi^-)}{N(a_4 \to \eta\pi)} = (23 \pm 7)\%. \tag{1}$$

Here, N stands for the integrated Breit–Wigner intensities of the given decay branches. The $a_2(1320)$ and $a_4(2040)$ resonance parameters and B_2 agree with the PDG values [13]. The decay branching fraction ratio B_4 is extracted for the first time.

The further analysis of this channel is focused in particular on finding a more realistic description of the non-

resonant component, which currently limits the interpretation of the resonance contents in the P-waves of both channels. The idea is to employ Regge theory in oder to describe the amplitude at large $\eta\pi^-$ and $\eta'\pi^-$ masses where no resonances contribute and the intensity is saturated by the non-resonant components. Using Finite-Energy Sum Rules, these Veneziano amplitudes can be extrapolated into the resonance region at lower masses. By including them into the mass-independent fit, the non-resonant contributions could be subtracted already at this level leading to cleaner resonance signals. This work is performed in close collaboration with the JLab Physics Analysis Center (JPAC).

2.3 Other published Results

Two analyses that were already discussed in the last report [14] have been published in the mean time.

Reference 15 reports on the exclusive production of ω and ϕ mesons off hydrogen target. Studying the cross-section ratios as a function of the Feynman variable x_F of the fast proton, a significant violation of the OZI rule is found, confirming earlier findings. The measurement of the spin-density matrix element ρ_{00} of the vector mesons in different selected reference frames distinguishes the contributions from diffractive production of $p_{\rm fast}V$ resonances and from central production. The dependence of the spin alignment on x_F and on $M_{p\rm V}$ is studied. Most of the observations can be traced back to the existence of several excited baryon states contributing to ω production which are absent in the case of the ϕ meson. Removing the low-mass $M_{p\rm V}$ resonant region, the OZI rule is found to be violated by a factor of eight, independently of $x_{\rm F}$.

Reference 16 presents a search for the exclusive muo-production of the $Z_c^{\pm}(3900)$ hadron in the decay channel $Z_c^{\pm}(3900) \rightarrow J/\psi\pi^{\pm}$ based on the full COMPASS data set collected with a muon beam between 2002 and 2011. The data cover the range from 7 to 19 GeV in the centre-of-mass energy of the photon-nucleon system. An upper limit for the ratio $BR(Z_c^{\pm}(3900) \rightarrow J/\psi\pi^{\pm}) \times \sigma_{\gamma\ N\rightarrow Z_c^{\pm}(3900)\ N}/\sigma_{\gamma\ N\rightarrow J/\psi\ N}$ of 3.7×10^{-3} is measured at the confidence level of 90%.

3 Nucleon structure results using a muon beam

3.1 NLO QCD fit to g_1 world data and verification of the Bjorken sum rule

The NLO QCD fit to the g_1 proton, deuteron, and ^{3}He world data with $Q^2 > 1$ (GeV/c)^2 and the verification of the Bjorken sum rule were already presented in the previous status report [14]. Since last June the results have been finalised and submitted for publication [17]. While the results on the Bjorken sum, evaluated from COMPASS data only, remained unchanged, the following points have been improved in the final QCD fit:

- Positivity: After realising that the condition $|\Delta(q+\bar{q})(x)| < q(x) + \bar{q}(x)$ was violated at large x for the up and down quarks in the previous fit, a penalty of $\exp(k(|\Delta q(x)| - q(x)))$ was added to χ^2 for the quark and gluon distributions for $x > 0.1$. For the factor k a value of 600 was chosen after a detailed optimisation.

- W^2 cut: A W^2 cut of 10 (GeV/c^2)^2 was implemented in order to suppress possible higher-twist effects in particular at large x. This removes mainly data points from JLab. The effect of this cut is shown in Fig. 6. A total of 495 data points remained as compared to 679 in the previous fit. The number of COMPASS points is unchanged (138).

- Shape: the parameter β_g in Eq. 2 was fixed to the value used in Ref. 18.

The functional form of the parton distribution functions $\Delta f_k(x)$ is parameterised at a reference scale of $Q_0^2 = 1$ (GeV/c)^2 and remained unchanged with respect to the previous report [14]

$$\Delta f_k(x) = \eta_k \frac{x^{\alpha_k}\,(1-x)^{\beta_k}\,(1+\gamma_k x)}{\int_0^1 x^{\alpha_k}\,(1-x)^{\beta_k}\,(1+\gamma_k x)\,\mathrm{d}x}\,, \tag{2}$$

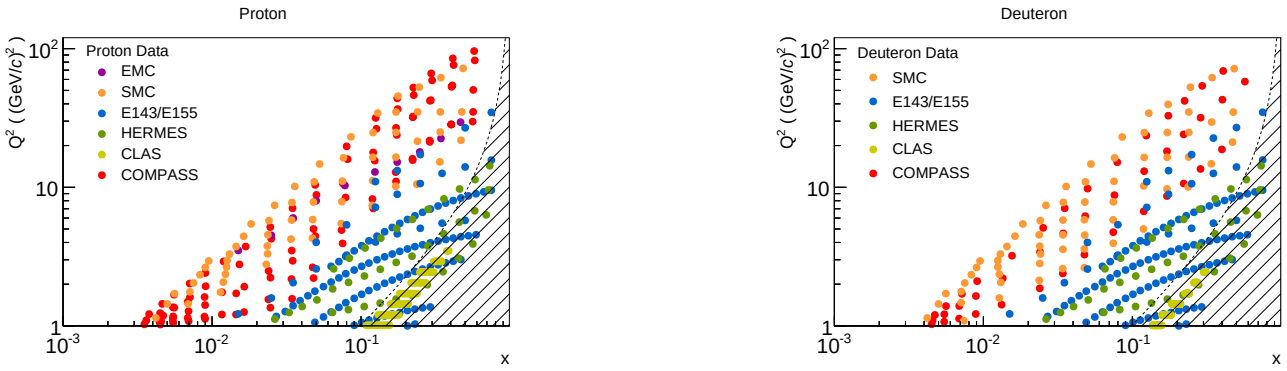

Fig. 6: Data points used in the QCD fit to the world data in the x-Q^2 plane. Data in the hatched area, where $W^2 < 10$ (GeV/c^2)^2, were omitted from the fit.

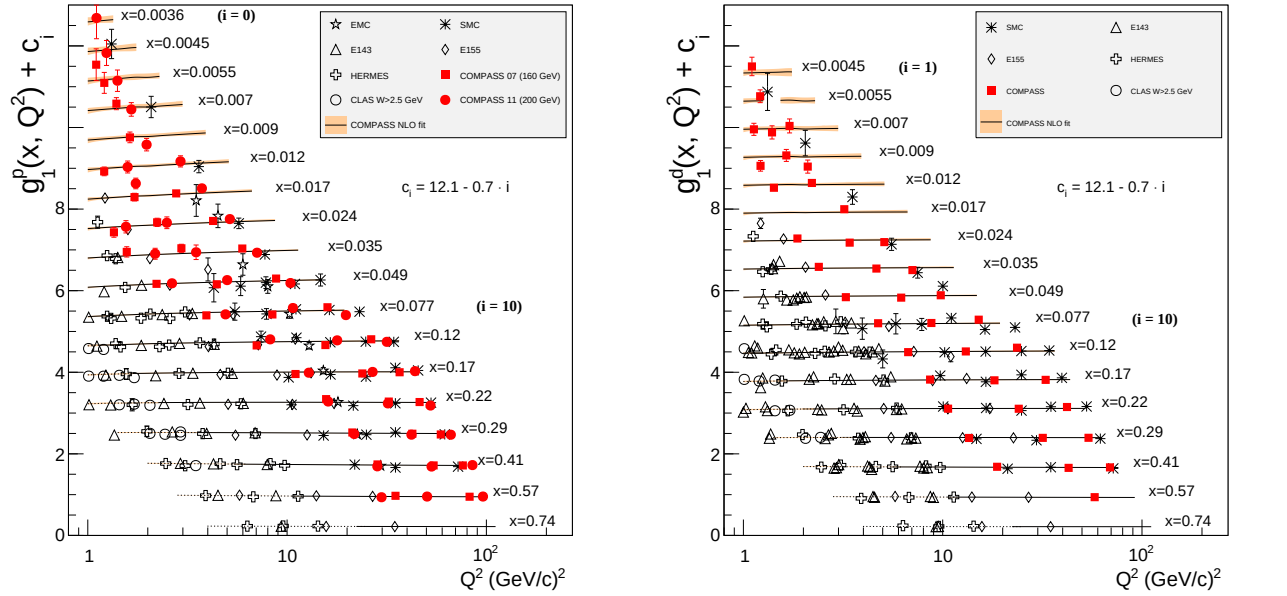

Fig. 7: World data on the spin-dependent structure function g_1 as function of Q^2 for various values of x. The lines represent the Q^2 dependence for each value of x, as determined from a NLO QCD fit. In the region not used in the fit, $W^2 < 10$ (GeV/c^2)^2, the lines are dashed. Left: proton, right: deuteron

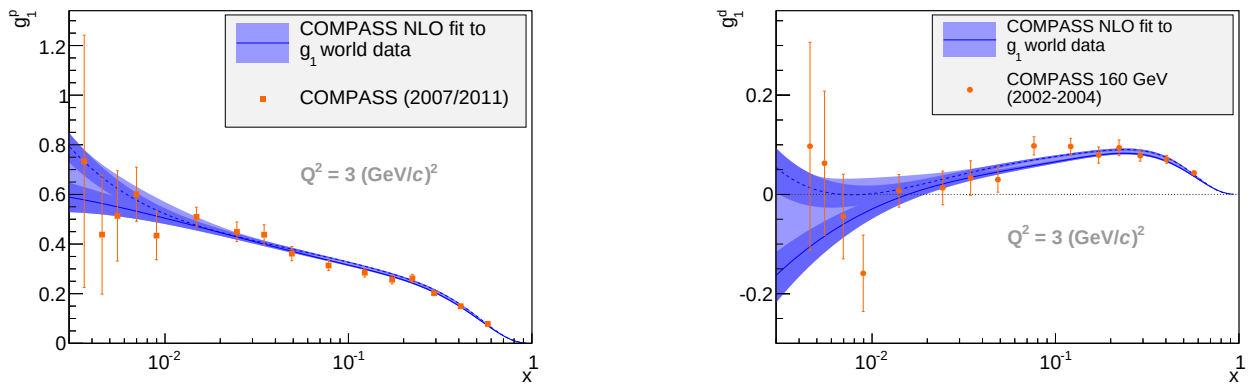

Fig. 8: Results of the QCD fit to g_1^p (left) and g_1^d (right) world data at $Q^2 = 3$ (GeV/c)^2 as functions of x. The curves correspond to two sets of functional shapes. The dark bands represent the statistical uncertainties associated with each curve and the light bands, which overlay the dark ones, represent the systematic uncertainties.

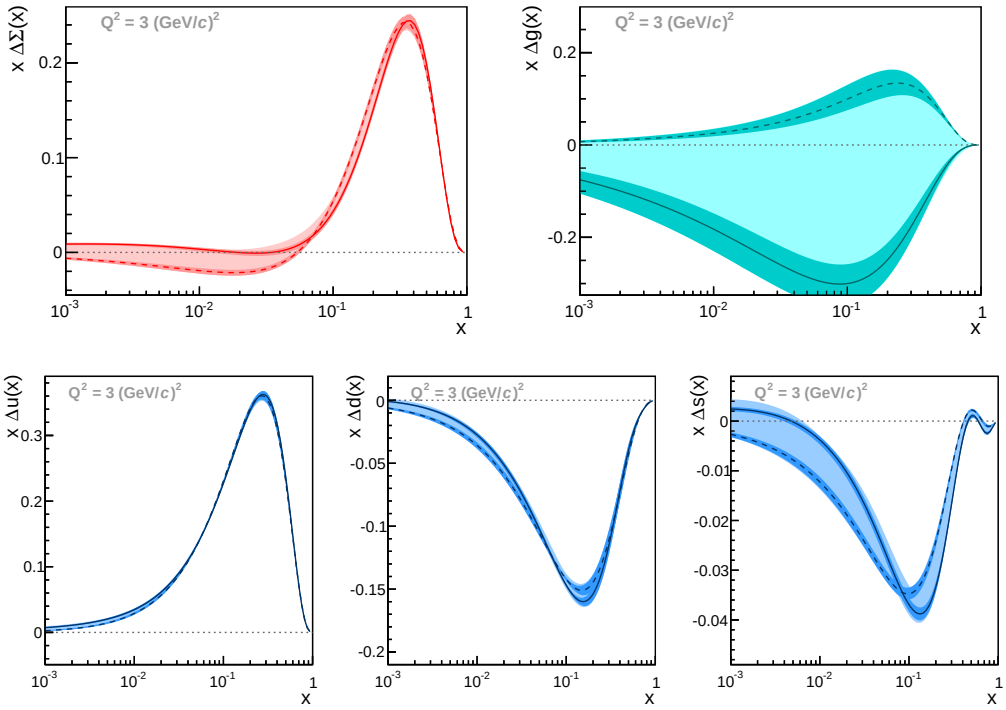

Fig. 9: Results of the QCD fit to g_1 world data at $Q^2 = 3$ (GeV/c)^2 for two sets of functional shapes. Top: singlet $x\Delta q_S(x) = x\Delta\Sigma(x)$ and gluon distribution $x\Delta g(x)$. Bottom: distributions of $x[\Delta q(x) + \Delta\bar{q}(x)]$ for up, down, and strange quarks. Continuous lines correspond to the fit with $\gamma_S = 0$, long dashed lines to the one with $\gamma_S \neq 0$. The dark bands represent the statistical uncertainties, only. The light bands, which overlay the dark ones, represent the systematic uncertainties.

where η_k is the first moment of $\Delta f_k(x)$. The moments η_k of the non-singlet distributions Δq_3 and Δq_8 are fixed by the baryon decay constants (F+D) and (3F−D) respectively, assuming SU(2)$_f$ and SU(3)$_f$ flavour symmetries. The parameter γ is non-zero only for the singlet and the gluon distributions; β_g (not well determined from the data) is fixed to 3.0225 [18]. The ranges of the first moments of the parton distributions remain basically unchanged with respect to last year.

The final fit is shown together with the data in Fig. 7 as a function of Q^2. Figure 8 shows the COMPASS proton and deuteron data for $Q^2 = 3$ (GeV/c)^2 as a function of x. Figure 9 displays the resulting PDFs.

3.2 Gluon polarisation in the nucleon

3.2.1 Determination of $\Delta g/g$ using "all-p_T" events

The "all-p_T" method for the determination of the gluon polarisation $\Delta g/g$ in the nucleon was presented in the previous status report. The analysis has been finalised and will be submitted for publication in the next weeks. The data were taken in 2002–2004 and 2006 using a 160 GeV polarised muon beam and a polarised ^{6}LiD target.

The method uses all events with a momentum transfer $Q^2 > 1$ (GeV/c)^2 and at least one hadron. No cut on the transverse hadron momentum p_T is applied. A neural network (NN), trained on Monte Carlo (MC) events, attributes three weights to each event, which reflect the probability for each event to originate from one of the three hard processes: leading-order process (LP), gluon radiation or QCD Compton (QCDC), and photon–gluon fusion (PGF) (Fig. 10). Figure 11 demonstrates the quality of the NN by comparing the MC truth for the probabilities to the ones obtained from the neural network trained on another MC sample.

The gluon polarisation is evaluated in a single bin of the gluon momentum fraction x_g as well as in three bins of x_g covering the range $0.04 < x_g < 0.28$. The results are summarised in Table 2. The largest contribution to the systematic uncertainty stems from instabilities in the spectrometer and from the MC inputs. The latter is eval-

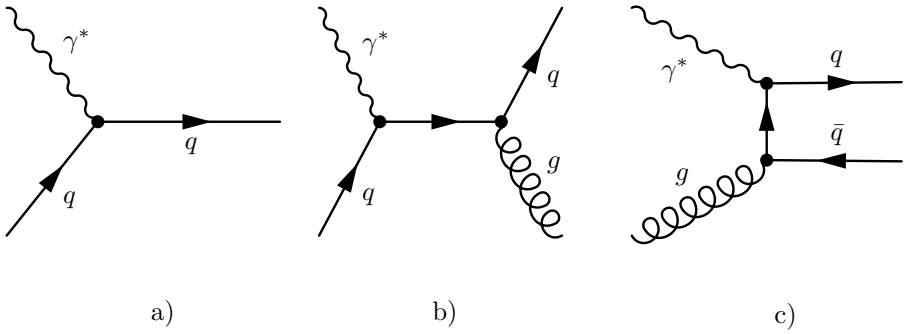

Fig. 10: Feynman diagrams for: a) a leading-order process (LP), b) gluon radiation (QCDC), and c) photon–gluon fusion (PGF).

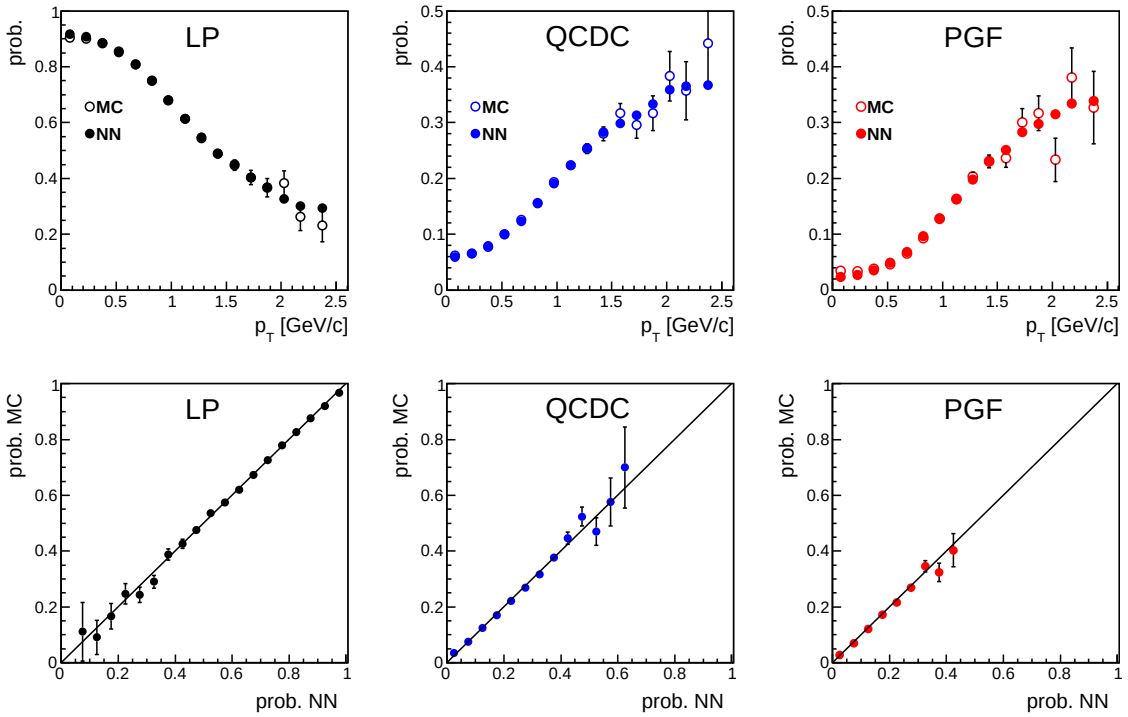

Fig. 11: Top panels: Values of the probabilities obtained from MC and from NN as functions of p_{T}; bottom panels: MC probabilities in bins of NN probabilities.

uated using eight MC samples with different input, e.g. PDFs, parton shower on/off, FLUKA vs. GHEISHA. The new result improves and supersedes our previous analysis [19]. The statistical and systematic uncertainties are reduced by a factor 1.6 and 1.8, respectively (Fig. 12, left). This is due to the cancellation in this method of some uncertainties in the simultaneous determination of $\Delta g/g$ and the leading-order-process asymmetry $A_{1,d}^{\mathrm{LP}}$, while previously the latter was estimated from the inclusive deuteron asymmetry $A_{1,d}^{\mathrm{incl}}$ obtained in a separate analysis.

The result favours a positive gluon polarisation in the measured x_{g} range. A comparison of the new results with the recent NLO QCD fit [17] is shown in Fig. 12 (right). The data points are close to the upper edge of the region allowed by the fit. Although LO and NLO results can strictly speaking not be compared directly, it gives a hint that solutions with positive gluon polarisation are preferred.

3.2.2 *Gluon contribution to the nucleon spin via single-hadron photoproduction at high-p_T*

In the previous status report we presented already the double-spin cross-section asymmetry A_{LL} for semi-inclusive single hadron production at small $Q^2 < 1(\mathrm{GeV}/c)^2$ for proton and deuteron targets as function of the hadron transverse momentum $0.7\ \mathrm{GeV}/c < p_T < 4\ \mathrm{GeV}/c$. The analysis is motivated by pQCD calculations

Table 2: The results for $\langle \Delta g/g \rangle$ at a scale of 3 $(\mathrm{GeV}/c)^2$ in three x_g bins and in a single x_g bin.

x_g^NN range	$\langle x_\mathrm{g} \rangle$	x_g range (RMS)	$\langle \Delta g/g \rangle$
$0 - 0.10$	0.08	$0.04 - 0.13$	$0.087 \pm 0.050 \pm 0.044$
$0.10 - 0.15$	0.12	$0.07 - 0.21$	$0.149 \pm 0.051 \pm 0.048$
$0.15 - 1$	0.19	$0.13 - 0.28$	$0.154 \pm 0.122 \pm 0.050$
$0 - 1$	0.10	$0.06 - 0.20$	$0.113 \pm 0.038 \pm 0.036$

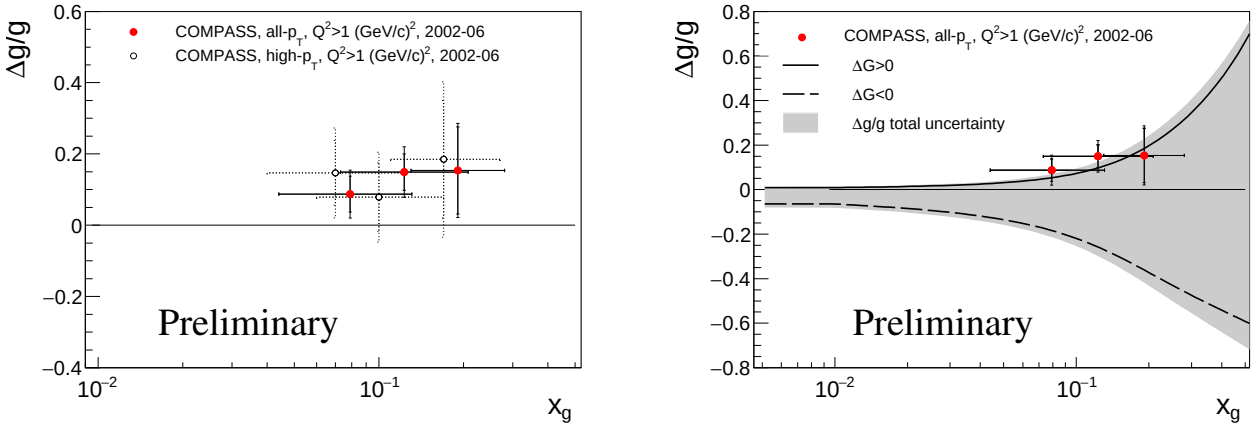

Fig. 12: The new results for $\Delta g/g$ in three x_g bins compared to our previous analysis [19] (left) and the recent COMPASS NLO QCD fit [17] (right).

for this process in COMPASS kinematics [20, 21]. The applicability of the framework at a centre-of-mass energy of $\sqrt{s} \simeq 18$ GeV was shown by the agreement of our previous cross-section measurement [22] with theoretical calculations [21]. Originally the data were integrated over the hadron polar angle in the laboratory frame with respect to the virtual photon $0.01 < \theta < 0.12$. A comparison with preliminary theoretical NLO calculations for this kinematics showed a loss of sensitivity on $\Delta g/g$ compared to calculations done in 2005 [20] integrated over a smaller range $0.01 < \theta < 0.07$. Therefore we evaluated the asymmetries as function of p_T in three bins in the c.m.s. pseudorapidity

$$\eta = -\ln(\tan\frac{\theta}{2}) - \frac{1}{2}\ln\frac{2E_\mu}{M}, \tag{3}$$

which is also used in the theoretical calculations.

For the 2002–2004 data, taken the SMC target magnet, we use $0.45 < \eta < 2.4$, while for the 2006–2011 data the range $-0.1 < \eta < 2.4$ is chosen. The η binning was optimised for similar statistics in the bins yielding the bin boundaries -0.1, 0.45, 0.9, 2.4.

Figure 13 displays the combined asymmetries for positive and negative hadrons in the three bins of η as function of p_T for the full proton and deuteron data set. The data are also available separately for positive and negative hadrons.

The data are compared in Fig. 14 to calculations using three different sets of PDFs from GRSV [23] and DSSV++ [24]. The calculations were performed with the program of Ref. 20 (courtesy of W. Vogelsang). It does not include the gluon resummation at leading logarithm, which is necessary (however not yet available) to fully explain the unpolarized cross-section at COMPASS kinematics [21]. As further input were used the DSS fragmentation functions [25], the CTEQ6 unpolarised PDFs [26], and the GRS unpolarised photon PDFs [27], and the GSV polarised photon PDFs [28]. The GRSV-min and GRSV-max PDFs assume $\Delta g = -g(x)$ and $\Delta g = g(x)$ at the reference scale $Q_0^2 = 0.40$ $(\mathrm{GeV}/c)^2$, respectively. The DSSV++ PDFs are a very recent fit including RHIC pp data indicating a positive gluon polarisation. As the LO analysis presented in the previous subsection, also the single hadron asymmetry data prefer a positive gluon polarisation when compared to NLO

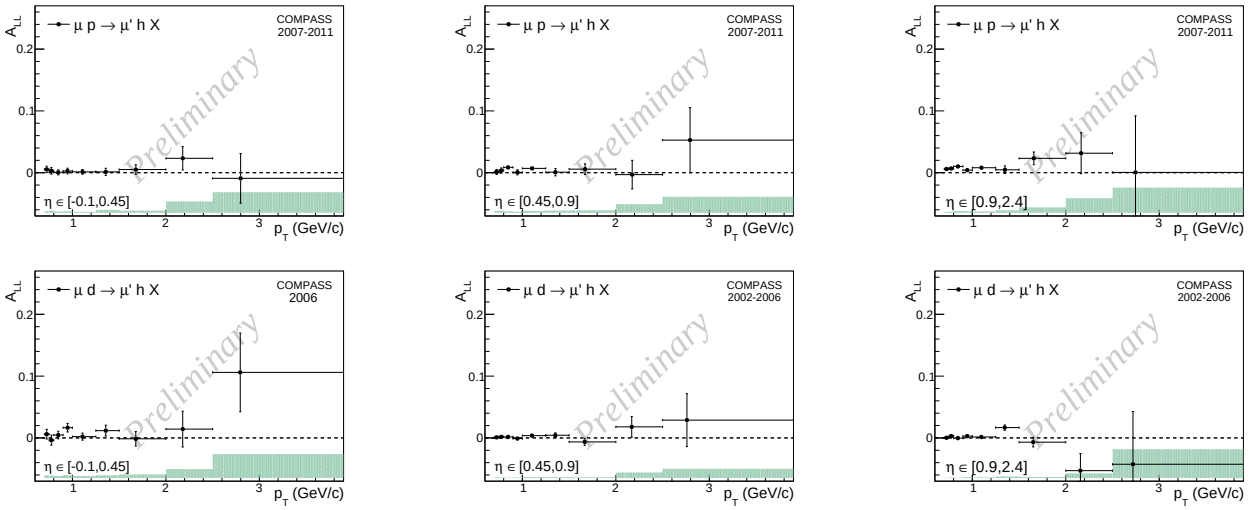

Fig. 13: A_{LL} asymmetries as function of p_T in three η bins for proton (top) and deuteron targets (bottom). The green band indicates the systematic uncertainty.

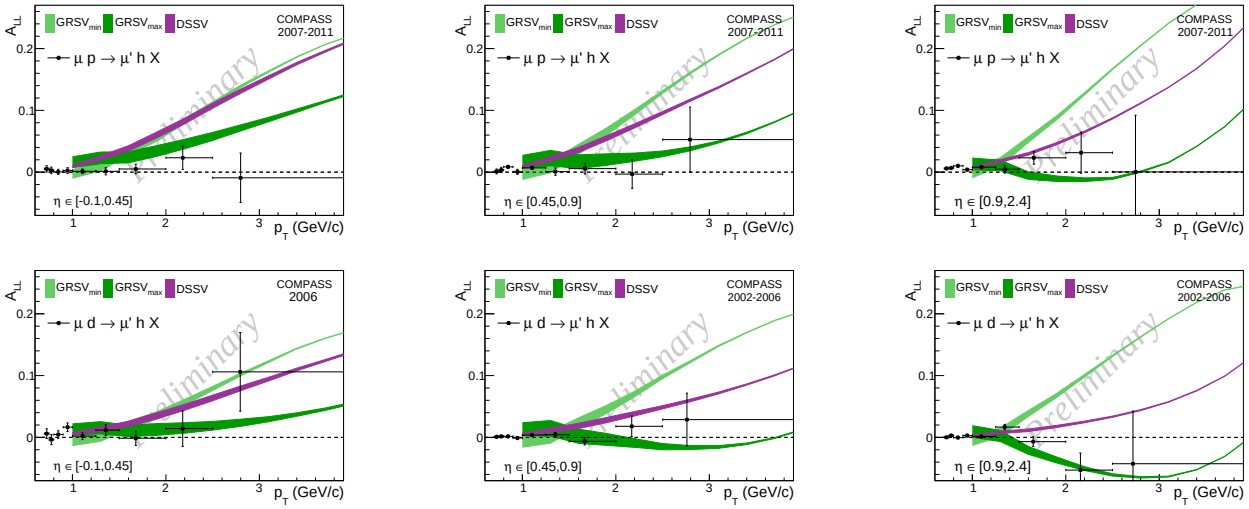

Fig. 14: Comparison of the measured A_{LL} asymmetries to NLO calculations using three different polarised gluon PDFs: GRSV_{min}, GRSV_{max}, and DSSV++ [23, 24] in three η bins as function of p_T for the proton (top) and the deuteron (bottom).

calculations.

3.3 Transverse structure of the nucleon and TMDs

3.3.1 The gluon Sivers asymmetry

The Sivers effect for gluons is connected to the gluon orbital angular momentum which may be the missing part in the nucleon spin. Last year we reported the measurement of the gluon Sivers asymmetry from a transversely polarised deuteron target. This analysis was extended to the 2010 transversely polarised proton data.

The Sivers asymmetry in the production of two high-p_T hadrons at large Q^2 receives contributions from three hard QCD subprocesses (see Sect. 3.2.1)

$$A_{UT}^{\sin(\phi_{2h}-\phi_s)} = R_{PGF} A_{PGF}^{\sin(\phi_{2h}-\phi_s)}(x_G) + R_{LP} A_{LP}^{\sin(\phi_{2h}-\phi_s)}(x) + R_{QDCC} A_{LP}^{\sin(\phi_{2h}-\phi_s)}(x_C), \tag{4}$$

where R_i are the relative contributions of the subprocesses. The fractions R_i as a function of the event kinematics are parameterised by a neural network trained on Monte Carlo samples. The minimisation process for

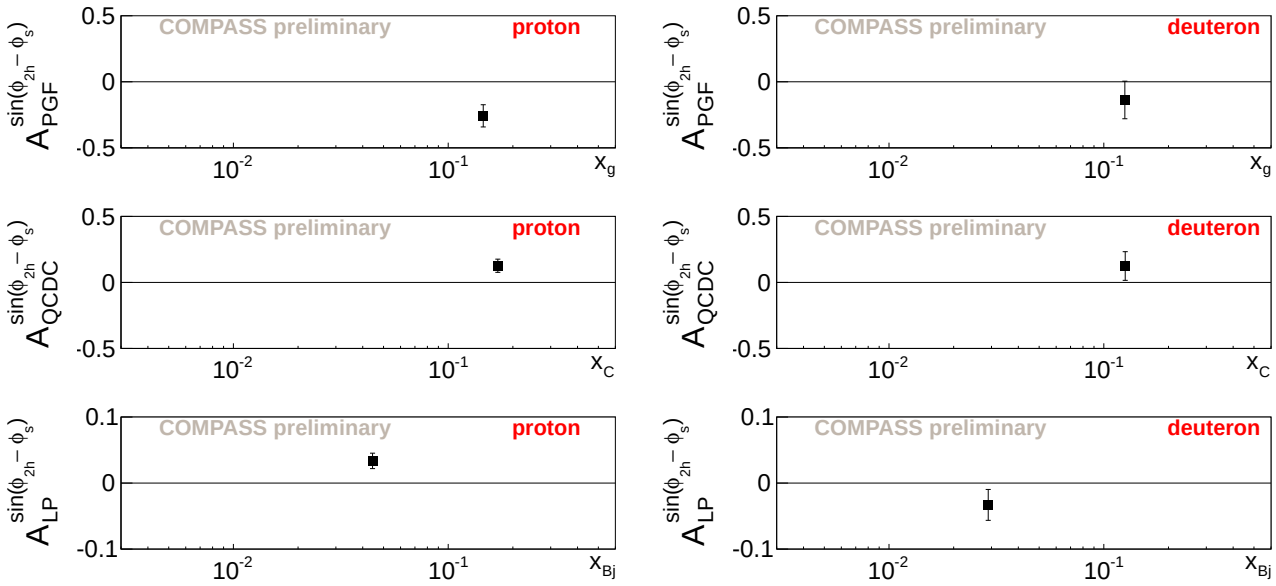

Fig. 15: Gluon Sivers (top) and QCDQ (middle) and LP Sivers (bottom) asymmetries for the proton (left) and the deuteron (right).

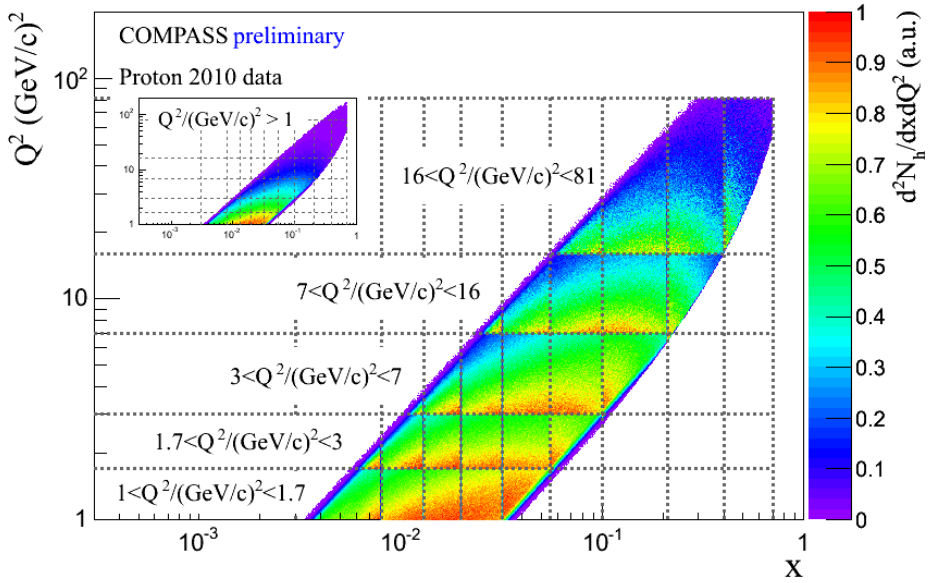

Fig. 16: Population of the (x, Q^2) bins for the multidimensional TSA analysis

.

the extraction of the three asymmetries is very similar to that described in Ref. 19 and Sect. 3.2.1 for the gluon polarisation. However, here only events with high-p_T are kept. For further details see last year's status report [14].

The Sivers asymmetry for the PGF process, i.e., the Sivers asymmetry for gluons is

$$\begin{aligned} &\text{proton:} && A_{PGF}^{\sin\phi_{2h}-\phi_S} = -0.26 \pm 0.09(\text{stat.}) \pm 0.08(\text{syst.}) \\ &\text{deuteron:} && A_{PGF}^{\sin\phi_{2h}-\phi_S} = -0.14 \pm 0.15(\text{stat.}) \pm 0.06(\text{syst.}) \end{aligned} \tag{5}$$

at $\langle x_G \rangle \simeq 0.15$. While the deuteron asymmetry was found to be negative, compatible with zero, the new proton result is two standard deviations below zero. The proton and deuteron results are compared in Fig. 15.

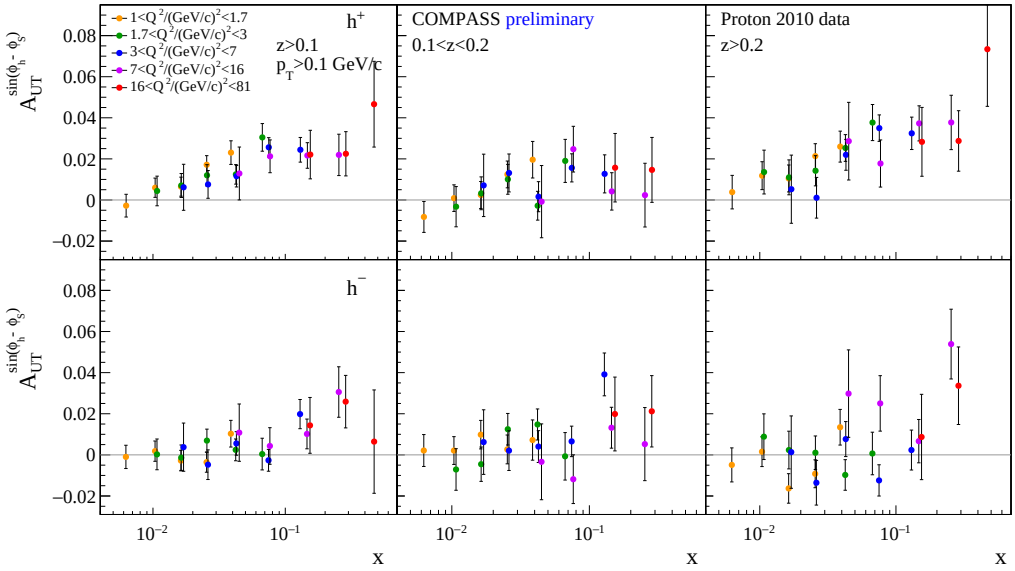

Fig. 17: The Sivers asymmetry for positive (top) and negative (bottom) hadrons as function of x for five Q^2 and three z ranges.

.

3.3.2 *Multidimensional analysis of transverse spin asymmetries*

Presently, the study of transverse-momentum-dependent (TMD) evolution of the parton distribution functions (PDFs) and fragmentation functions (FFs) and of the corresponding target-spin-dependent asymmetries (TSA) is a hot topic. Using standard SIDIS notations, the differential cross-section can be written in single-photon-exchange approximation as [29]

$$\frac{\mathrm{d}\sigma}{\mathrm{d}x\,\mathrm{d}y\,\mathrm{d}z\,p_T^h\,\mathrm{d}p_T^h\,\mathrm{d}\phi_h\,\mathrm{d}\psi} = 2\left[\frac{\alpha}{xyQ^2}\frac{y^2}{2\,(1-\varepsilon)}\left(1+\frac{\gamma^2}{2x}\right)\right](F_{UU,T}+\varepsilon F_{UU,L})$$

$$\times\Bigg\{1+\sqrt{2\varepsilon\,(1+\varepsilon)}A_{UU}^{\cos\phi_h}\cos\phi_h+\varepsilon A_{UU}^{\cos(2\phi_h)}\cos\left(2\phi_h\right)+\lambda\sqrt{2\varepsilon\,(1-\varepsilon)}A_{LU}^{\sin\phi_h}\sin\phi_h$$

$$+S_L\left[\sqrt{2\varepsilon\,(1+\varepsilon)}\sin\phi_h A_{UL}^{\sin\phi_h}+\varepsilon\sin\left(2\phi_h\right)A_{UL}^{\sin(2\phi_h)}\right]$$

$$+S_L\lambda\left[\sqrt{1-\varepsilon^2}A_{LL}+\sqrt{2\varepsilon\,(1-\varepsilon)}\cos\phi_h A_{LL}^{\cos\phi_h}\right]$$

$$+S_T\Big[A_{UT}^{\sin(\phi_h-\phi_S)}\sin\left(\phi_h-\phi_S\right)+\varepsilon A_{UT}^{\sin(\phi_h+\phi_S-\pi)}\sin\left(\phi_h+\phi_S-\pi\right)+\varepsilon A_{UT}^{\sin(3\phi_h-\phi_S)}\sin\left(3\phi_h-\phi_S\right)$$

$$+\sqrt{2\varepsilon\,(1+\varepsilon)}A_{UT}^{\sin\phi_S}\sin\phi_S+\sqrt{2\varepsilon\,(1+\varepsilon)}A_{UT}^{\sin(2\phi_h-\phi_S)}\sin\left(2\phi_h-\phi_S\right)\Big]$$

$$+S_T\lambda\Big[\sqrt{(1-\varepsilon^2)}A_{LT}^{\cos(\phi_h-\phi_S)}\cos\left(\phi_h-\phi_S\right)$$

$$+\sqrt{2\varepsilon\,(1-\varepsilon)}A_{LT}^{\cos\phi_S}\cos\phi_S+\sqrt{2\varepsilon\,(1-\varepsilon)}A_{LT}^{\cos(2\phi_h-\phi_S)}\cos\left(2\phi_h-\phi_S\right)\Big]\Bigg\}$$

with $\varepsilon = (1-y-\frac{1}{4}\gamma^2y^2)/(1-y+\frac{1}{2}y^2+\frac{1}{4}\gamma^2y^2)$, $\gamma = 2Mx/Q$ and the laboratory azimuthal angle ψ of the scattered lepton (in DIS kinematics $\mathrm{d}\psi \approx \mathrm{d}\phi_S$). The target transverse polarisation dependent part of this general expression contains eight modulations[1] in the azimuthal angles of the produced hadron ϕ_h and of the nucleon spin ϕ_S. The amplitude of each modulation is given by the corresponding asymmetry $A^{f(\phi_h,\phi_s)}$. Five amplitudes depend only on the target spin S_T, while the three others also depend on the beam/photon polarisation λ.

[1]The twist-2 amplitudes are marked in red and higher-twist amplitudes in blue

The relation between the four leading-twist asymmetries and the TMD PDFs and FFs is given by

$$\begin{aligned} A_{UT}^{\sin(\phi_h-\phi_S)} &\propto f_{1T}^{\perp q}\otimes D_{1q}^{h}, & A_{UT}^{\sin(\phi_h+\phi_S-\pi)} &\propto h_1^q\otimes H_{1q}^{\perp h} \\ A_{UT}^{\sin(3\phi_h-\phi_S)} &\propto h_{1T}^{\perp q}\otimes H_{1q}^{\perp h}, & A_{LT}^{\cos(\phi_h-\phi_S\quad)} &\propto g_{1T}^{q}\otimes D_{1q}^{h}, \end{aligned} \tag{6}$$

where h_1^q, $f_{1T}^{\perp q}$, $h_{1T}^{\perp q}$ and g_{1T}^q indicate transversity, Siver PDF, pretzelosity, and worm gear PDF, respectively. The PDFs are coupled to the normal unpolarised FF D_{1q}^h or to the Collins FF $H_{1q}^{\perp h}$.

We determine simultaneously the eight transverse spin asymmetries for positive and negative unidentified hadrons using an unbinned likelyhood method using the 2010 proton data. The multidimensional analysis uses a grid in (x, z, p_T, Q^2) with bin boundaries in Q^2 of (1, 1.7, 3, 7, 16, 81) (GeV/c)^2 and in x of (0.003, 0.008, 0.013, 0.02, 0.032, 0.055, 0.1, 0.21, 0.4, 0.7) (Fig. 16). In addition the following cuts are applied $0.1 < y < 0.9$, $W > 5$ GeV/c^2, and for the hadron $p_T > 0.1$ GeV/c and various z ranges. Systematic uncertainties caused by detector instabilities and acceptance effects were studied. Furthermore the statistical compatibility of repeated measurements was checked. Possible effects due to the slight deviation of the photon direction and the beam direction were also considered. The systematic uncertainty is always smaller than 0.75 times the statistical uncertainty.

As a result, we have a huge, highly differential data set for the eight asymmetries, which will have a strong impact on model-building for TMDs. Figure 17 shows as an example the Sivers asymmetry $A_{UT}^{\sin(\phi_h-\phi_S)}$.

3.3.3 Single and dihadron transverse asymmetries in a dihadron sample

The similarity among the Collins asymmetry for positive and for negative hadrons [30] and the dihadron asymmetry as functions of x has let us to further investigate the single-hadron asymmetries in the dihadron sample taken 2010 with a polarised NH_3 (proton) target.

The cross-section for inclusive dihadron production, $\mu N \to \mu' h^+ h^- X$, can be written as [31][2]

$$\frac{\mathrm{d}\sigma^{h_1h_2}}{\mathrm{d}\phi_1\,\mathrm{d}\phi_2\,\mathrm{d}\phi_S} = \sigma_{\mathrm{U}} + S_T(\sigma_{\mathrm{S}}+\sigma_{\mathrm{C}}), \tag{7}$$

with the Sivers-like and Collins-like terms

$$\begin{aligned} \sigma_{\mathrm{S}} &= \sigma_{1\mathrm{S}}\sin(\phi_1-\phi_S) + \sigma_{2\mathrm{S}}\sin(\phi_2-\phi_S) \\ \sigma_{\mathrm{C}} &= \sigma_{1\mathrm{C}}\sin(\phi_1+\phi_S-\pi) + \sigma_{2\mathrm{C}}\sin(\phi_2+\phi_S-\pi). \end{aligned} \tag{8}$$

The indices 1,2 refer to the two hadrons and ϕ_S is the azimuthal angle of the transverse spin. The structure functions $\sigma_{\mathrm{U/C/S}}$ depend in general on $\Delta\phi = \phi_1 - \phi_2$. The cross-sections can alternatively be expressed as a function of $\Delta\phi$ and ϕ_1 instead of ϕ_1 and ϕ_2 leading to the following 'Collins-like' asymmetries $A_{\mathrm{CL}} = \sigma/(D_{NN}\sigma_{\mathrm{U}})$

$$\begin{aligned} A_{1\mathrm{CL}}^{\sin(\phi_1+\phi_S-\pi)} &\propto \sigma_{1\mathrm{C}} + \sigma_{2\mathrm{C}}\cos\Delta\phi \\ A_{2\mathrm{CL}}^{\sin(\phi_2+\phi_S-\pi)} &\propto \sigma_{2\mathrm{C}} + \sigma_{1\mathrm{C}}\cos\Delta\phi \\ A_{1\mathrm{CL}}^{\cos(\phi_1+\phi_S-\pi)} &\propto -\sigma_{2\mathrm{C}}\sin\Delta\phi \\ A_{2\mathrm{CL}}^{\cos(\phi_2+\phi_S-\pi)} &\propto \sigma_{1\mathrm{C}}\sin\Delta\phi \end{aligned} \tag{9}$$

Thus for $\sigma_{1\mathrm{C}}(\Delta\phi) = -\sigma_{2\mathrm{C}}(\Delta\phi)$ and $\sigma_{1,2\mathrm{C}}(\Delta\phi)/\sigma_{\mathrm{U}}(\Delta\phi)$ independent of $\Delta\phi$, the cosine asymmetries of Eq. 9 are equal for the positive and negative hadrons, while for the sine asymmetries this leads to a mirror symmetry. This is exactly, what is observed in the data (Fig. 18).

[2] Note the extra π term, which is due to different conventions.

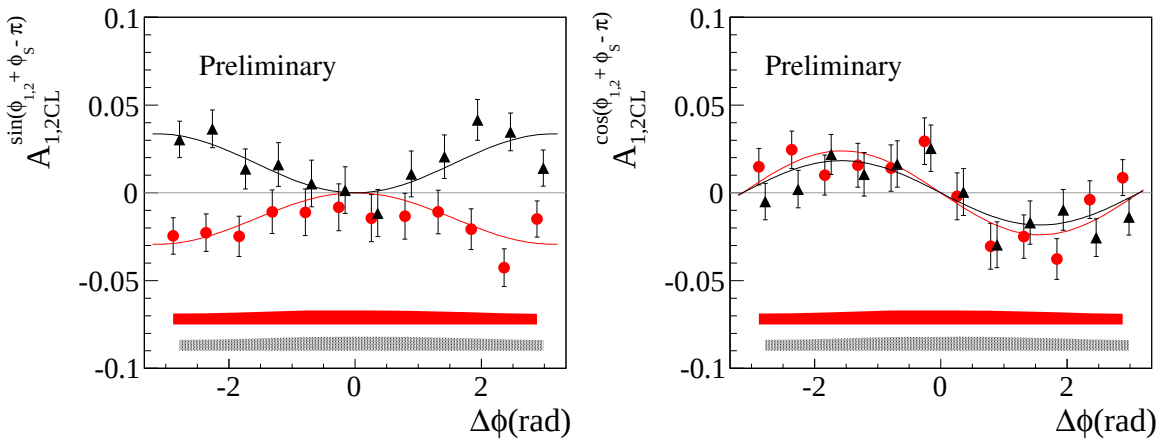

Fig. 18: Collins-like asymmetries for positive (1) and negative (2) hadrons in the dihadron sample as function of $\Delta\phi$. The curves show fits according to Eq. 9 assuming $\sigma_{1C} = -\sigma_{2C}$.

So far we have discussed the single-hadron asymmetries in the dihadron sample. Using the verified relation $\sigma_{1C} = -\sigma_{2C}$ and the dihadron azimuthal angle ϕ_{2h} of the vector $\vec{R}_N = \hat{p}_{T1} - \hat{p}_{T2}$ one can study the relation of dihadron and single-hadron asymmetries in the dihadron sample. The angle ϕ_{2h} is also the azimuthal angle of $\hat{p}_{T1} + \hat{p}_{T2}$ plus or minus $\pi/2$ depending on the quadrant. It is thus kind of an average azimuthal angle for the hadron pair. Using the angle $\phi_{2h,S} = \phi_{2h} + \phi_S - \pi$ yields essentially the same dihadron asymmetries as the standard angle ϕ_{RS} [30].

We find $A_{2h,\mathrm{CL}}^{\sin(\phi_{2h}+\phi_S-\pi)} \propto \sqrt{2(1-\cos\Delta\phi)}$ [32]. Integrating this asymmetry and the corresponding single-hadron asymmetry of Eq. 9 over $\Delta\phi$, we find a ratio of $4/\pi$ in agreement with our previous observation that dihadron asymmetry is somewhat larger than the single-hadron Collins asymmetry.

A similar analysis was performed for the Sivers-like asymmetries in the dihadron sample. However, the relation $\sigma_{1S} = -\sigma_{2S}$ does not hold.

3.4 GPDs and exclusive omega production

We have performed a complete measurement of the five transverse target-single-spin asymmetries A_{UT} and the three transverse target double-spin asymmetries A_{LT} for exclusive ω muoproduction from transversely polarised protons. The data were taken in 2010 with a polarised NH_3 target. Therefore no recoil detector could be used. Exclusive ω production events are selected on basis of the invariant missing mass.

These asymmetries are sensitive to all types of GPDs, including the chiral-odd or 'transverse' GPDs H_T and $\overline{E_T}$ related to transversity and Boer-Mulders TMDs, respectively. In particular, the leading-twist asymmetry $A_{UT}^{\sin(\phi-\phi_S)}$ is sensitive to the chiral-even GPDs E, which are linked to the orbital angular momentum of quarks. This analysis complements the exclusive ρ^0 production studies [34, 35]. The phenomenological GPD model of Goloskokov and Kroll [33] predicts a sizeable value for the asymmetry $A_{UT}^{\sin(\phi-\phi_S)}$ for ω and a small one for ρ^0. The difference between both predictions can be explained by the different quark contribution in flavour-dependent wave function of the mesons. The combinations of GPDs E contributing to these two processes are:

$$\begin{aligned} E^{\rho^0} &= \frac{1}{\sqrt{2}}\left(\frac{2}{3}E^u + \frac{1}{3}E^d + \frac{3}{8}E^g\right) \\ E^{\omega} &= \frac{1}{\sqrt{2}}\left(\frac{2}{3}E^u - \frac{1}{3}E^d + \frac{3}{8}E^g\right). \end{aligned} \tag{10}$$

There is a cancellation to a large extent between the small gluon and sea contributions. The contributions from the GPDs E^u and E^d are large but with opposite sign and the resulting contribution is therefore smaller for ρ than for ω. However, the GPDs contribution for ω production is entangled with pion-exchange contribution

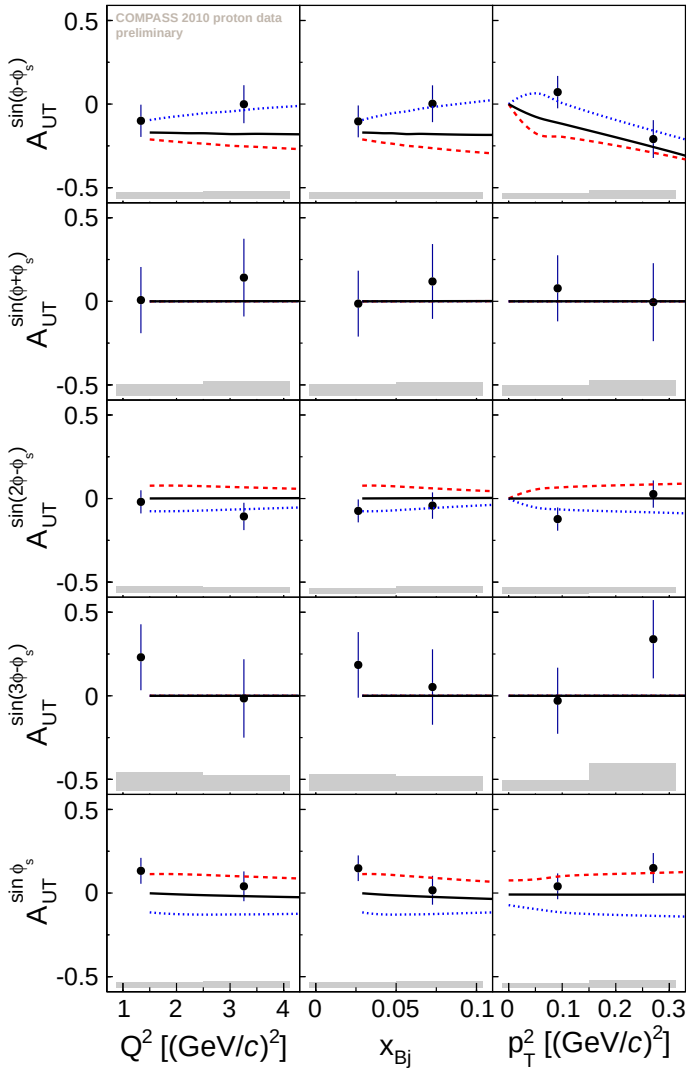

Fig. 19: Final results for the five transverse target single-spin asymmetries A_{UT}. The curves show the predictions of the GPD model [33]. They are calculated for the average W, Q^2 and p_T^2 of the COMPASS data set, W = 7.1 GeV/c^2 and p_T^2 = 0.17 (GeV/c)^2 for the left and middle panels and W = 7.1 GeV/c^2 and Q^2 = 2.2 (GeV/c)^2 for the right panels. The dashed red and dotted blue curves represent the predictions with the positive and negative contributions of the pion pole, respectively, while the solid black curve represents the predictions without the pion pole.

which is rather small for ρ production. The result of the five transverse target single-spin asymmetries A_{UT} is presented in Fig. 19 and compared to the GPD model with and without the addition of the pion pole contributions. The sign of the $\pi\omega$ transition form factor is not yet known and our results do not allow its unambiguous determination.

4 Hadron multiplicities: TMDs and fragmentation functions

4.1 Quark fragmentation functions from pion and kaon multiplicities

The analysis of the multiplicities of unidentified hadrons, identified pions and kaons from the 2006 isoscalar ^{6}LiD target has been finalised. The data are analysed in a 3-dimensional grid in the kinematic variables $0.1 < y = \nu/E_\mu < 0.7$, and $0.2 < z = E_h/\nu < 0.85$ with $Q^2 > 1$ (GeV/c)^2 and 5 GeV/c^2 $< W <$ 18 GeV/c^2, where ν is the energy of the virtual photon. The pion data cover to $0.004 < x < 0.7$, while the kaon statistics implies $x < 0.4$.

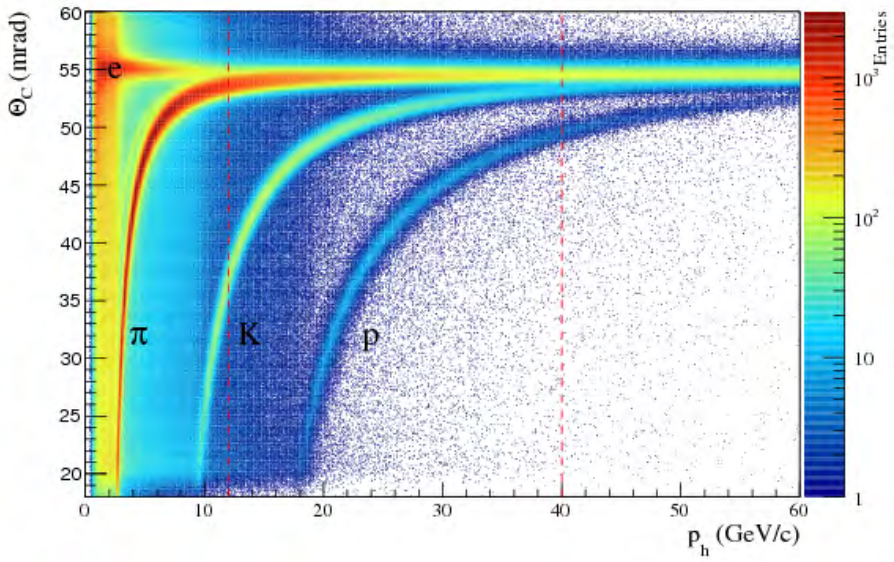

Fig. 20: Measured Cherenkov angle as function of particle momentum p_h. Vertical dashed lines indicate the momentum selection cuts.

The multiplicities are defined as the differential cross-section for hadron production normalised to the inclusive DIS cross-section. They depend on unpolarised PDFs $q(x, Q^2)$ and FFs $D_q^h(z, Q^2)$

$$\frac{\mathrm{d}^3\sigma^h(x,z,Q^2)/\mathrm{d}x\,\mathrm{d}Q^2\,\mathrm{d}z}{\mathrm{d}^2\sigma^{DIS}(x,Q^2)/\mathrm{d}x\,\mathrm{d}Q^2} = \frac{\sum_q e_q^2\, q(x,Q^2)\, D_q^h(z,Q^2)}{\sum_q e_q^2\, q(x,Q^2)}\ . \tag{11}$$

The multiplicity measurement is corrected for the finite detector acceptance using a Monte Carlo simulation containing approximately 400 million events. The events are generated using LEPTO with MSTW08 PDFs and JETSET with COMPASS high-p_T tuning [19]. For secondary interaction FLUKA is used, which better reproduces the p_T dependence of the data than GHEISHA. The acceptance is large, typically above 60%, only for $z = 0.8$, $0.15 < x < 0.7$ and $0.1 < y < 0.15$ it drops below 40%. Further corrections are applied for diffractive vector meson production of ρ for the pion data and of ρ and ϕ for the kaon data.

The experimental multiplicities are affected by QED radiative effects, which introduce a systematic bias of the observed kinematics with respect to the true kinematics. The most important contributions at first order are the initial and final state radiation of a real photon by the incoming and the outgoing lepton. The bias on the muon kinematics upon real photon emission affects in turn the reconstruction of the hadron energy fraction z. This effect is not taken into account so far. In this analysis, the DIS events and hadron yields are corrected on an event-by-event basis using the inclusive corrections for DIS yields and semi-inclusive corrections for hadron yields. For the time being we attribute a 100% uncertainty to the latter.

Hadrons are identified using a maximum likelihood criterion based on the RICH information (Fig. 20). A momentum range of 12 GeV/$c < p_K <$ 40 GeV/c is available for kaon identification. The event yields for the different hadron species are unfolded using the measured RICH identification and misidentification efficiencies. Figure 21 shows the final multiplicities for positive and negative kaons, M^{K^+} and M^{K^-}. The multiplicities integrated over $0.2 < z < 0.85$ and averaged over $0.1 < y < 0.7$ for pions and kaons are shown in Fig. 22. While our data agree well with the LEPTO/JETSET Monte Carlo (only shown for kaons), they clearly disagree with the results from HERMES. The HERMES pion multiplicities [36] are larger and their kaon multiplicities [37] are smaller for all x compared to the COMPASS results. Also the shapes are rather different. Here a clarification is pending. The COMPASS multiplicities do not show a strong x dependence; in particular no rise of the kaon multiplicities toward small x where the strange quarks a more abundant.

We have also performed LO fits to the COMPASS pion and kaon data to extract the FFs. The relation between

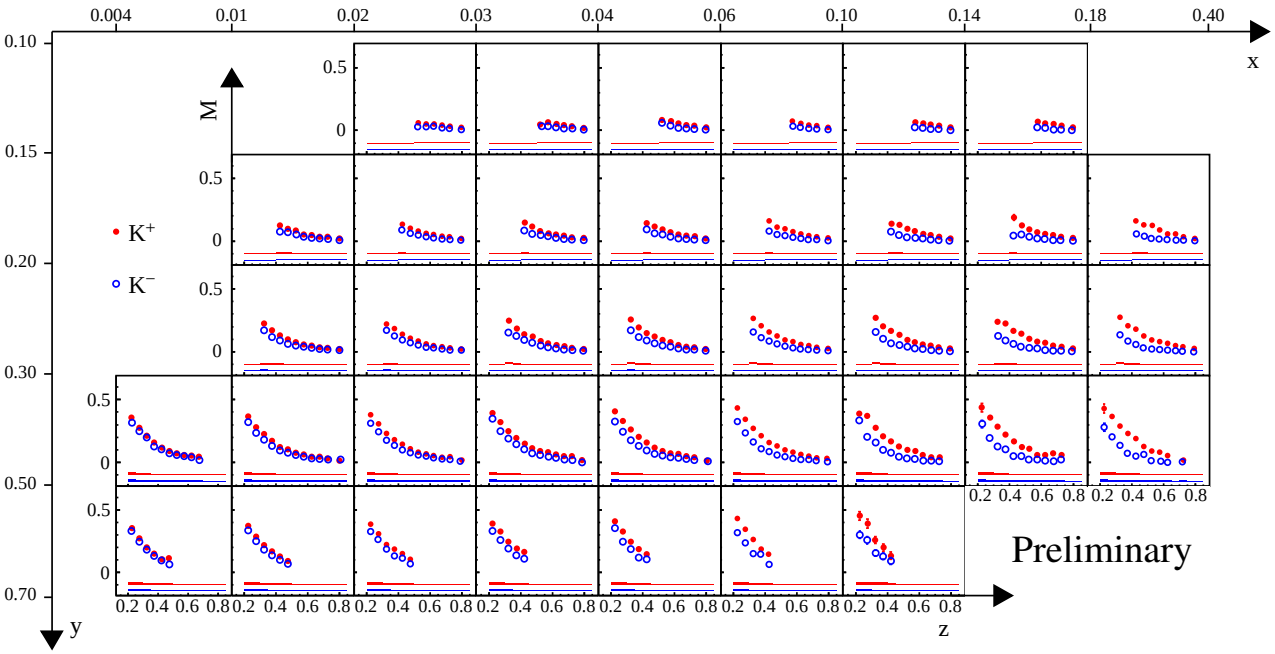

Fig. 21: Kaon multiplicities as a function of z for (x, y) bins. The red markers correspond to positive kaons and the blue markers to negative kaons. Both diffractive vector meson and acceptance corrections are applied. The asymmetric systematic errors for radiative correction on kaons do not extend above the markers, i.e. the systematics related to the radiative correction are not shown. All other systematic errors are shown as bands.

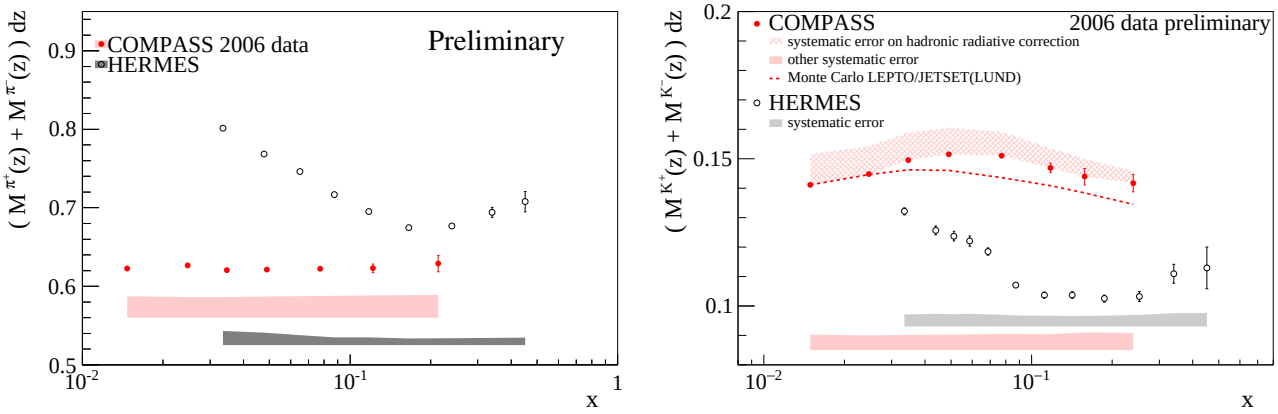

Fig. 22: Charged pion (left) and kaon (right) multiplicities as function of x; COMPASS $0.1 < y < 0.7$; $0.2 < z < 0.85$; HERMES $0.1 < y < 0.85$; $0.2 < z < 0.80$; bands show the systematic uncertainties.

multiplicities and FFs in LO is given by

$$M^h = \frac{1}{N^{DIS}(x,Q^2)} \frac{\mathrm{d}N^h}{\mathrm{d}x\,\mathrm{d}z\,\mathrm{d}Q^2} = \frac{\sum_q e_q^2 q(x,Q^2) D_q^h(z,Q^2)}{\sum_q e_q^2 q(x,Q^2)} \tag{12}$$

Imposing isospin and charge symmetry for the FFs and assuming $D_s^{\pi^\pm} = D_{\overline{u}}^{\pi^+}$, only the glue FF and two independent quark FFs survive, the favoured and the unfavoured one. For the kaons the favoured strange FF is fitted with separate parameters. The fit was performed using MSTW08 for the PDFs and the functional form for the FFs (γ and δ fixed to zero for strange favoured, unfavoured and glue FFs and for the pion multiplicities).

$$zD_i(z,Q_0^2) = N_i z^{\alpha_i}(1-z)^{\beta_i}[1+\gamma_i(1-z)^{\delta_i}] \tag{13}$$

Figure 23 shows COMPASS results for the quark-to-pion and quark-to-kaon favoured and unfavoured FFs ob-

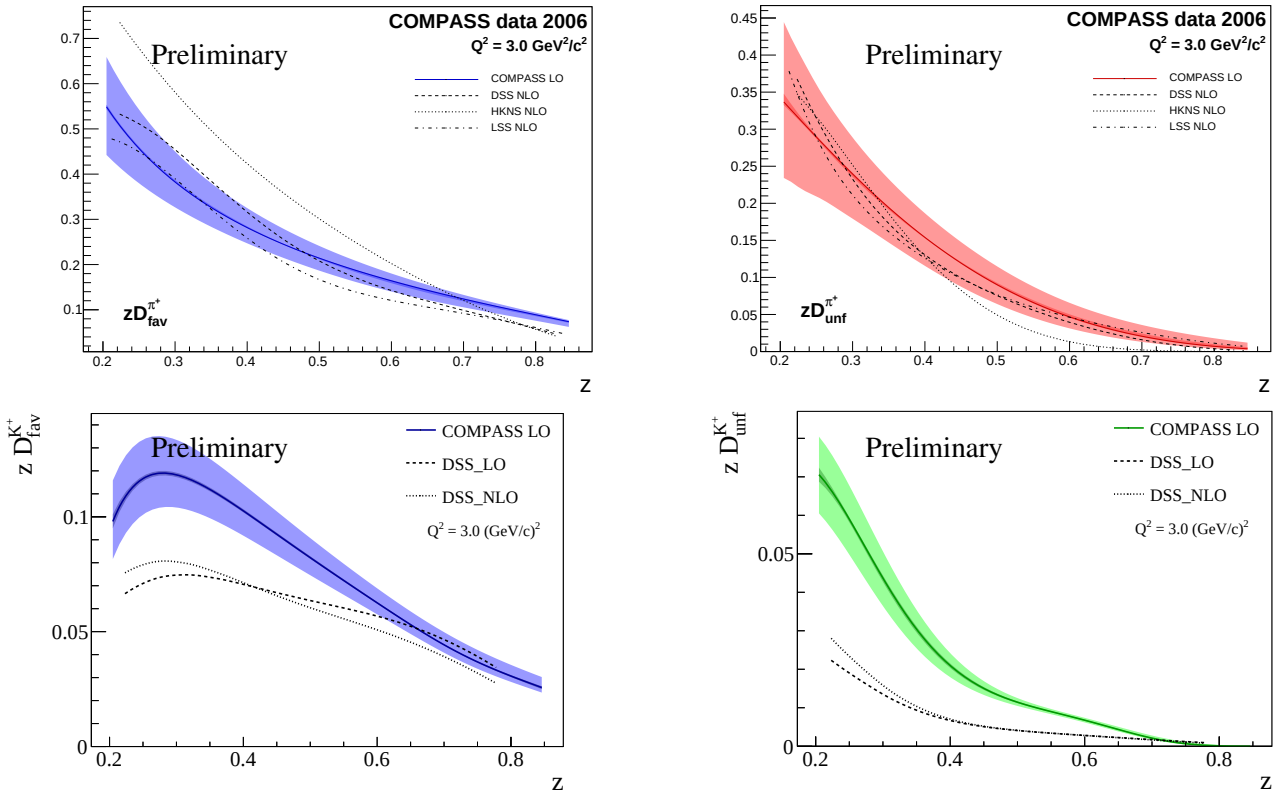

Fig. 23: Favoured (left) and unfavoured (right) LO fragmmentation functions for pions (top) and kaons (bottom).

tained from the LO fit to COMPASS data alone. The pion results are in good agreement with the DSS parametrisations [25], however for the kaon we obtain both larger favoured and unfavoured FFs.

Isospin symmetry links the charged and neutral kaon FFs, e.g.

$$D_u^{K^+ + K^-} = D_d^{K^0 + \overline{K^0}}. \tag{14}$$

Thus neutral kaons can help to further clarify the situation. Work on this analysis has started.

4.2 Transverse-momentum-dependent hadron multiplicities

Unpolarised transverse-momentum-dependent parton densities (TMD-PDFs) and fragmentation functions (TMD-FFs), commonly often referred to as TMDs, can be assessed by measuring the hadron yields normalised to the yields of DIS interactions, i.e. hadron multiplicities. While the study of the z dependence of the hadron multiplicities is sensitive to the hadronisation in the collinear framework, the dependence upon the transverse momentum of the final hadron p_T gives access to the transverse structure of the nucleon and the formation process of the hadron. The transverse momentum is generated by the transverse momentum of the struck quark $k_\perp$ and the transverse momentum $p_\perp$ of the final hadron with respect to the fragmenting quark. The multiplicities are given by

$$\frac{\mathrm{d}^4 M^h(x, Q^2, z, p_T^2)}{\mathrm{d}x\, \mathrm{d}Q^2\, \mathrm{d}z\, \mathrm{d}p_T^2} = \frac{1}{\mathrm{d}^2\sigma^{\mathrm{DIS}}(x, Q^2)/\mathrm{d}x\, \mathrm{d}Q^2} \frac{\mathrm{d}^4\sigma(x, Q^2, z, p_T^2)}{\mathrm{d}x\, \mathrm{d}z\, \mathrm{d}Q^2\, \mathrm{d}p_T^2} \tag{15}$$

$$= \frac{\sum_q e_q^2 f_q(x, k_\perp, Q^2) D_{h/q}(z, p_\perp, Q^2)}{\sum_q e_q^2 f_q(x, k_\perp, Q^2)}. \tag{16}$$

A recent fit [38] to the existing data sets, including 2004 COMPASS data [39], was performed assuming Gaussian

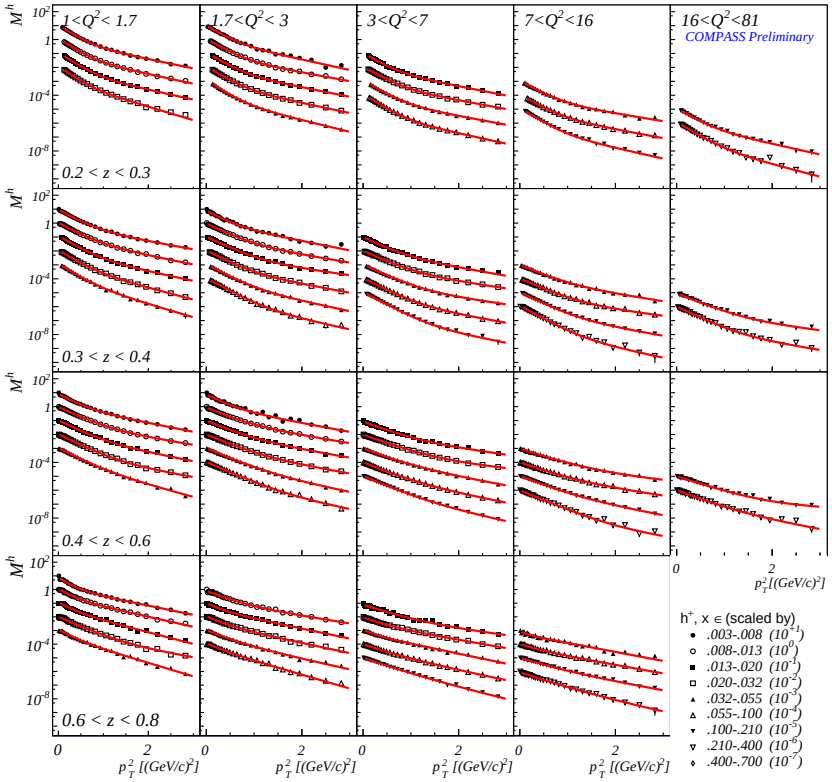

Fig. 24: Multiplicities of positive hadrons as function of p_T^2 in Q^2 (columns) and z bins (rows) and for various regions in x.

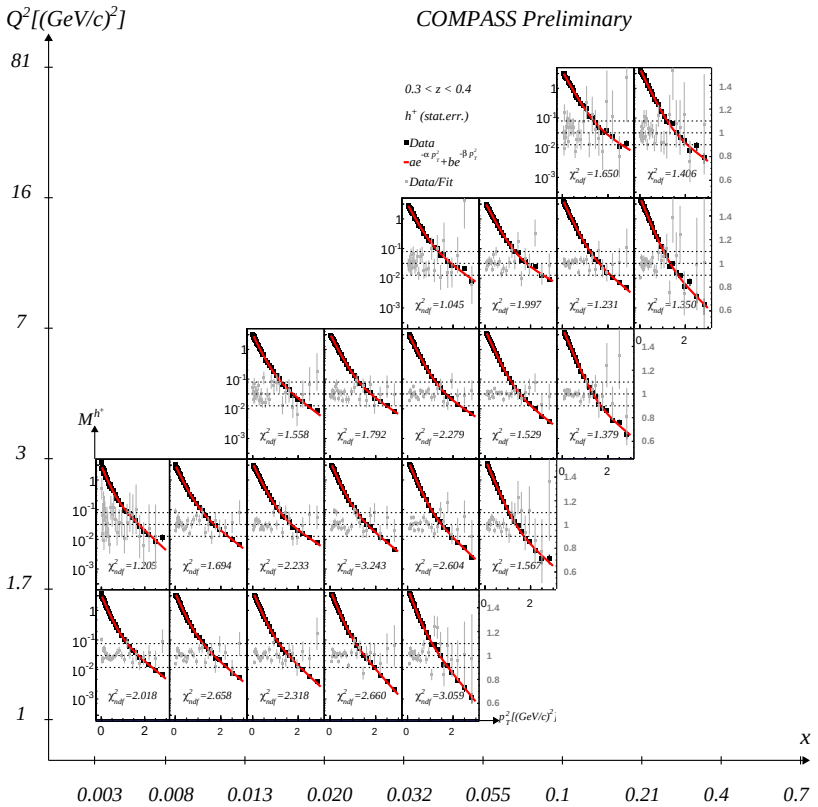

Fig. 25: Multiplicities of positive hadrons as function of p_T^2 in x (columns) and Q^2 (rows) for $0.3 < z < 0.4$ fitted by two exponentials. The deviations from the fit are shown in grey.

parametrisations for the TMDs $f_q(x, k_\perp)$ and $D_{h/q}(z, p_\perp)$. This fit has shown that this ansatz is not suitable to describe the shape of our data.

We analysed the hadron multiplicities of the 2006 isoscalar data set (^{6}LiD, same data as in previous subsection) in a 4-dimensional grid of Q^2, x, z, and p_T^2. In total 4.3 million positive hadrons and 3.4 million negative hadrons in the range $0.2 < z < 0.8$ entered the analysis. The contribution from diffractive vector meson production has been estimated, but a correction was not applied for the time being. It affects mainly the region $p_T < 1$ GeV/c. Its highest values of about 40% appears for $z > 0.75$, $Q^2 < 2$ (GeV/c)^2, and $p_T < 0.5$ (GeV/c)^2. The multiplicities of the positive hadrons are shown as example in Fig. 24. Systematic uncertainties have been evaluated, but are not shown here for clarity.

The multiplicities can not be fitted using a single exponential in p_T^2, therefore a two-exponential function $M = ae^{-\alpha p_T^2} + be^{-\beta p_T^2}$ as used. The fits describe the data well (Fig. 25). The data provide valuable input for the QCD analysis of TMDs.

5 Analysis of the DVCS 2012 data

A first measurement of the deeply virtual Compton scattering using the 160 GeV high energy muon beam of SPS and the final set-up to adapt the COMPASS spectrometer for exclusive measurement has been performed in November 2012. This set-up comprises a 2.5 m long liquid Hydrogen (LH_2) target surrounded by a new 4 m long recoil detector named CAMERA, and a new electromagnetic calorimeter ECAL0 to extend the angular acceptance for photon detection. In 2012 only the central part of ECAL0 (25% of the complete detector) was installed. The DVCS data taking consists of 5 periods of a few days each using alternately positive and negative muon beams. The goal was to determine the performance of the setup and to select exclusive single photon events $\mu p \to \mu' \gamma p$ to study the two contributions of Bethe-Heitler (BH) when the photon is radiated by the initial or final lepton and of deeply virtual Compton scattering (DVCS) which are parameterised by the Generalised Parton Distributions (GPDs) to describe the 3D structure of the nucleon.

Thanks to the recoil proton detector CAMERA, we can select exclusive single photon production by a comparison of the observables given only by the spectrometer or by CAMERA. We denote k, k', q, q', p, p' the four-momenta of the incident muon, outgoing muon, virtual photon, real photon, target proton, outgoing proton respectively, $t = (q - q')^2 = (p - p')^2$ the transfer to the proton target, ν the energy of the virtual photon in the lab, E_γ and E_p the energies of the real photon and the outgoing proton in the lab respectively.

Without the use of CAMERA the exclusive reaction $\mu p \to \mu' \gamma p$ can be selected with the detection of only the incident and outgoing muons and the photon using a cut on the missing mass of a particle which should be a proton (or on the missing energy):

$$\begin{aligned} M_{miss}^2 &= M_{X=p'}^2 = (k + p - k' - q')^2 = 2\mathrm{m_p}(\nu - E_\gamma) + {\mathrm{m_p}}^2 + t \\ E_{miss} &= (M_{miss}^2 - {\mathrm{m_p}}^2)/2\mathrm{m_p} = \nu - E_\gamma + t/2\mathrm{m_p} \end{aligned} \tag{17}$$

Detection of proton in CAMERA allows to perform a cut on the missing mass of a particle:

$$M_{undet}^2 = M_{X=0}^2 = (k + p - k' - q' - p')^2 = 2(\mathrm{m_p} - E_p)(\nu - E_\gamma - E_p) + t \tag{18}$$

With CAMERA we can also build the differences between azimuthal angles and transverse momenta of the proton (respectively to the direction of the incident muon) using either the forward spectrometer only or directly CAMERA:

$$\begin{aligned} \Delta\varphi &= \varphi_{miss} - \varphi_{CAMERA} \\ \Delta p_\perp &= |p_\perp^{miss}| - |p_\perp^{CAMERA}| \end{aligned} \tag{19}$$

We can also compare the Z position of the hits in the inner CAMERA ring given either by the scintillating counter or by the interpolation between the vertex given by the spectrometer and the outer ring:

$$\Delta Z = Z_{ringA} - Z_{interp.} \tag{20}$$

Figure 26 shows the distributions of $\Delta\varphi$, $\Delta p_\perp$, M^2_{undet} and ΔZ. The exclusivity cuts are the following: $|\Delta\varphi| <$ 0.4 rad, $|\Delta p_\perp| < 0.3$ GeV/c, $|M^2_{undet}| < 0.3$ (GeV/c^2)^2 and $|\Delta Z|$ <16 cm. The distributions are compared to MC simulations of BH and DVCS using the HEPGEN/BH+DVCS generator and the TGEANT/CORAL/PHAST chain. The agreement between MC and data is reasonably good.

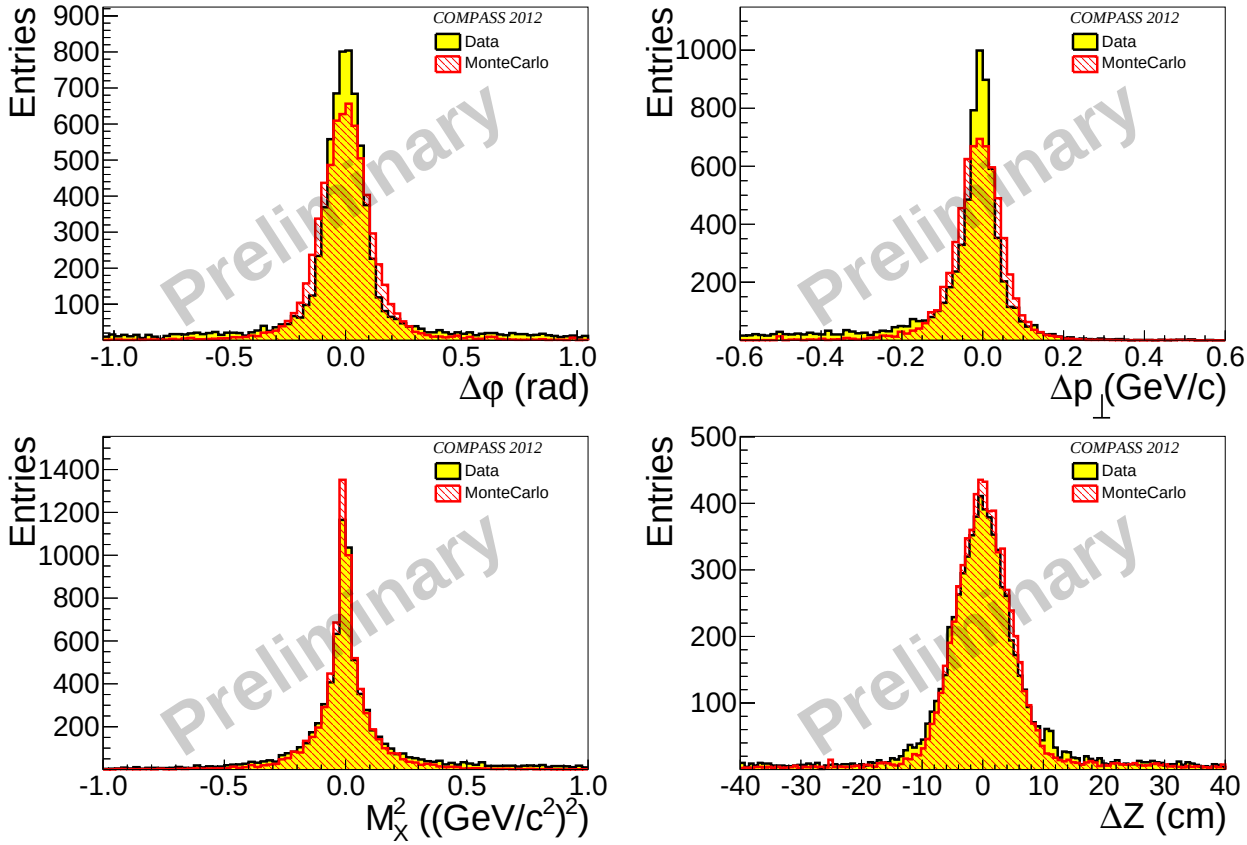

Fig. 26: Distributions of events for $\Delta\varphi$ (top left), $|\Delta p_\perp|$ (top right), $|M^2_{undet}|$ (bottom left) and $|\Delta Z|$ distribution (bottom right). For each distribution the cuts on the other distributions are applied. The data are in yellow, the MC simulation using HEPGEN/BHDVCS generator and the TGEANT/CORAL/PHAST chain is in red.

π^0-mesons are one of the main background sources for exclusive single photon production. We can consider two possible cases:

– *the visible* π^0. The exclusive photon candidates contained in the selected sample have been associated with all other possible background photons (of energy smaller than the requested thresholds) in the same event and the invariant mass of the 2 photons is reconstructed. Fig. 27 clearly shows that it remains visible π^0 in the sample previously selected. We call this contribution "visible" π^0 background. 128 events in the peak determined by a cut of $\pm$20 MeV/c^2 around the PDG π^0 mass can be identified as such and are mainly localised in the large x_{Bj} bin which contains 1268 events. This visible π^0 contribution is subtracted from the exclusive single photon sample.

– *the invisible* π^0 *when one photon is lost.* The π^0 contamination can originates either from semi-inclusive production or from exclusive production. They can be evaluated using a MC based on the LEPTO generator for the first case and on the HEPGEN/π^0 generator for the later. MC samples can be normalised

in order to reproduce the visible π^0 in the real data. Two extreme cases are considered, either a fully semi-inclusive background, or a fully exclusive background and they are used to provide upper and lower limits for the contamination to BH and DVCS events.

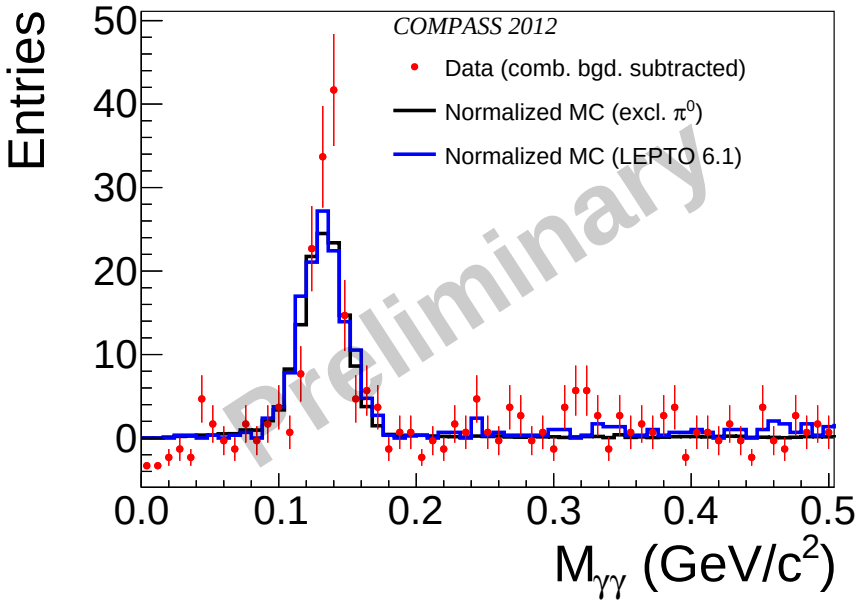

Fig. 27: Two photon invariant mass in the selected exclusive single photon sample. Clearly it remains a "visible" π^0 contribution in the data which can be compared to a contamination given either by exclusive π^0 production (MC/HEPGEN/PI0) or by semi-inclusive π^0 production (MC/LEPTO).

Fig. 28 presents the exclusive single photon events obtained in the 2012 sample as a function of the azimuthal angle $\phi_{\gamma^*\gamma}$ between the leptonic and hadronic planes as well as the BH estimation and the invisible π^0 contamination estimated by LEPTO as upper and by HEPGEN/PI0 as lower bound. Note, that no radiative corrections are applied. At small x_{Bj} the BH is supposed to dominate and give the normalisation of the MC/HEPGEN/BH prediction. At large x_{Bj} we can see the BH contribution, the one photon from π^0 contribution which is maximised and it remains room for a "pure" DVCS contribution. The analysis of the t-dependence of the "pure" DVCS contribution is on going.

6 Drell–Yan

In this section we discuss the status of analysis for the 2014 unpolarised Drell–Yan run and the status of the 2015 run with a polarised NH_3 target.

6.1 Experimental set-up

The apparatus used in the COMPASS DY measurements includes some modifications with respect to the one used for SIDIS, DVCS and hadron spectroscopy. The distinctive features of the set-up are the following:

- a negative hadron beam (97% π^-, 2.5% K^- and 0.5% $\bar{p}$) with momentum 190 GeV/c and intensity reaching up to 10^8 particles/s.
- a long NH_3 target, transversely polarisable, followed by 2 nuclear targets (aluminium and tungsten).
- a long hadron absorber to stop hadronic products of interaction, with a tungsten beam plug as inner core, with the double purpose of stopping the remaining beam, and acting as nuclear target itself.
- a large acceptance trigger system detecting multimuon events.
- a radiation-hard beam telescope with excellent time resolution.

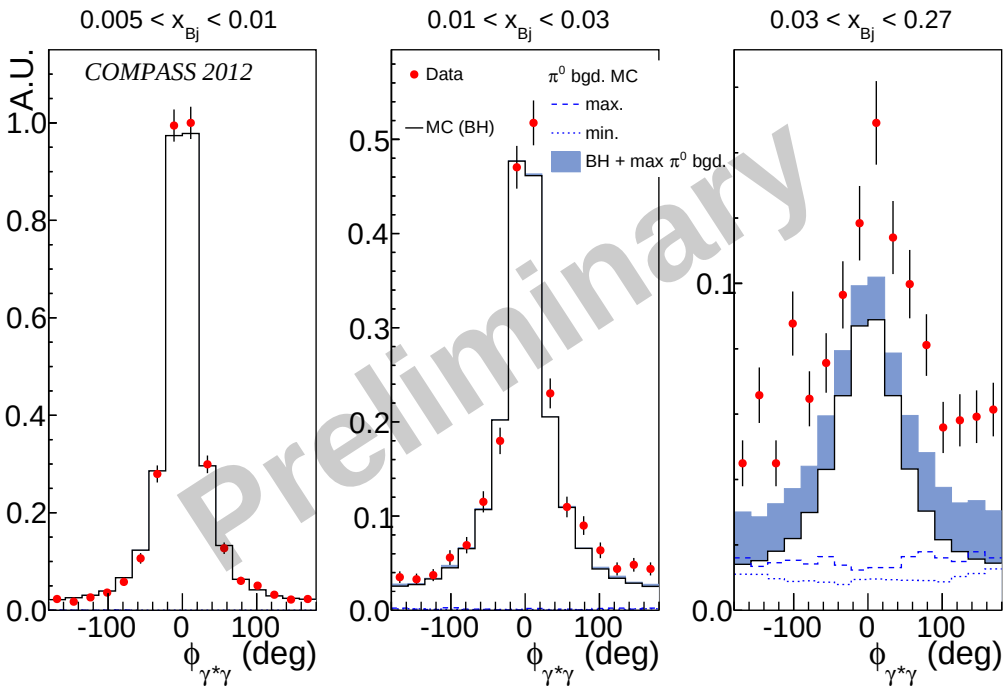

Fig. 28: The exclusive single photon events obtained in the 2012 sample as a function of $\phi_{\gamma*\gamma}$ compared to the BH estimation normalised to the data in the small x_{Bj} bin and to the π^0 contamination estimated either by LEPTO or by HEPGEN. The visible π^0 background has been subtracted from these data.

The set-up includes, as for the other COMPASS physics programs, a large acceptance tracking system, as well as muon filters, a RICH and calorimeters for muon identification.

The preparation for the 2014 DY run included the redesign, building and commissioning of the polarised target platform in its new location, 2.3 m upstream from the one used previously , as well as all related services. In the recovered space between target and spectrometer, the new hadron absorber was mounted together with a concrete shield structure. The full set-up is shown in Fig. 29 except for the two beam line CEDARs, which were used for beam particle tagging, and were set on kaons and antiprotons.

The two cells of NH_3 material that constitute the polarisable target are cylindrical with 2 cm radius and 55 cm length each. There is 20 cm space between cells, since the vertex resolution along the beam line is degraded by the presence of the hadron absorber. In the beam line there are two other non-polarisable targets: one aluminium cylinder 7 cm long is placed 27 cm upstream of the beam plug, inserted deep inside the hadron absorber. The tungsten beam plug itself acts as a target. Although its total length amounts to 120 cm, primary Drell–Yan interactions in tungsten come from the 20–40 cm most upstream part only.

6.2 Hardware upgrades for the Drell–Yan experiment

As it was already said above in order to make a successful Drell–Yan experiment at COMPASS a number of hardware upgrades has been performed. In more detail they are described in the "Hardware for Drell–Yan" Section of this document. Here we would like to bring only the list of upgrades, ordered according to the corresponding element position along the beam line, which looks as follows:

- upgraded CEDAR's system, main goal is to improve rate capability and thermal stability;
- Completely refurbished COMPASS Polarised Target Superconducting Magnet, new CERN-standard Magnet Control System (MCS) and Magnet Safety System (MSS);
- COMPASS Polarised Target with renewed cryogenic system and newly produced micro-wave cavity designed to host new 2-cells proton-free polarised target holder;

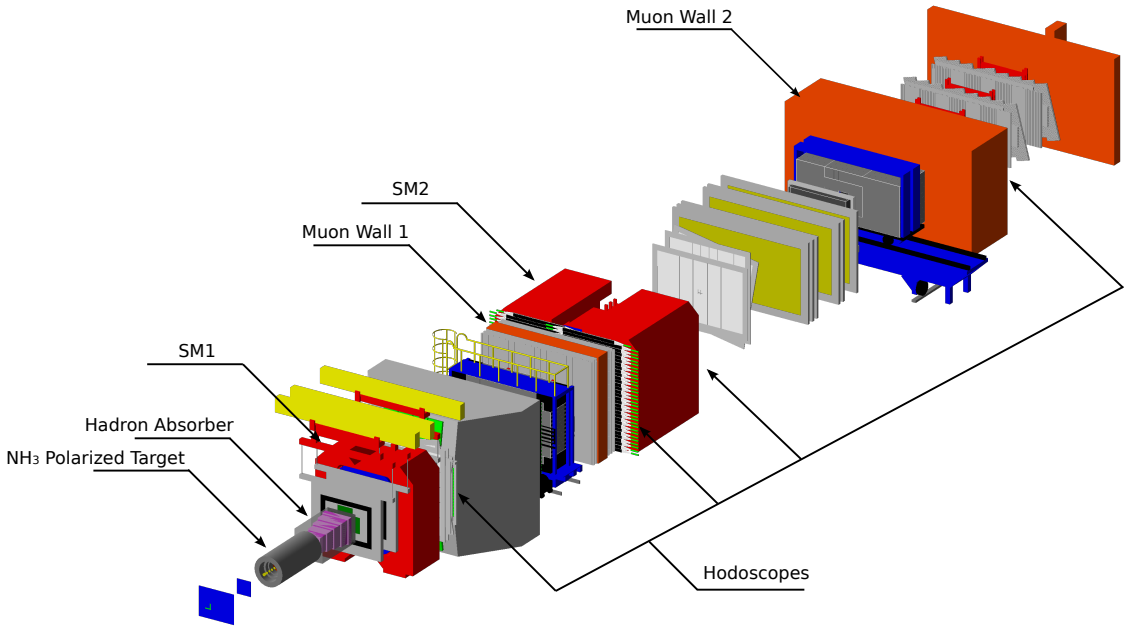

Fig. 29: Side view of the COMPASS DY set-up. Not visible in the figure are the beam telescope detectors, hidden by the Veto hodoscopes (in blue), and the CEDARs, upstream along the beam line. The vertex detector, located in the middle of the absorber, upstream the part represented in pink, is also not visible.

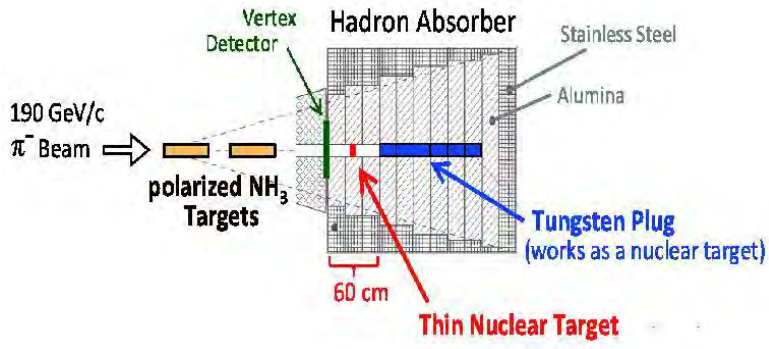

Fig. 30: The DY setup in the target and absorber regions.

– New scintillating fibre based high-rate-capable Vertex Detector placed in between the COMPASS PT and the Hadron Absorber (HA) with the goal to improve the dimuon event vertex resolution, degraded by the multiple scattering in HA;

– Hadron Absorber with the incorporated tungsten beam plug designed to stop a secondary hadrons flux over the spectrometer and to absorb non interacted in the PT hadron beam;

– DC05 Large Area Drift Chamber constructed to substitute the poorly performing Straw tube module #2;

– Completely new COMPASS DAQ system both hardware and software wise, designed to improve data taking stability and trigger rate capability.

6.3 Preliminary analysis of 2014 data

The 2014 DY data taking started on October 6 and lasted until December 15 2014, the period of beam availability. The first half of the running period was devoted to the commissioning of all parts of the new set-up,

to the beam tuning, and to the trigger related studies. The new DAQ system was also used for the first time in real data-taking conditions, and adjustments were made. Once the detector was found to be stable enough, we started the physics data-taking in view of the unpolarised Drell–Yan and J/ψ studies. The beam intensity was then increased, up to the nominal value of 10^8 pions/s. A preliminary analysis of these very recent data with high intensity beam revealed the good quality of the last 3 weeks of collection.

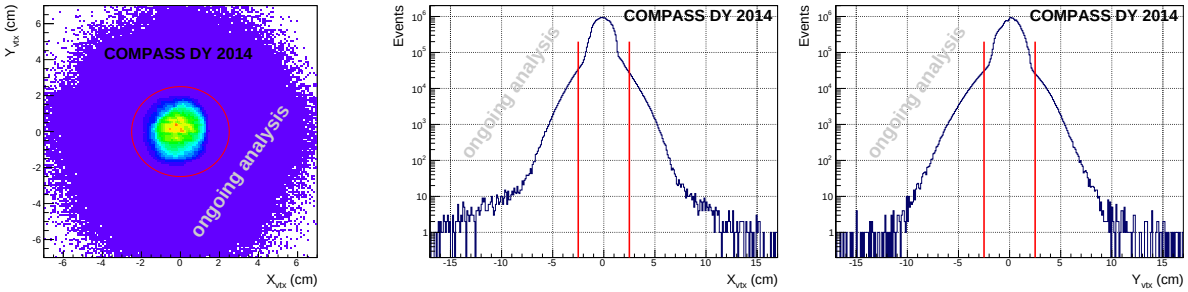

Fig. 31: Reconstructed primary vertices with 2 opposite charge muons and a beam, originated in the NH_3 target region. Transverse centring with the target cells and respective projections are shown.

In Figure 31 the good beam centring with the target cells is shown. Divergence was small, below 0.5 mrad, and the beam spot was kept large, with $\sigma_{x,y} \approx 1$ cm (which is of particular importance for the 2015 running with polarised target, in order to avoid local heating of the NH_3 material that could compromise the polarisation).

More than 80 million opposite sign muon pairs were analysed which associate to a primary vertex with beam track. The primary vertices of events with large dimuon masses are likely to be pure Drell–Yan events. For $M_{\mu\mu} > 4.5$ GeV/c^2 and below the Υ mass (where COMPASS has no longer relevant acceptance) this is the only physics contribution expected. Also the combinatorial background coming from uncorrelated muons from pion decays is not extending that far. Figure 32 shows the reconstructed primary vertices along the beam line, for the selected opposite sign muons with $M_{\mu\mu} > 4$ GeV/c^2. The 2 most upstream bumps visible correspond to the ammonia target cells, followed by the interactions in the plastic scintillating fibres of the vertex detector, the ones in the thin aluminium target, and finally those occurring in the tungsten beam plug. As the pion beam crosses the materials it is getting absorbed, by amounts consistent with the respective pion interaction length of each material.

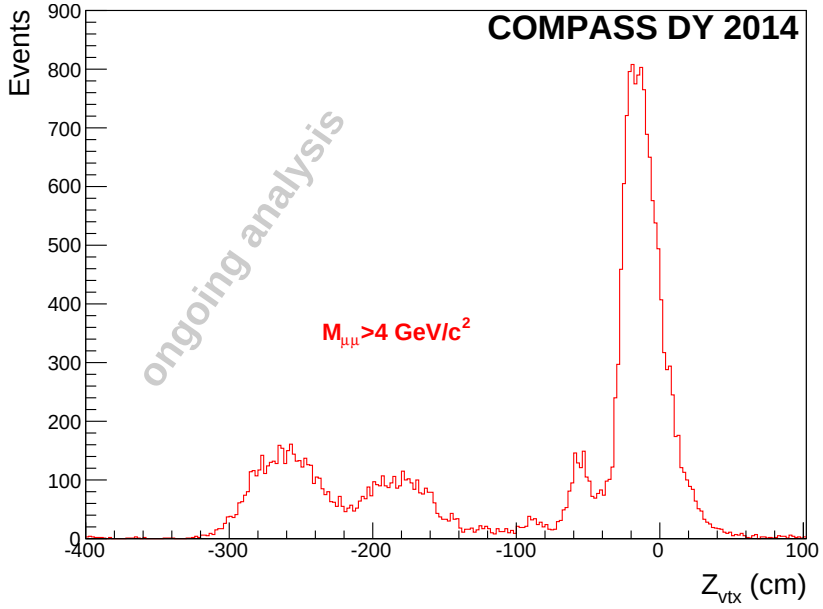

Fig. 32: Distribution of primary vertices along the beam line, for opposite sign dimuons with mass $M > 4.0$ GeV/c^2.

The dimuon invariant mass spectrum for the selected events originating from the ammonia target region is

shown in Fig. 33. About a quarter of a million J/ψs are present in this sample, as well as more than 5000 ψ' particles, from the NH_3 target only. The statistics shall be enough to extract interesting physics, starting with kinematical distributions of Drell–Yan and J/ψ events, and studies on the nuclear dependence of different processes.

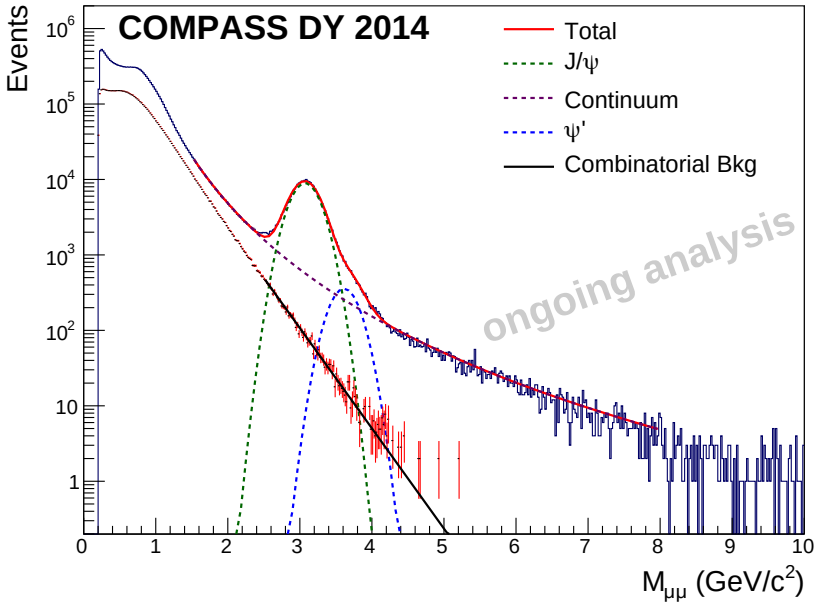

Fig. 33: Dimuon invariant mass spectrum, for primary vertices in the ammonia target region.

The continuum under the J/ψ is a sum of different physics contributions, namely Drell–Yan and a small amount of semi-leptonic open charm decays; and the combinatorial background already referred above, which can be studied using the like-sign dimuons collected. From the like-sign samples one can, after some symmetrisation on charges acceptance, obtain the distribution for the combinatorial of uncorrelated opposite-sign muon pairs. This distribution is shown in red in Fig. 33, being negligible for masses $M > 4.5$ GeV$/c^2$.

Very preliminary kinematical distributions of the opposite sign dimuons with $M > 4$ GeV$/c^2$ are shown in Fig. 34. The dimuon p_T distribution peaks at 1 GeV$/c$ as expected for Drell–Yan. Events with very high p_T suggest selection cuts still need some tuning. The x_p versus x_π plot shows that the phase-space accessed is indeed the proton and pion valence quarks one, where COMPASS proposes to access the TMD PDFs, and namely the Sivers one [40]. The Feynman-x distribution is typical of fixed target experiments, showing small access to the region of exclusive Drell–Yan, as was expected. These distributions are all for events originated from the ammonia target region only. The distributions obtained from other targets, namely tungsten, where we have large statistics, shall be affected by larger smearing, due to significant multiple scattering in the target material itself, added to the one in hadron absorber.

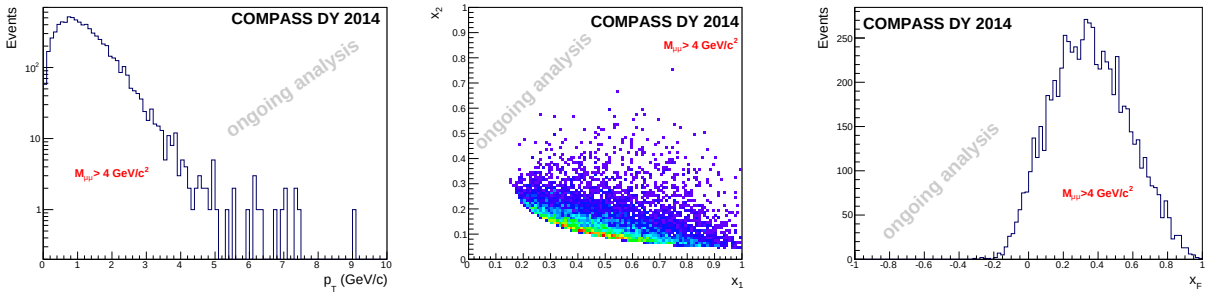

Fig. 34: Kinematical distributions for primary vertices with 2 opposite charge muons and a beam, originated in the NH_3 target region and with dimuon mass $M_{\mu\mu} > 4$ GeV$/c^2$. Dimuon transverse momentum (left), x_p versus x_π (centre) and $x_F = x_\pi - x_p$ (right).

The plots presented here do not include yet vertex detector information. Due to the difficult location of this

detector, its inclusion in the reconstruction requires special code, which is being tuned at the moment. The relatively high occupancy and the fact that the tracks have to bridge over the hadron absorber, coping with the multiple scattering involved, makes it a difficult task. These will be the coming steps in this analysis, expected to improve the resolution in what concerns the ammonia target cells separation.

6.4 2015 polarised Drell–Yan Run

The polarised Drell–Yan experiment in COMPASS was approved in 2010, and is the program for the full 2015 COMPASS data-taking. This will be the first measurement of this kind in the world. It will provide an insight into the TMD PDFs of the nucleon, complementary to that already given by SIDIS measurements also done at COMPASS [41].

The 2015 Drell–Yan data taking started on April 27 and is expected to last until November 15 2015. The three major differences with respect to 2014 are the ammonia target which is now transversely polarised; an additional absorber foil added to the hadron absorber that stops spallation neutrons; and the new large area drift chamber which is now included in the set-up. Another improvement concerns the reduction of dead time thanks to the optimisation of veto anti-signals included in the physics dimuon triggers. The Run is progressing as expected, up to now. One month of data-taking passed, the hadron beam has been tuned and beam telescope detectors placed according to the beam optics that compensate the Lorentz force of the target dipole deviating the beam in x-direction. A beam optics is chosen such that the beam enters the experimental hall with an angle $\theta_x = 1.6$ mrad, and an offset such that it crosses the two target cells optimally centred.

6.5 2015 - expected statistics

Based on the analysis of 2014 data, and assuming certain run conditions for 2015, one can make an estimate of the expected event rates and yields. Uncertainties are still large, namely concerning the supercycle lengths during the Run (here assumed to be according the official schedule), the COMPASS DAQ dead-time at nominal beam intensity (only preliminary tests were done, but here a live-time value of 0.7 is assumed), and the COMPASS strategy for repolarisation (here assumed to be every 2 weeks, coincident with Machine Development).

A Drell–Yan event rate of 800/day is expected from the ammonia target region. Since the ammonia itself is immersed in a bath of helium, with packing factor estimated around 0.5, this number of DY events corresponds to both NH_3 and He. In 140 days of physics data-taking this would mean 96000 DY events with $M > 4$ GeV$/c^2$. This value deviates less than 20% from estimates given in the COMPASSII proposal (mostly because of the spectrometer availability, or live-time).

A dedicated analysis of 2014 data on the nuclear targets was not yet done. Based on the proportions of high mass dimuon events found in Fig. 32 one can set a rough lower limit of 100 DY events/day from aluminium target, and 1000/day from tungsten target.

7 Hardware

7.1 Hardware for the 2015 Drell–Yan

7.1.1 CEDAR upgrade

The CEDARs will be used to tag K and $\overline{p}$ (about 2.5% and 0.5% of the particles in the M2 190 GeV/c hadron beam at COMPASS).

In the 2014 pilot run the following activities have been performed. In order to improve the uniformity of the temperature field in the CEDAR vessels a new insulating tent was built, equipped with fan units for the air circulation and with 8 PT100 distributed on each CEDAR cage (see Fig. 35).

Temperature uniformity within 0.4 °C is now achieved on the CEDAR cages and temperature gradients within 0.2–0.3 °C are now measured on the (old) inner PT100 (the latter was 1.5 °C on CEDAR1). New GANDALF modules with 1 Gs/s waveform digitisers and with built-in CFD algorithm (Freiburg design) have been installed; they provide both amplitude and time information on the CEDAR PMT signals. The beam-line has been tuned

Fig. 35: CEDAR tent structure constructed in 2014.

in collaboration with CERN in order to have an as parallel a possible beam; RMS divergences from TURTLE-TRANSPORT beam software are: $X = 177$ μrad, $Y = 109$ μrad. The equalisation of the 16 PMTs was performed (CERN) obtaining efficiencies in the range 0.8–0.88. The pressure scan has been performed with Light Diaphragm (LD) of 0.4 mm and with beam intensity of 1.2×10^7 p/spill. It showed a reasonable separation between π and K-meson peaks but with a K detection efficiency of about 0.25, lower than in the past. The result of the pressure scan is presented in Fig. 36.

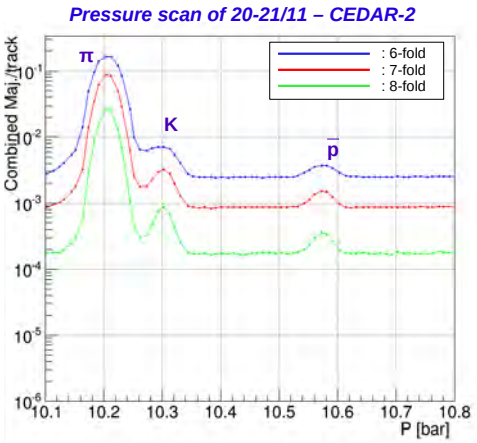

Fig. 36: Results of the pressure scan of the CEDAR-2 detector obtained in Nov. 2014.

PMT time resolutions obtained by comparing the PMTs of the same CEDAR were of 1.8 ns from the old TDC chain and 1.6 ns from the new GANDALF chain. They are consistent with the TTS of the PMTs and compatible with the high beam intensity planned to be used in 2015. There are basically three remaining open problems after the pilot run of 2014: some instability of the CERN electronics chain (likely due to the programmable delay lines), problems in the timing of the COMPASS DAQ chains for the CEDARs (both TDCs and GANDALFs) and relatively low K detection efficiency (likely due to the PMT efficiencies).

In 2015 the tuning of the complex PMT voltage dividers have been revised, removing some residual ringing and optimising the gain. Two PMTs have been replaced (CERN). The CERN electronics chain was reviewed to repair instabilities. A first PMT equalisation and CEDAR preliminary alignment have been performed, but the PMT efficiencies are still rather low (0.84 on CEDAR-1 and 0.87 on CEDAR-2). After a pressure scan performed with LD = 0.4 mm and intensity of 4.5×10^7 p/spill the separation between π and K peaks resulted worse than in 2014. Additional work to increase PMT efficiency (to reach the design figure of ¿ 90%) and to test the effects of beam intensity on the CERN electronic chain is in progress.

7.1.2 Polarised target magnet

All the services for the repaired magnet, including Magnet Safety System (MSS) and Magnet Control System (MCS), were installed in the COMPASS experimental area (Bat. 888) during the summer 2014 (see the picture of the MSS and MCS in Fig. 37).

Fig. 37: Picture of the COMPASS polarised target control system installed in Bat. 888 (COMPASS experimental area).

The stage of cooling started in September but lasted longer than expected due to insufficient availability of helium and the cold box during several weeks to cool it to 4 K. Once fixed, electrical tests were performed and magnet protection was checked in November with PH-DT. Solenoid and dipole have been tested successfully at their nominal current in the beginning of December 2014 in both polarities. A first field homogeneity could be obtained using the NMR peak signal from the coils located along the target.

The helium delivery was stopped during the CERN closure in December, then the magnet was naturally warmed up and reached room temperature on 22nd January. The cooling was restarted mid of February 2015 in better conditions than in 2014 and took about 2 weeks. The preparation and commissioning of the magnet was resumed in March with the participation of PH-DT. One of the most important steps to do was to set-up the operational procedures to combine solenoid and dipole fields in order to allow the magnetic field rotation without losing the polarisation of the target. Scripts to be run by the control system were developed, implemented and intensively tested during several weeks, and then endorsed. In Figure 38 one can see the snapshot of the COMPASS PT magnet power interface screen while performing test field rotation.

Reactions of the Magnet Safety System (MSS) were carefully studied during these tests and validated. This program was interrupted 3 weeks in April during the absence of the engineer from PH-DT in charge of programming the control system and then could only be terminated when the beam was already delivered to COMPASS. The first TE calibration of the NMR signal was performed manually in May. It normally requires communication between the NMR control and the magnet control system but it was not yet ready at that time. A very slow discharge at nominal current in the solenoid has been experienced. In such situation the energy stored (3 MJ)

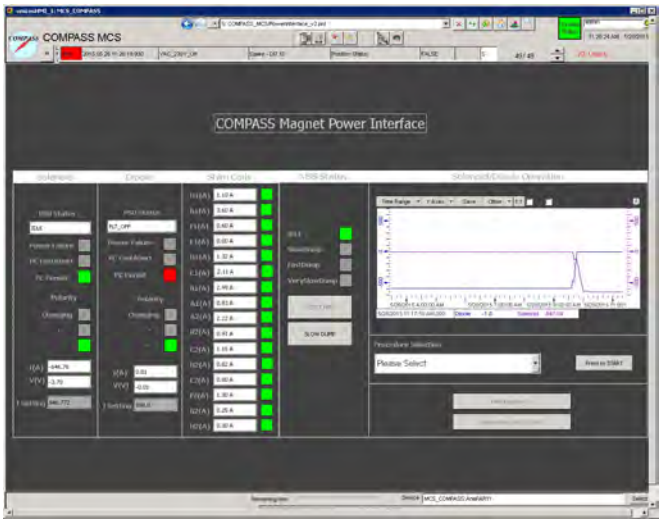

Fig. 38: Snapshot of the COMPASS magnet power interface screen during the test field rotation.

in the coil is dissipated slowly in the power cables. We observed that during more than 4 hours the value of the solenoid field stays higher than 0.5 T, keeping the polarisation in safe condition and giving sufficient delay to ramp the dipole field. Another important validation concerns the fast discharge of the solenoid at nominal current that occurred during an incorrect manual operation. It developed for the first time at this level of current since the magnet has been repaired. The magnet was checked afterwards and was found healthy.

7.1.3 Polarised target

The COMPASS spectrometer is using solid state polarisable ammonia target in the transverse Drell–Yan physics data taking. The superconducting magnet together with horizontal dilution cryostat, microwave cavity and corresponding services had to be moved by 2.3 meters upstream from the last SIDIS measurements in the run 2011 due to the place taken by the new hadron absorber. The target platform had to be moved first before the superconducting magnet could be placed to the new position. The photo of the COMPASS set-up in the polarised target region is shown in Fig. 39.

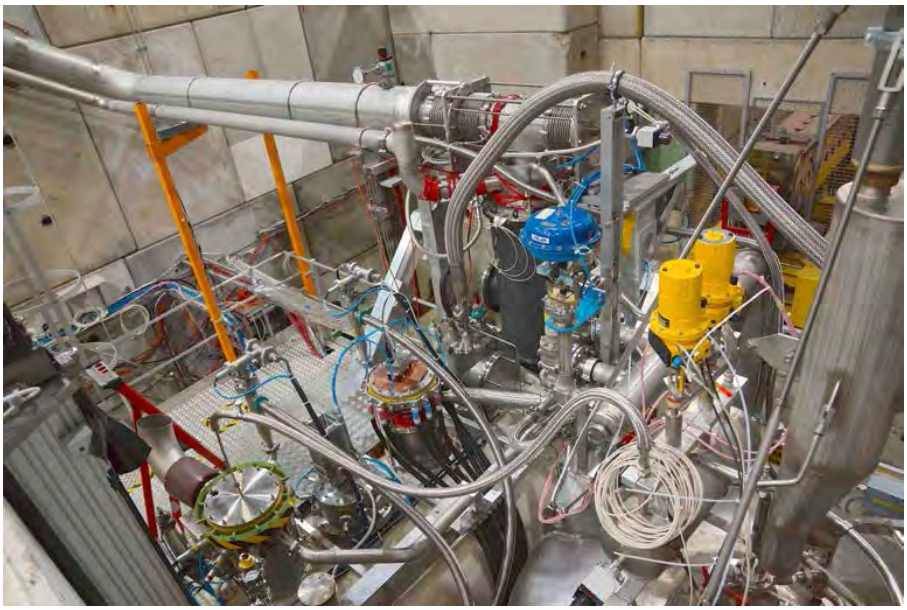

Fig. 39: Picture of the COMPASS DY setup in the region of the polarised target.

The microwave cavity was modified for two oppositely polarised target cells with a new internal microwave stopper.

The target material has to stay below 100 K during the loading into the mixing chamber of the dilution cryostat. The target cells are filled with solid ammonia on a separate loading platform that had to be adapted to the smaller limited space. New target cells were produced from plastic without hydrogen bonds. This should eliminate the need of measurement of proton background NMR signal that comes from aramide epoxy composite used in the previous design. The two cells are 55 cm long, have diameter of 4 cm and they are separated by 20 cm gap. Each target cell has two internal NMR coils and three coils mounted on the cells for the polarisation measurement.

Thanks to new microwave guide lines, which makes microwave power feed into the target efficiently, about 80 % polarisation was obtained during less than 2 days in the first complete polarisation test (May 18). The relaxation time of the proton at 0.6 T with a high intensity hadron beam of 8×10^7/s was also measured to be 1300 hours. However it was still long enough for the data taking, it is slightly faster than the value in 2010 and 2007 because of warmer temperature and the dilution cryostat will be optimised.

The polarisation level of the PT material is shown in Fig. 40 for up (left plot) and $down$ (right plot) cells independently.

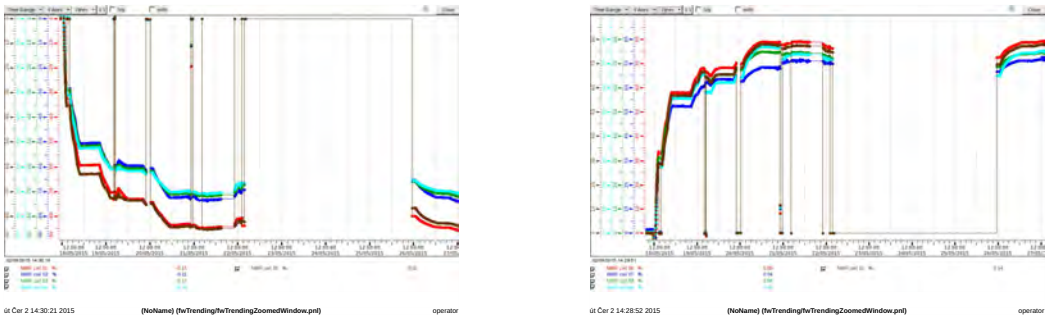

Fig. 40: Polarisation built-up as a function of time is shown separately for both target cells. The up is shown in the left plot and $down$ - in the right one.

There were many interruptions during the polarisation operations, for example magnet tests and switching microwave on and off. Basically the polarisation reached the maximum level after less than two days of polarisation.

7.1.4 Scintillating fibre based vertex detector

The hadron absorber, necessary to suppress the hadronic background and to filter the remaining primary beam in order to have a clean $\mu^+\mu^-$ sample, increases the distance from target to the first set of tracking detectors by about 2.3 m. Moreover, the material of this absorber significantly degrades both, the resolution of the reconstructed primary vertex and the reconstructed invariant mass of the dimuon pair because of the multiple scattering. Compared to the COMPASSset-up without absorber the mass resolution degrades from ≈ 85 MeV/c^2 (σ) to ≈ 200 MeV/c^2 (σ). Especially, the vertex resolution along the beam axis is strongly compromised from 0.8 cm (σ) to 6.5 cm (σ), making a clean separation of both target cells mounted at a distance of 20 cm difficult. From Monte Carlo simulations it was seen that a vertex detector with an approximate size of 15×15 cm^2 mounted at a distance of about 50 cm from the target could improve the situation significantly. For the detector design the high particle rate at this position has to be considered. The simulations showed that for each primary particle 7.5 charged particles will pass the detector. For an initial flux of 10^8 pions per second, the expected average rate is about 3 MHz/cm^2. Given this high rate, a design based on scintillating fibres was chosen, as scintillating fibre detectors, in use since the beginning of the COMPASSexperiment, have been proven to combine high rate capabilities with excellent timing resolution. They are in use where the primary beam has to be detected or where it is not yet completely separated from scattered particles. The chosen design is:

– Three detector planes(X,U,V)

- U,V planes: ($\pm 45°$): 15×15 cm^2
- X plane : 22.5×22.5 cm^2, covering completely the U and V planes
- Scintillating fibres: round Kuraray SCSF 78 MJ 1 mm diameter
- Pitch: 0.7 mm
- Deactivated centre with about 3 cm diameter
- Number of channels: 912
- Dimension along beam axis (including housing): ¡ 6 cm

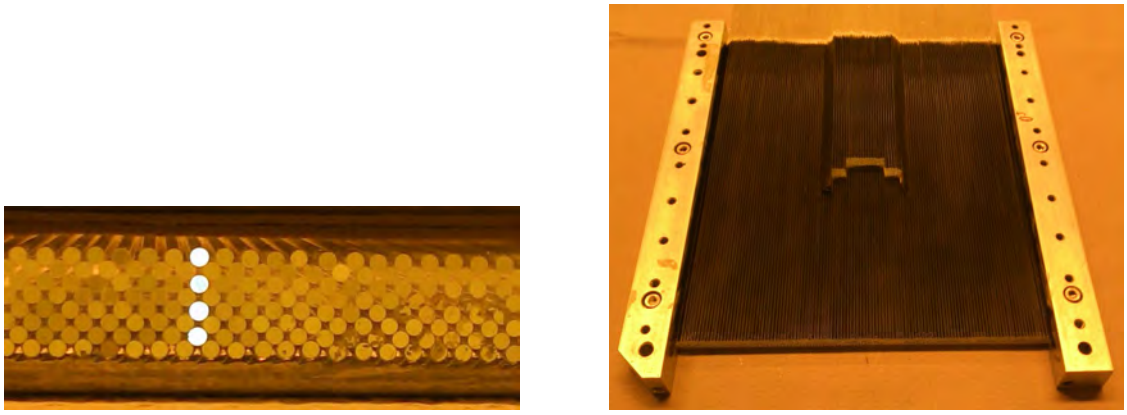

Fig. 41: Left: Front view of a detector plane. One detector channel comprises a stack of 4 fibres; Right: Top view of the U layer covered by protective paint.

The use of 1 mm diameter fibres results in rates of 4–6 MHz per fibre in the outer and about 12 MHz in the central region, not taking the deactivated area into account. The high rates in the central region could result in problems with the data readout as well as with resolving ambiguities in vertex reconstruction. As the muons emitted under small scattering angles have to pass the central plug of the absorber the error of the reconstructed angles is quite large and they will not be used in the analysis. Therefore, it was decided to deactivate a 3 cm diameter central region of the vertex detector by introducing light guides instead of scintillating fibres. This limits the maximum rate to about 7–8 MHz.

The simulations showed that this vertex detector will improve the mass resolution slightly to ≈ 175 MeV/c^2 (σ). However, the primary vertex resolution along the beam axis will be improved to ≈ 4.5 cm (σ), making a separation of both target cells on a $\geq 4\sigma$ level possible.

The readout comprises a new 16-channel multianode PMT (Hamamatsu R11265-100-M16) which has been tested to deliver clean signals up to rates of 16 MHz per channel and 16-channel FPGA based discriminator boards developed at GSI Darmstadt (PaDiWa). The TDCs used are the 128-channel FPGA based Gandalf modules developed for COMPASS by the University of Freiburg.

The construction of the detector started in mid 2013 and was finished by July 2014. The detector was then shipped to CERN and installed in August 2014 (Fig. 42).
Figure 41 left shows the design of a single plane. One detector channel comprises of a stack of 4 fibres as can be seen by one illuminated channel. The right picture shows the top view of the U-plane. The thicker part on the top centre comprises the fibres dedicated to the readout above the deactivated centre. Figure 42 left shows all three detector planes mounted in the final housing. The pictures to the right show the mounted detector close

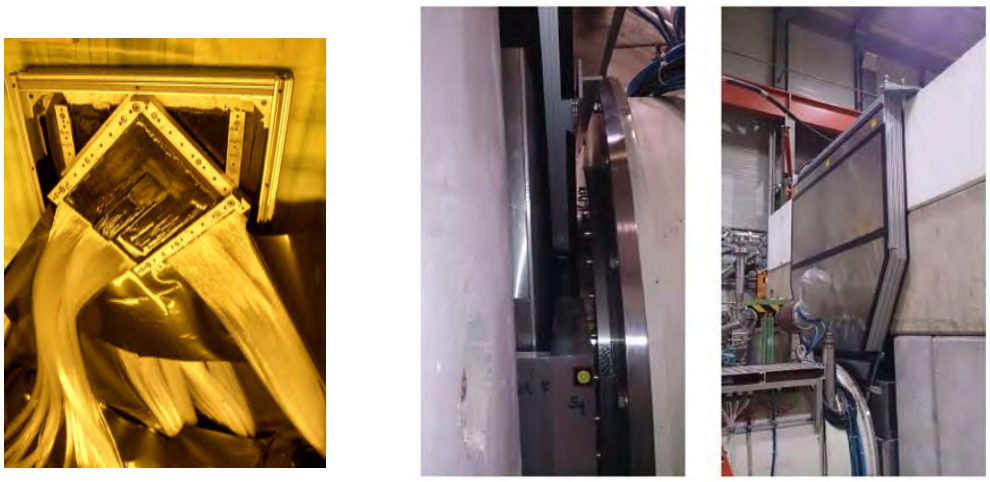

Fig. 42: Detailed views of the detector: scintillator planes mounted in the detector frame (left), central part of the detector fit into the absorber (centre), full view of the detector (right).

to the COMPASS target in frontal view (right) and in a detailed view of the dedicated 6 cm slot reserved for the detector.

During the Drell–Yan test run October-December 2014 the detector was commissioned. Special care was taken to achieve an excellent time resolution. This is necessary in order to efficiently separate hits belonging to different events, given the high initial flux of 10^8 pions per second and peak rates of close to 10 MHz per fibre. Figure 43 shows the time resolution achieved with the detector. Each plot shows the time difference in TDC channels of 160 ps of two coincident fibre hits in the X-U (top) X-V (centre) and U-V planes (bottom), respectively. The typical width of the timing peaks seen for the whole detector is < 6 TDC channels. This corresponds to a time resolution of < 680 ps (σ) well suited to separate hits from different events.

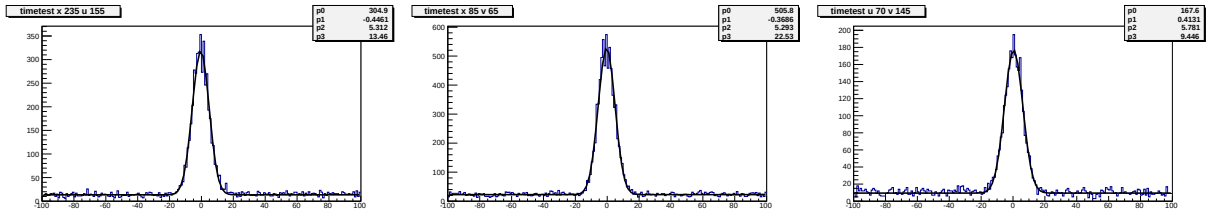

Fig. 43: Time resolution of the vertex detector. Plotted is the time difference of two coincident fibre hits ($t_1 - t_2$) for the X-U (top) X-V (centre) and U-V planes (bottom). The time unit is in TDC channels of 160 ps.

7.1.5 New hadron absorber: installation and performance

As said before, the installation of an hadron absorber downstream of the target allows to reduce the high secondary particle flux produced by the interaction of the pion beam in the target and, consequently, the detector occupancies. This makes an increase in the intensity of the incident pion beam possible. The absorber, 236 cm long, is made by alumina (Al_2O_3), with a 140 cm long tungsten beam plug inside it to stop the non-interacted beam. The alumina absorber stops the secondary particles flux, minimising multiple scattering; this is essential to disentangle the two oppositely polarised target cells in the track reconstruction. A concrete shielding surrounds the whole structure to reduce the dose rate, well below the 15 μrad/hour.
The installation has taken placed in the first week of July 2014. Two images of the hadron absorber in place in the COMPASS hall are shown in Fig. 44, before (left) and after (right) the installation of the concrete shielding.

To allows the installation of the absorber and the concrete shielding around, the polarised target, the solenoid and its supporting platform, have been moved 2.3 m upstream. In Figure 45 a 3D design of the platform, the superconducting solenoid, the concrete blocks and the absorber are shown. The side and top concrete blocks

Fig. 44: The fully assembled hadron absorber in the COMPASS hall: (left) before and (right) after the installation of the concrete shielding and Vertex Detector.

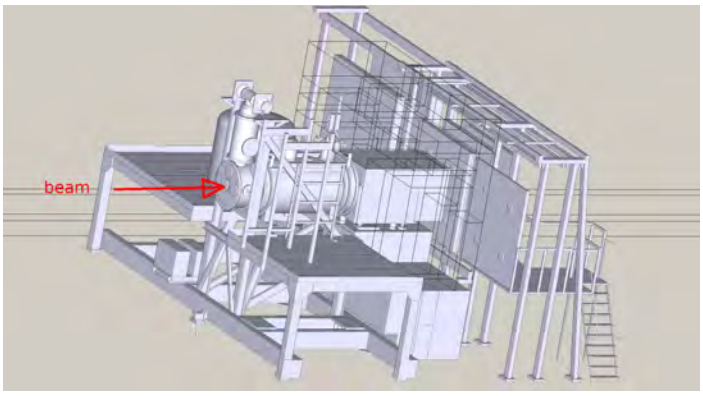

Fig. 45: 3D design of the target region configuration for the Drell–Yan measurements:the superconducting solenoid and its supporting platform, the concrete blocks and the absorber are shown. Downstream the absorber, the existing suspension structure of the Micromegas and DC detectors is also shown.

are shown with the contour lines only.

During the 2014 hadron run up to the nominal value of the beam intensity of 10^8 π/sec, the hadron absorber fulfilled the expected performances, which were studied with Monte Carlo simulations performed both with FLUKA and GEANT4. The occupancies on the tracking detectors most exposed to secondary beam flux (Micromegas, Pixel Micromegas, DC00, DC01, DC04 and Straws) were consistent with simulation results and did not exceed the maximum allowed values.

7.1.6 New pixelised hybrid Micromegas detectors

Twelve large gaseous Micromegas detectors with active area of 40 $\times$ 40 cm^2 were used on the COMPASS experiment, measuring particle position on 4 coordinates X, Y, U and V (see Fig. 46).

They are placed right downstream of the polarised target in order to measure particles scattered at small angle. The beam area of every detector (5 cm diameter at the centre of the detector) being however blinded as the particle flux was too high there. The hit rate seen by the detectors can be above 100 kHz/strip in the area close to the beam.

A new project lead by IRFU institute of CEA Saclay began in 2009 in order to replace these detectors by new ones, with two main goals in mind: to activate the centre of the detectors, where the beam is going through, and to decrease the impact of discharges which appear in the amplification stage with high intensity hadron beams which we were aiming to have during the Drell–Yan data taking.

A long phase of R&D on discharge impact reduction lead to the idea of hybrid Micromegas detectors, where an

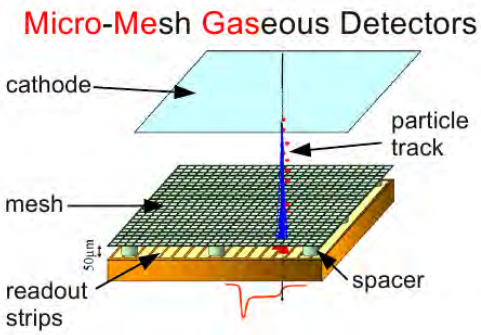

Fig. 46: Micromegas detector principle. The ionisation electrons coming from the incoming particle are amplified in the gap between strips and micro-mesh and read on the strips.

additional amplifying GEM foil is added above the micro-mesh in order to decrease the gain of the Micromegas stage, and thus to reduce the probability of discharge. A concurrent solution using resistive layer structure (buried resistors) deposited on top of the read-out anodes was studied, but the performance of that solution were not as good as the hybrid solution, in particular concerning the time resolution.

The new detectors are read by 400 μm-pitch strips on the central part (40% of the surface) and 480 μm pitch strips on the sides, which cover the 40 $\times$ 40 cm^2 active area. The centre of the detectors, blind on the old ones, were equipped with a pixelised read-out (Fig. 47) with rectangular pixels which keep the same 400 μm pitch and thus the same spatial resolution as the strips.

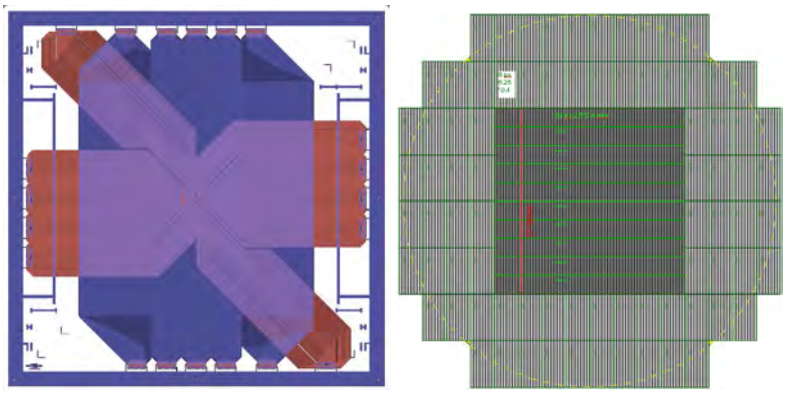

Fig. 47: Scheme of the pixel area (right) and position in the detector (left). Rectangular pixels have the same 400 μm pitch as the strips.

Full size hybrid prototypes were built and tested in nominal conditions in the Compass spectrometer in 2011–2012. They are equipped with read-out electronics based on highly integrated APV chips, which are also used on other COMPASS detectors like Silicon, GEMs and RICH MWPCs. The detectors shown very good performance, with particle detection efficiencies above 96% with high intensity muon and hadron beams, spatial resolutions below 70 μm and time resolution around 9 ns (see Fig. 48 and Fig. 49).

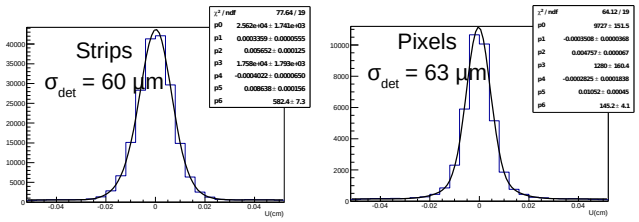

Fig. 48: Spatial resolution of a new hybrid pixelised Micromegas detector, measured in high flux muon beam. Strips (left) and pixel resolutions (right) are in the order of 60 μm

Discharge rate stays very low, with a probability by incoming hadron reduced by a factor larger than 100 compared to old Micromegas detectors. New Micromegas detectors were partially installed in 2014, where

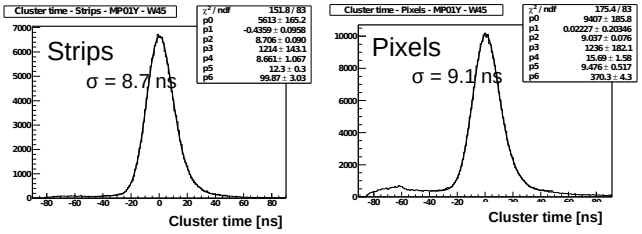

Fig. 49: Time resolution of a new Micromegas detector, measured with high flux muon beam. Strip (left) and pixel time resolution (right) are in the order of 9 ns.

they replaced obsolete detectors of the station 1 (4 new detectors installed). The remaining eight detectors were installed for the beginning of the 2015 run (see Fig. 50).

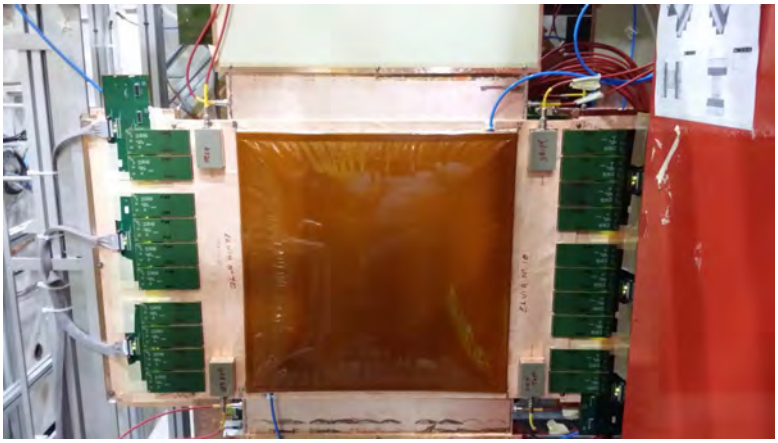

Fig. 50: Final Micromegas set-up with the newly installed PMM.

7.1.7 *Large area drift chamber (DC05)*

A new planar drift chamber, DC5, was built in 2014 to replace the ageing straw detector station 2 in the COMPASS Large-Angle Spectrometer (LAS). DC5 follows closely the design of drift chamber DC4 that has been developed for application in COMPASS in the past by CEA-Saclay and was made available to the University of Illinois for the construction of DC5. DC5 has an active area of about 5 m^2 and consists of 8 views (YY′XX′VV′UU′) with a total of 2304 readout channels, with each 256 (320) channels in the YY′XX′ (VV′UU′) views. The chamber has a pitch of 8 mm between sense wires and the resulting small maximum drift distance of 4 mm allows to operate the chamber at the expected high background rates of up to 150 kHz per wire. New front end electronics based on the CMAD chip from INFN Torino was funded, developed and produced by the new COMPASS collaborators from Academia Sinica in Taipei. The detector was funded by NSF and the new COMPASS institution UIUC and constructed at the Nuclear Physics Laboratory of the University of Illinois in Urbana Champaign. Four of the anode planes were wired at Old Dominion University in Norfolk, Virginia. Cathode coating and final assembly of DC5 were carried out at CERN. DC5 was installed in COMPASS on May 13th (see Fig. 51).

First tests indicate that the FEE operate well meeting expectations concerning stability and noise. Promising amplification signals with DC5 filled with its nominal gas mixture (Ar/Ethane/CF_4 = $45\%/45\%/10\%$) have been measured with a ^{90} Sr source (example in Fig. 52).

7.1.8 *New* COMPASS *DAQ system*

After more than 10 years of successful operation the COMPASS DAQ system required a serious upgrade. A multiport PCI technology, a back bone of the system, became obsolete. The DATE software required a significant changes to migrate to 64 bit SLC6 operating system. Mean while the ALICE DAQ group has developed a new DAQ software and announced a maintenance termination of the current system.
Taking into account all these factors the COMPASS DAQ group has developed a completely new DAQ system

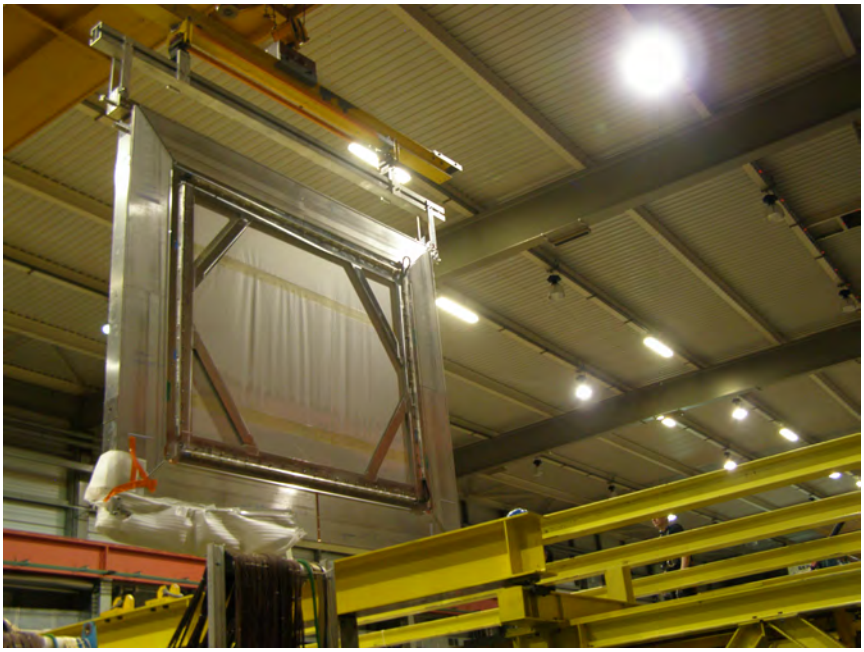

Fig. 51: DC05 installation in the COMPASS experimental area.

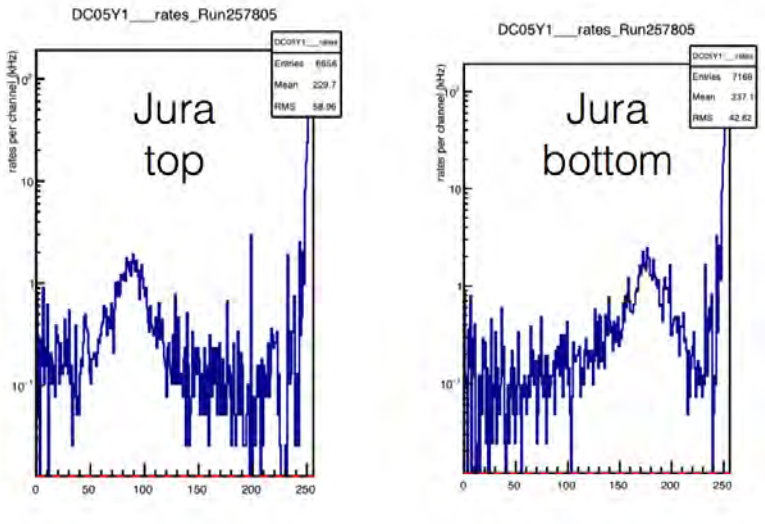

Fig. 52: Signal profile induced in DC05 by ^{90} Sr source as it is seen in the COMPASS on-line program COOOL.

using a State-of-the-Art hardware as well as modern software technology.
The system architecture is shown in Fig.53. It consists of hardware event builder, implemented in nine FPGA based Data Handling Modules, spill buffer PCIE cards and Readout Engine computers. Configuration, control and data handling inside computers are done by the COMPASS DAQ software.

One module is shown in Fig.54 together with a complete event builder for 2015 year run. The design of the module is optimised for DAQ applications with multiple high speed serial links, big memory for data buffering and real time data processing.
The Data Handling Module employs Xilinx FPGA XC6VLX130T chip and features 16 high speed serial links(SLinks) and 4 Gbytes of DDR3 memory. The DHM can be programmed as COMPASS MultipleXor(CMX) or COMPASS SWitch(CSW) module.

The event building is performed in two stages. At the first stage each CMX module reads data from up to 15 front-end modules, stores the information in the attached 4 GBytes memory and then sends combined data to

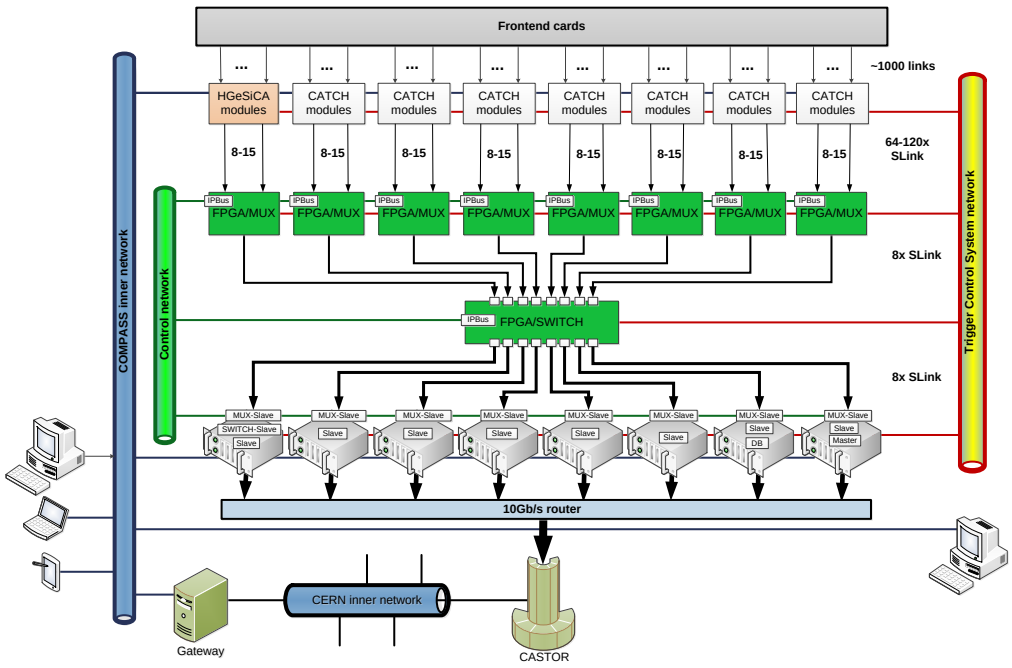

Fig. 53: A new DAQ architecture.

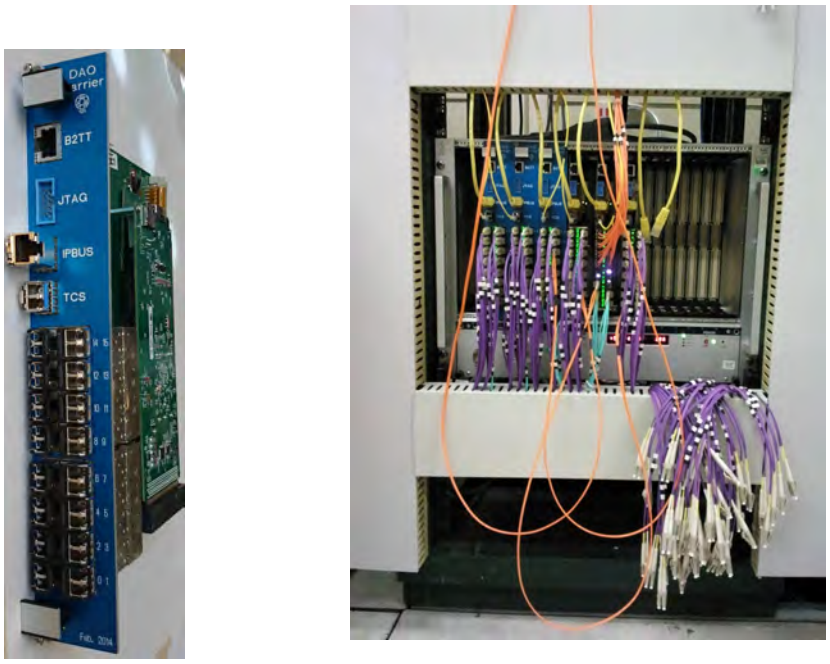

Fig. 54: Photos of DHM module (left) and Hardware Event Builder (right) for 2014 and 2015 data taking period.

the CSW module via single serial link. The CMX module can be seen as a 15 to 1 multiplexer. At the second stage the CSW combines partially assembled events from 8 CMX modules in complete events and then distributes them between 8 Readout Engine on-line computers using PCIE Spill Buffer cards as an interface. The DAQ software stores data in local hard disks and then copies data to CERN's Central Data Recording facility.
A maximum sustained system bandwidth is 1.0 GBytes/s while a maximum peak rate, which can be handled by the system within the spill, is 20 GB/s.
One of important feature of the system that it checks data consistency at all stages of data transmission and event assembly, which makes the system, first of all, more robust and more reliable, and secondly, simplifies

identification of malfunctioning hardware or front-end electronics. The software part of the DAQ provides intuitive and transparent Graphical User Interface for system configuration and monitoring. The run control GUI and interactive DAQ status window are shown in Fig.55 and Fig.56 accordingly.

Fig. 55: The Run Control GUI displays status of the DAQ, trigger rates, prescaling values and event sizes ver

Fig. 56: The Interactive status and configuration GUI shows status of all attached front-end modules, DAQ modules and Readout Engine computers.

The DAQ system has been commissioned in 2014 for the first Drell–Yan pilot run. Although, the system performed well and showed similar performance to the previous DAQ, it was not able to handle correctly certain errors of data format occurred in the front-ends which lead to DAQ crashes. During winter shutdown errors in FPGA firmware and DAQ software have been identified and fixed. The hardware event builder for 2015 run consists of 5 CMX modules and one CSW module and can be seen in Fig54. The DAQ has been tested up to 40 kHz trigger rate and 800 MByte/s data rate within the spill. The DAQ could handle even higher trigger rate but it's limited by the front-end electronics performance. During normal data taking it's expected to run with about 30 kHz trigger rate.

7.2 Completing the DVCS and SIDIS setup

The CAMERA detector is a barrel-shaped device that surrounds the 2.5 m long liquid Hydrogen target for the COMPASS DVCS measurements. It consists of two concentric cylinders of plastic scintillating detectors, azimuthally segmented into 24 slabs. The length of the scintillating elements is 2.75 m and 3.60 m for the inner and outer cylinders respectively, and the radial distance between the two cylinders is of 85 cm. The charged particles, recoiling at large angles from the target, are detected by measuring the hit position in each cylinder and the Time-of-Flight (ToF) between the inner and the outer barrels.

The detection of the recoil protons is essential in order to cleanly separate the rare exclusive DVCS events ($\mu p \to \mu \gamma p$) from the leading semi-inclusive DIS reactions. The exclusive reactions are selected in the off-line data analysis by imposing tight cuts on the four-momentum balance of the reconstructed events. Therefore, an excellent ToF resolution is mandatory in order to maximise the background rejection. Nevertheless, the inner scintillating counters have to be thin (4 mm) in order to allow for slow protons with momentum as low as 260 MeV/c to reach the outer barrel. This limits the reachable time resolution to about 300 ps.

7.2.1 Upgrade of the CAMERA recoil proton detector

The inner scintillating counters currently installed in the device are characterised by a non-optimal light transmission. The light attenuation lengths (λ), measured prior to their installation in summer 2012, ranged from 0.7 m to 1.2 m, leading to degraded performances during the 2012 pilot DVCS data taking. In Figure 57 we show the correlation between the measured attenuation lengths and time resolutions for the present scintillating counters. This graph clearly shows that an attenuation length better than 1.5 m is needed in order to reach the design time resolution of about 300 ps. The degraded light transmission also has a measurable impact on the

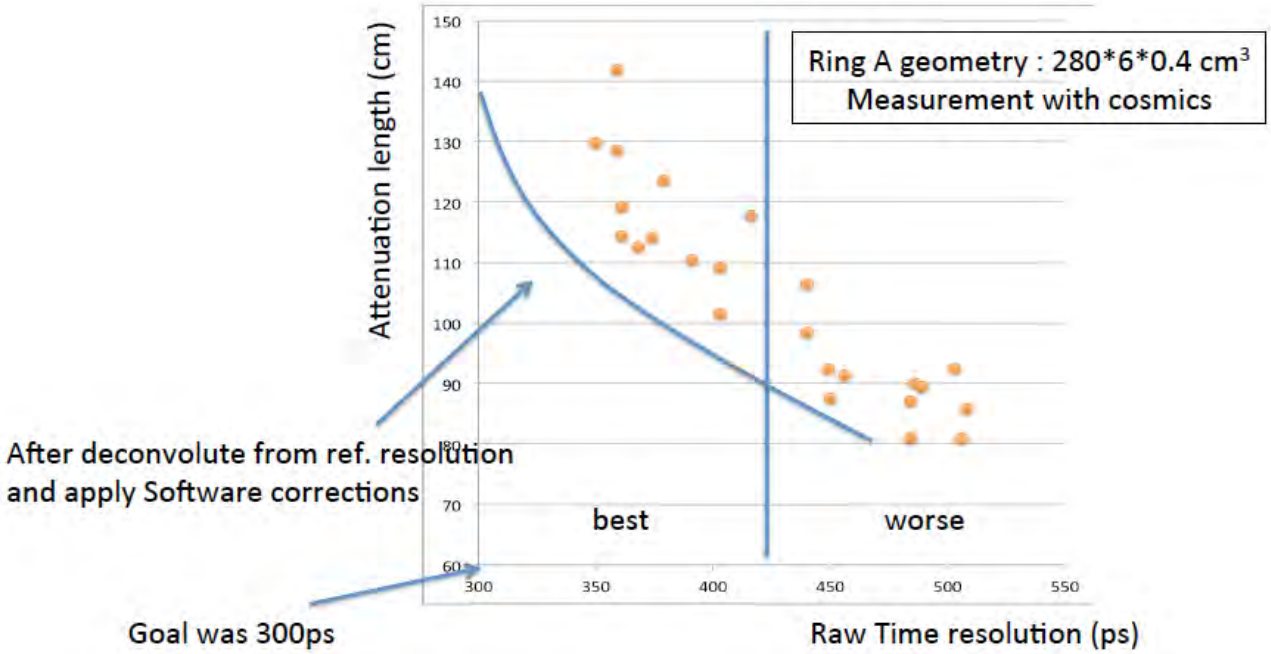

Fig. 57: Measured correlation between the attenuation lengths and time resolutions for the present scintillating counters.

hit detection efficiency, which drops to about 70% at the extremities of the scintillating counter.

During this year, and in preparation of the data taking in 2016, we plan to replace all inner scintillating counters with new ones from a different producer. The new counters will be provided by the Eljen company. Two full-size prototypes have been purchased and tested at the beginning of this year, and found to meet our quality requirements in terms of light attenuation length and time resolution. Figure 58 shows the attenuation length measured with cosmic muons for both prototypes, as well as the time resolution as function of the hit position along the counter. One prototype element shows a very good light transmission ($\lambda \simeq 1.8$ m), while the second one has slightly worse performances ($\lambda \simeq 1.6$ m). The time resolution is measured to be better than 300 ps for both scintillating counters, and reaches as expected an optimum close to the centre of the element. The improved light transmission allows not only to reach the design time resolution, but also to increase by a factor of 3 the number of detected photoelectrons at the extremities of the scintillating counters, thus allowing for a optimal detection efficiency over the full detector length.

In order to insure the same level of quality for the 24 new elements that will replace the existing ones, a detailed quality assessment protocol has been defined and agreed upon with Eljen. Moreover, a total of 28 counters have been ordered to guarantee a 20% safety margin. Each produced counter will be characterised by Eljen prior to the delivery, such that all 28 elements will have a guaranteed λ larger than 1.6 m. Upon reception, all scintillating counters will be re-measured by our group to verify that they meet all specifications, and bad elements will be eventually sent back to the company for replacement. The delivery is expected at the beginning of July 2015, and re-installation in the CAMERA detector is planned during September 2015.

A first calibration of CAMERA installed at the end of the COMPASS hall is under discussion. This will be done using an independent DAQ to provide no interference with the regular Drell-Yan data taking.

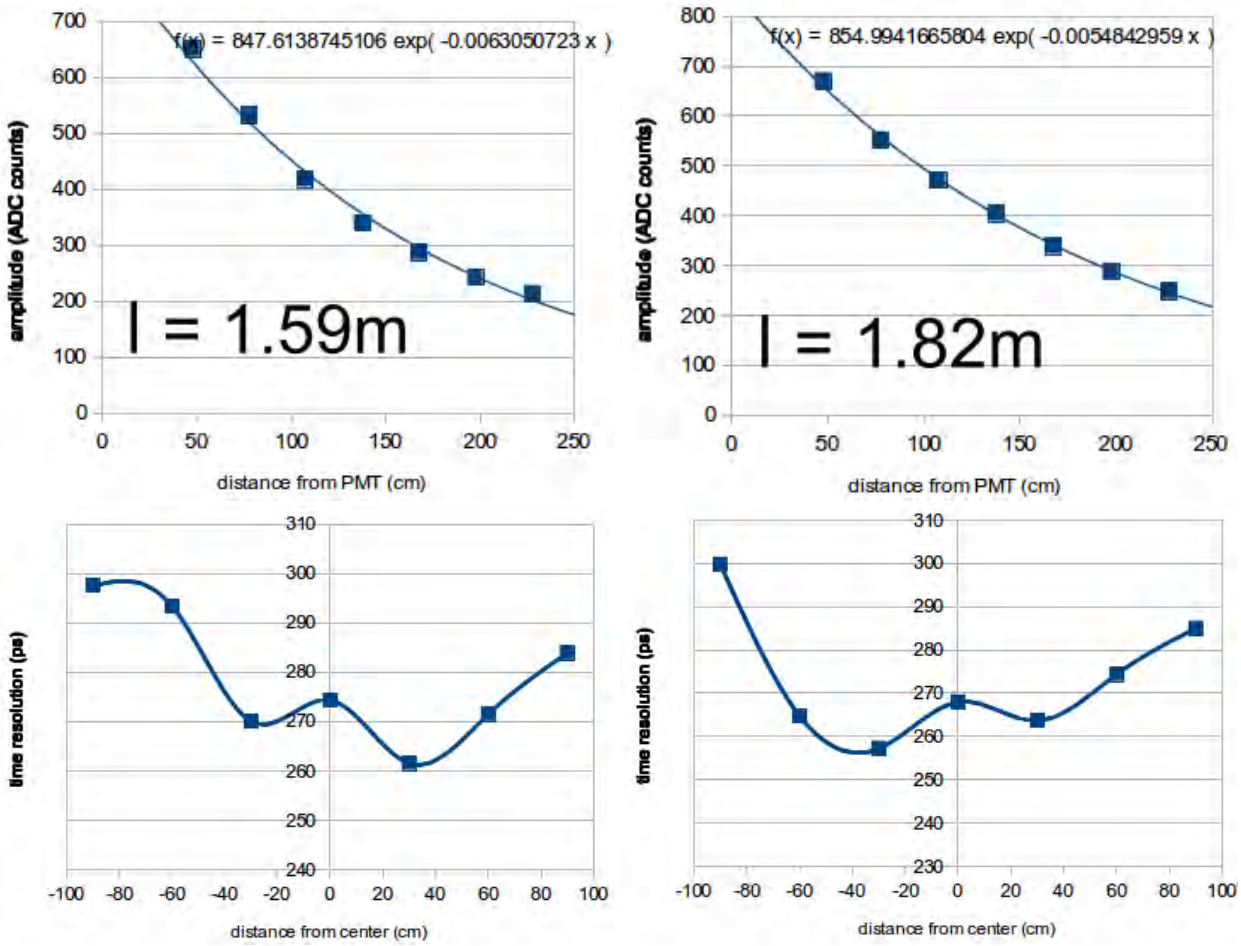

Fig. 58: Measured attenuation length and time resolution for the two Eljen prototypes.

7.2.2 Construction of a start counter based on scintillating fibres

The ToF resolution of the CAMERA detector is mostly limited by the small light yield and the complex light guides geometry of the scintillating counters in the inner barrel. Therefore, the plan is to develop a start counter detector that measures the time of the incoming beam particles with an excellent resolution, and which is mounted just upstream of the target. In combination with the known position of the primary vertex (using information from both the spectrometer and the scintillating counter barrels of CAMERA) and the time information from the outer CAMERA counters, the time-of-flight of the recoil protons can thus be measured with high accuracy.

The basic concept consists of scintillating fibres, stacked to achieve a higher light yield. The individual stacks are arranged in a way, that there is an overlap between adjacent channels in order to guarantee for high efficiency. Moreover, the size of the fibres has to be chosen to achieve a granularity in order to stand the high beam flux. It is planned to set up two of these detectors, where the second is rotated by 90° in order to double the time information and also to gain position information.
During the DVCS test run in 2012 first prototypes were tested. For these prototypes an existing sample of round fibres (Kuraray SCSF 81) with 2.5 mm diameter was used. The layout was chosen similarly to the one of the existing scintillating fibre station FI15. Two prototypes were equipped with one fibre per readout channel, the third prototype with 3 fibres per channel. The latter however could not be fully analysed due to readout problems. Each detector consisted of two sub-planes readout at opposite sides of the detector. This *pseudo double-sided* readout was chosen to compensate time differences depending on the vertex position. Moreover, the readout consisted of standard multianode PMTs (Hamamatsu H6568) and the 16-channel discriminator boards both already used for the existing scintillating fibre detectors.
The extracted time resolution for a single prototype detector was about 330 ps(σ), thus resulting in a resolution

of a detector pair in the order of 230 ps(σ). This already would be a significant improvement compared to the sole use of the inner RPD ring.
Figure 59 (R. Schäfer, Diploma thesis, University of Freiburg) shows the impact that these prototype modules could have on the momentum resolution. At low proton momentum no impact is visible. However with increasing momentum the impact increases, so that for momenta of about 0.7 GeV/c an improvement in the resolution of about 2% (absolute), i.e. 25% relative, can be achieved.
However, there is still ample room for improvement based on the analysis of the prototype data.

1. It turned out, that the use of round fibres is not ideally suited for a high precision time measurement. Due to the reduced path in active scintillating material when getting closer to the fibres edges, the light yield and therefore the output signal decreases. With the leading edge discriminators in use, this leads to a time jitter depending on the position of passage. In the analysis, this effect was partially compensated by defining pseudo-channels for these regions of the fibres, which are the overlap regions of neighbouring fibres exhibiting the time information twice. However, to avoid this effect, the use of square fibres was chosen for the final design.

2. The *pseudo double-sided* readout turned out to be not ideally suited, as it created a variety of fibre combinatorics to be taken into account. Therefore, it was decided to go for a real double sided readout of the scintillating fibre in order to have a reliable mean-timed signal from each hit fibre.

3. For the final design 2 mm square fibres (Bicron BCF-12) were chosen. A single channel will comprise of four of these fibres, resulting in ≈8 mm of active material (compared to ≈2.5 mm for the prototype). Moreover these fibres show an increased trapping efficiency of 7.3% (compared to 5.3%).

4. The existing multianode PMTs will be replaced by the new model already used for the Drell-Yan vertex detector (Hamamatsu R11265). This PMT does not show only a much higher *quantum efficiency* of ≈35% (compared to 20%) but it has also an increased pixel size of 5.8 × 5.8 mm^2 (compared to 4 × 4 mm^2) making the use of four 2 × 2 mm^2 fibres without large crosstalk effects possible.

All these effects will result in an increased light yield calculated to be in the order of a factor of 7.
The time resolution depends on the intrinsic resolution of the PMT (in the order of σ_{PMT} ≈135 ps (σ) and on the light yield, i.e. the number of photo-electrons, $\sigma_{PE} \propto \frac{1}{\sqrt{N_{PE}}}$. Therefore, the achieved resolution per plane could be as low as 175 ps. Even with an increased light yield of only a factor of 4 the resolution of a single detector would be in the order of 200 ps, resulting in a resolution of the detector pair of about 140 ps.

The first detector is under construction now and will be tested and commissioned this July during the Drell-Yan beam time. If the detector features are as expected, the second detector will be build in order to be also tested during this years' beam time. Both detectors will then be ready for data taking early 2016.

7.2.3 Preparation of the complete ECAL0 electromagnetic calorimeter

The large electromagnetic calorimeter ECAL0 to enlarge the angular domain of photon detection is under preparation. In 2012 a part of it, consisting of 56 modules equipped with their registration block as in Fig. 60 (25% of total), was placed 1.5 m downstream of the LH_2 target. The ECAL0 modules are equipped with modern photon detectors multichannel avalanche photon detectors (MAPD), HV, temperature stabilisation and LED-based monitoring systems. ECAL0 demonstrated in the 2012 DVCS pilot run very stable work and successful calibration using pion beam. So the final ECAL0 will be made operational with the same techniques.

The modules are already at CERN and the production of the registration blocks will be finished at Dubna at the end of 2015. The production is performed with new multipixel photon counter (MPP) (S12572-010P MPPC 3x3 mm SMD Package) from Hamamatsu. The delivery of the new registration blocks to CERN will start now and several newly equipped modules will be tested in a dedicated test beam at the end of June 2015. The FEE and cable production and delivery to CERN will be performed before the end of the year. All the equipped modules will be assembled and tested with cosmic muons outside of the beam line and only after that will to be

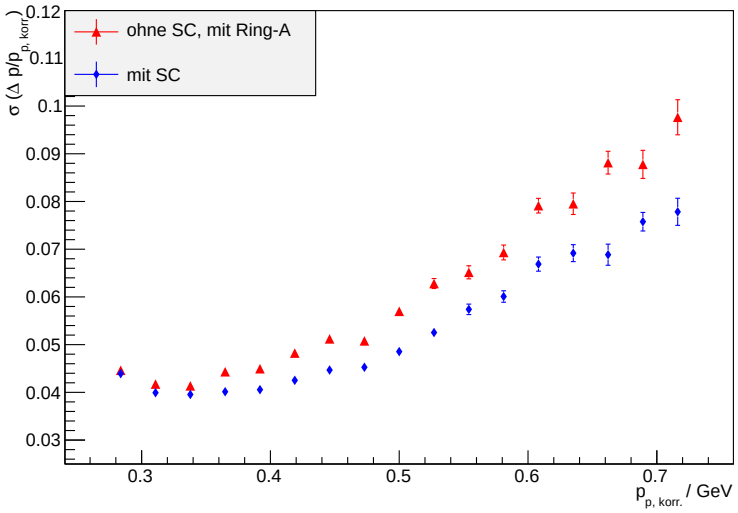

Fig. 59: Relative momentum resolution of the Recoil Proton Detector without (red triangles) and with (blue diamonds) using a start counter. (From: R. Schäfer, Diploma thesis, Univ. Freiburg)

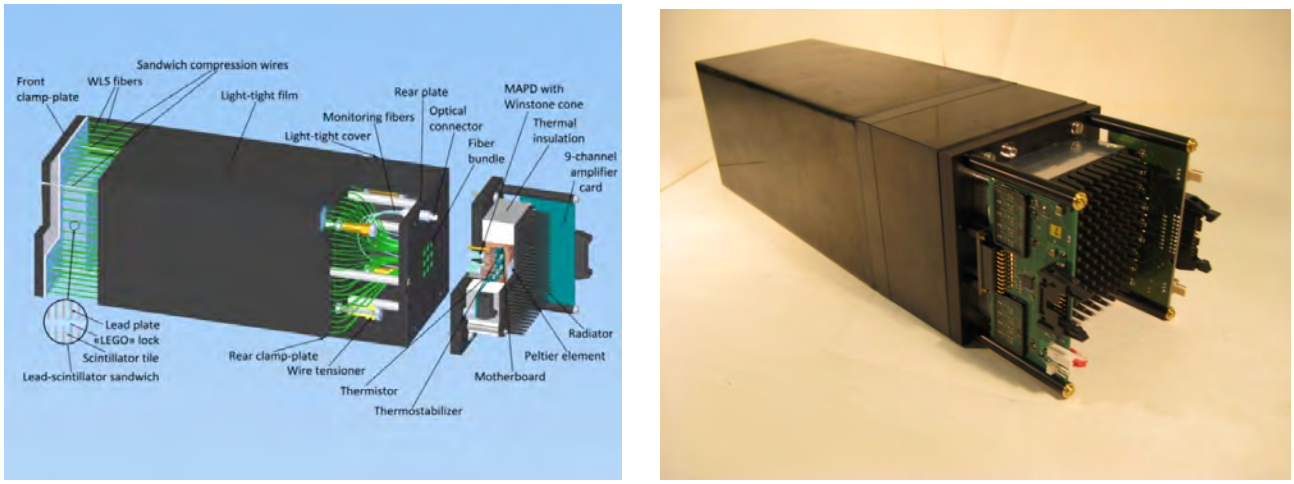

Fig. 60: ECAL0 module sketched (top) and assembled (bottom)

craned in. The working drawings of the metallic frame will be ready in September/October 2015 and the frame will be completed in February 2016. The assembling of the equipped modules in the frame will then start.

7.2.4 Upgrade of the RICH detector

RICH-1 is an essential ingredient of the COMPASS spectrometer and its performance is guaranteed by continuous maintenance and by an ongoing second upgrade of the photon detection system, following the major upgrade during 2005–06.

Concerning maintenance, apart the ordinary operation, in recent years extraordinary maintenance has upgraded the controls of the gas circulation system which ensure the stable pressure and continuous purification of the radiator gas and the cooling system of the read-out electronics based on subathmospheric pressure circulation of cold water.

The photon detection system upgrade consists in the replacement of the gas detectors by CsI photon converters that equip the peripheral regions of the read-out system. The central region equipped with MAPMTs coupled to individual telescopes by fused silica lenses will remain unchanged. The novel photon detectors are based on MPGD (Micro-Pattern Gas detector) technology. The hybrid architecture illustrated in Fig. 61 comprises a double layer of THGEM (THick GEM) multipliers and a MICROMEGAS multiplication stage. The first

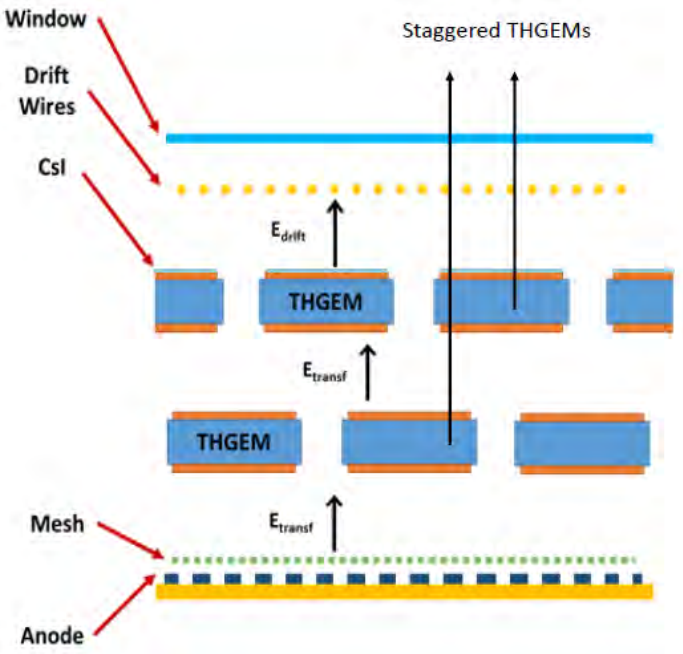

Fig. 61: Scheme of the hybrid architecture novel photon detector (not to scale).

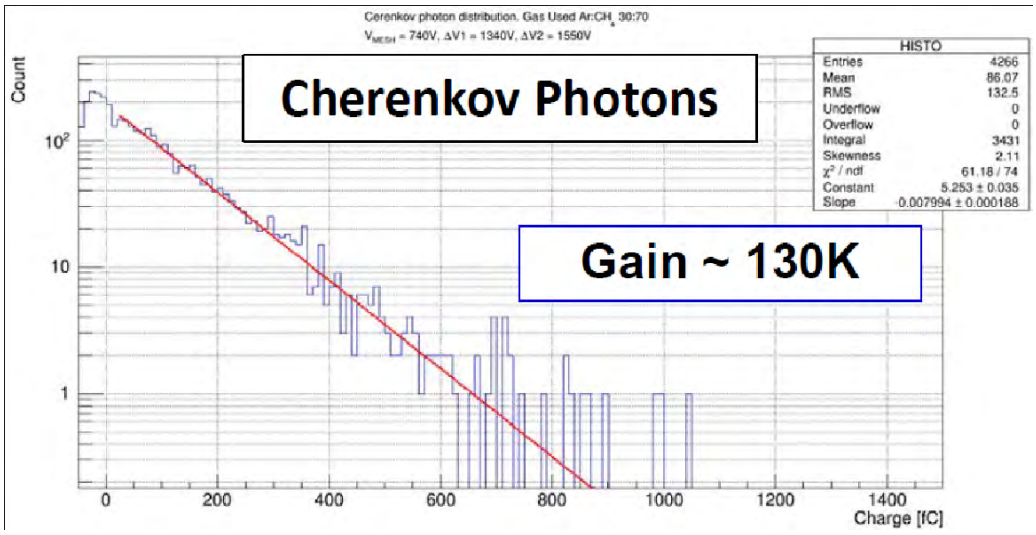

Fig. 62: Single photon amplitude spectrum collected with the hybrid MPGD-based photon detector at a test beam in September 2014.

THGEM board also acts as photocathode: a CsI film is deposited on its surface. These detectors allow to operate at an effective gain of at least 5×10^4 (Fig. 62), namely about five time higher than the effective gain of the present photon detectors, while the detection dead-area is about 10–15% smaller than in the previous detectors. The resulting number of detected photons is expected to increase by 10–20%. The increased gain makes it possible to apply higher electronic thresholds, resulting in a much more effective rejection of the electronic noise and, as a consequence, a cleaner imaging and easier pattern recognition.

The novel photon detectors will make use of the APV25-based read-out electronics already in operation for the MWPC photon converter. Four MWPCs will be replaced during the 2015–2016 shutdown and will be in operation in 2016.

8 Publications and Presentation to Conferences

Publications

1. Measurement of azimuthal hadron asymmetries in semi-inclusive deep inelastic scattering off unpolarised nucleons,
NPB **886** (2014) 1046, CERN-PH-EP/2014-009.

2. A high statistics measurement of transverse spin effects in dihadron production from muon-proton semi-inclusive deep-inelastic scattering,
PLB **736** (2014) 124, CERN-PH-EP/2014-013.

3. Measurement of radiative widths of $a_2(1320)$ and $\pi_2(1670)$, Eur. Phys. J. A **50** (2014) 79,
CERN-PH-EP/2014-041.

4. Spin alignment and violation of the OZI rule in exclusive ω and ϕ production in pp collisions,
NPB **886** (2014) 1078, CERN-PH-EP/2014-096.

5. Measurement of the charged-pion polarisability,
PRL **114** (2015) 062002, CERN-PH-EP/2014-109.

6. Search for exclusive photoproduction of $Z_c(3900)$ production at COMPASS
PLB **742** (2015) 330, CERN-PH-EP/2014-180.

7. Odd and Even Partial Waves of $\eta\pi^-$ and $\eta'\pi^-$ in $\pi \to \eta^{(\prime)}\pi^-$ at 191 GeV/c,
PLB **740** (2015) 303, CERN-PH-EP/2014-204.

8. Collins and Sivers asymmetries in muonproduction of pions and kaons off transversely polarised proton,
PLB **744** (2015) 250, CERN-PH-EP/2014-213

9. The COMPASS setup for physics with hadron beams,
NIMA **779** (2015) 69, CERN-PH-EP/2014-247.

10. Observation of a new narrow axial-vector meson $a_1(1420)$,
submitted to RPL, CERN-PH-EP/2015-015.

11. The spin structure function g_1^p of the proton and a test of the Bjorken sum rule,
submitted to PLB, CERN-PH-EP/2015-085.

Presentation to Conferences:

- 88 presentations to Conferences and Workshops in 2014;

- 27 presentations to Conferences or Workshops in 2015, till June 20.

References

[1] C. Adolph et al. [COMPASS], Measurement of the charged-pion polarizability, *Phys. Rev. Lett.* **114** (2015) 062002. [doi:10.1103/PhysRevLett.114.062002].

[2] B. Pasquini, D. Drechsel, and S. Scherer, The Polarizability of the pion: No conflict between dispersion theory and chiral perturbation theory, *Phys. Rev.* **C77** (2008) 065211. [doi:10.1103/PhysRevC.77.065211].

[3] B. Pasquini, D. Drechsel, and S. Scherer, Reply to 'Comment on 'The Polarizability of the pion: No conflict between dispersion theory and chiral perturbation theory', *Phys. Rev.* **C81** (2010) 029802. [doi:10.1103/PhysRevC.81.029802].

[4] C. Adolph et al. [COMPASS], First Measurement of Chiral Dynamics in $\pi^-\gamma \to \pi^-\pi^-\pi^+$, *Phys.Rev.Lett.* **108** (2012) 192001. [doi:10.1103/PhysRevLett.108.192001].

[5] J. Vijande, A. Valcarce, F. Fernandez, and B. Silvestre-Brac, Nature of the light scalar mesons, *Phys. Rev.* **D72** (2005) 034025. [doi:10.1103/PhysRevD.72.034025].

[6] R. S. Longacre, The $e(1420)$ Meson as a $K\bar{K}\pi$ Molecule, *Phys. Rev.* **D42** (1990) 874–883. [doi:10.1103/PhysRevD.42.874].

[7] S. Paul [COMPASS], Precision spectroscopy with COMPASS and the observation of a new iso-vector resonance, *EPJ Web Conf.* **73** (2014) 03002. [doi:10.1051/epjconf/20147303002]. Presented at MENU2013, Rome.

[8] Z.-G. Wang, Light axial-vector tetraquark state candidate: $a_1(1420)$, arXiv:1401.1134 (2014).

[9] J.-L. Basdevant and E. L. Berger, The twofold emergence of the a_1 axial vector meson in high energy hadronic production, arXiv:1501.04643 (2015).

[10] M. Mikhasenko, B. Ketzer, and A. Sarantsev, Nature of the $a_1(1420)$, *Phys. Rev.* **D91** (2015) 094015. [doi:10.1103/PhysRevD.91.094015].

[11] C. Adolph et al. [COMPASS], Observation of a new narrow axial-vector meson $a_1(1420)$, arXiv:1501.05732 (2015).

[12] C. Adolph et al. [COMPASS], Odd and even partial waves of $\eta\pi$ and $\eta'\pi$ in $\pi p \to \eta^{(\prime)}\pi p$ at 191 GeV/c, *Phys. Lett.* **B740** (2015) 303–311. [doi:10.1016/j.physletb.2014.11.058].

[13] J. Beringer et al. [Particle Data Group], Review of Particle Physics (RPP), *Phys. Rev.* **D86** (2012) 010001. [doi:10.1103/PhysRevD.86.010001].

[14] The COMPASS Collaboration, Compass status report, *CERN-SPSC-2014-020, CERN-SR-139* (2014). URL `http://cds.cern.ch/record/1707909`.

[15] C. Adolph et al. [COMPASS], Spin alignment and violation of the OZI rule in exclusive ω and ϕ production in pp collisions, *Nucl. Phys.* **B886** (2014) 1078–1101. [doi:10.1016/j.nuclphysb.2014.07.020].

[16] C. Adolph et al. [COMPASS], Search for exclusive photoproduction of $Z_c^{\pm}(3900)$ at COMPASS, *Phys. Lett.* **B742** (2015) 330–334. [doi:10.1016/j.physletb.2015.01.042].

[17] C. Adolph et al. [COMPASS], The Spin Structure Function g_1^{p} of the Proton and a Test of the Bjorken Sum Rule, *CERN-PH-EP/2015-085* (2015).

[18] A. D. Martin, W. J. Stirling, R. S. Thorne, and G. Watt, Parton distributions for the LHC, *Eur. Phys. J.* **C63** (2009) 189–285. [doi:10.1140/epjc/s10052-009-1072-5].

[19] C. Adolph et al. [COMPASS], Leading order determination of the gluon polarisation from DIS events with high-p_T hadron pairs, *Phys. Lett.* **B718** (2013) 922–930. [doi:10.1016/j.physletb.2012.11.056].

[20] B. Jäger, M. Stratmann, and W. Vogelsang, Longitudinally polarized photoproduction of inclusive hadrons at fixed-target experiments, *Eur. Phys. J.* **C44** (2005) 533–543. [doi:10.1140/epjc/s2005-02380-0].

[21] D. de Florian, M. Pfeuffer, A. Schäfer, and W. Vogelsang, Soft-gluon Resummation for High-pT Inclusive-Hadron Production at COMPASS, *Phys. Rev.* **D88** (2013) 014024. [doi:10.1103/PhysRevD.88.014024].

[22] C. Adolph et al. [COMPASS], Measurement of the cross section for high-pT hadron production in the scattering of 160-GeV/c muons off nucleons, *Phys. Rev.* **D88** (2013) 091101. [doi:10.1103/PhysRevD.88.091101].

[23] M. Glück, E. Reya, M. Stratmann, and W. Vogelsang, Models for the polarized parton distributions of the nucleon, *Phys. Rev.* **D63** (2001) 094005. [doi:10.1103/PhysRevD.63.094005].

[24] D. de Florian, R. Sassot, M. Stratmann, and W. Vogelsang, Evidence for polarization of gluons in the proton, *Phys. Rev. Lett.* **113** (2014) 012001. [doi:10.1103/PhysRevLett.113.012001].

[25] D. de Florian, R. Sassot, and M. Stratmann, Global analysis of fragmentation functions for pions and kaons and their uncertainties, *Phys. Rev.* **D75** (2007) 114010. [doi:10.1103/PhysRevD.75.114010].

[26] J. Pumplin, D. Stump, J. Huston, H. Lai, P. M. Nadolsky, et al., New generation of parton distributions with uncertainties from global QCD analysis, *JHEP* **0207** (2002) 012. [doi:10.1088/1126-6708/2002/07/012].

[27] M. Glück, E. Reya, and I. Schienbein, Radiatively generated parton distributions of real and virtual photons, *Phys. Rev.* **D60** (1999) 054019. [doi:10.1103/PhysRevD.60.054019, 10.1103/PhysRevD.62.019902].

[28] W. Vogelsang, Radiatively generated parton distributions of polarized hadrons and photons, arXiv:hep-ph/9510429 (1995).

[29] A. Bacchetta et al., Semi-inclusive deep inelastic scattering at small transverse momentum, *JHEP* **02** (2007) 093.

[30] C. Adolph et al. [COMPASS], A high-statistics measurement of transverse spin effects in dihadron production from muon-proton semi-inclusive deep-inelastic scattering, *Phys. Lett.* **B736** (2014) 124–131. [doi:10.1016/j.physletb.2014.06.080].

[31] A. Kotzinian, Azimuthal Correlations in the Structure Functions of polarized Dihadron Semi-Inclusive Deep Inelastic Scattering, *Phys. Rev.* **D91** (2015) 054001. [doi:10.1103/PhysRevD.91.054001].

[32] F. Bradamante [COMPASS], Work on the interplay among h^+, h^- and hadron pair transverse spin asymmetries in SIDIS, arXiv:1502.01451 (2015). Presented at SPIN 2014, Beijing.

[33] S. Goloskokov and P. Kroll, Transversity in exclusive vector-meson leptoproduction, *Eur. Phys. J.* **C74** (2014) 2725. [doi:10.1140/epjc/s10052-014-2725-6].

[34] C. Adolph et al. [COMPASS], Exclusive ρ^0 muoproduction on transversely polarised protons and deuterons, *Nucl. Phys.* **B865** (2012) 1–20. [doi:10.1016/j.nuclphysb.2012.07.025].

[35] C. Adolph et al. [COMPASS], Transverse target spin asymmetries in exclusive ρ^0 muoproduction, *Phys. Lett.* **B731** (2014) 19–26. [doi:10.1016/j.physletb.2014.02.005].

[36] A. Airapetian et al. [HERMES], Multiplicities of charged pions and kaons from semi-inclusive deep-inelastic scattering by the proton and the deuteron, *Phys. Rev.* **D87** (2013) 074029. [doi:10.1103/PhysRevD.87.074029].

[37] A. Airapetian et al. [HERMES], Reevaluation of the parton distribution of strange quarks in the nucleon, *Phys. Rev.* **D89** (2014) 097101. [doi:10.1103/PhysRevD.89.097101].

[38] M. Anselmino, M. Boglione, J. Gonzalez Hernandez, S. Melis, and A. Prokudin, Unpolarised Transverse Momentum Dependent Distribution and Fragmentation Functions from SIDIS Multiplicities, *JHEP* **1404** (2014) 005. [doi:10.1007/JHEP04(2014)005].

[39] C. Adolph et al. [COMPASS], Hadron Transverse Momentum Distributions in Muon Deep Inelastic Scattering at 160 GeV/*c*, *Eur. Phys. J.* **C73** (2013) 2531. [doi:10.1140/epjc/s10052-013-2531-6]. Erratum ibid. **C75** (2015) 94, [doi:10.1140/epjc/s10052-014-3255-y].

[40] G. Baum et al. [COMPASS], COMPASS-II proposal, *CERN/SPSC-2010-014, SPSC-P-340* (2010). URL `http://cdsweb.cern.ch/record/1265628/files/SPSC-P-340.pdf`.

[41] C. Adolph et al. [COMPASS], Collins and Sivers asymmetries in muonproduction of pions and kaons off transversely polarised protons, *Phys. Lett.* **B744** (2015) 250–259. [doi:10.1016/j.physletb.2015.03.056].